REVIVING ABANDONED RESERVOIRS WITH HIGH-PRESSURE AIR INJECTION:
APPLICATION IN A FRACTURED AND KARSTED DOLOMITE RESERVOIR

Final Report

Principal Authors: Robert Loucks[1] (Co-PI), Stephen C. Ruppel[1] (Co-PI),

Contributors: Dembla Dhiraj[2], Julia Gale[1], Jon Holder[2], Jeff Kane[1], and Jon Olson[2]

[1]Bureau of Economic Geology
John A. and Katherine G. Jackson School of Geosciences
The University of Texas at Austin
Austin, TX 78713

[2]Department of Petroleum Engineering
The University of Texas at Austin
Austin, TX 78713

Date Report Issued: March 2007

Contents

Figures

iv

Tables

Disclaimer

EXECUTIVE SUMMARY

Despite declining production rates, existing reservoirs in the United States contain vast volumes of remaining oil that is not being effectively recovered. This oil resource constitutes a huge target for the development and application of modern, cost-effective technologies for producing oil. Chief among the barriers to the recovery of this oil are the high costs of designing and implementing conventional advanced recovery technologies in these mature, in many cases pressure-depleted, reservoirs. An additional, increasingly significant barrier is the lack of vital technical expertise necessary for the application of these technologies. This lack of expertise is especially notable among the small operators and independents that operate many of these mature, yet oil-rich, reservoirs. We addressed these barriers to more effective oil recovery by developing, testing, applying, and documenting an innovative technology that can be used by even the smallest operator to significantly increase the flow of oil from mature U.S. reservoirs.

The Bureau of Economic Geology and Goldrus Producing Company assembled a multidisciplinary team of geoscientists and engineers to evaluate the applicability of high-pressure air injection (HPAI) in revitalizing a nearly abandoned carbonate reservoir in the Permian Basin of West Texas. The Permian Basin, the largest oil-bearing basin in North America, contains more than 70 billion barrels of remaining oil in place and is an ideal venue to validate this technology. We have demonstrated the potential of HPAI for oil-recovery improvement in preliminary laboratory tests and a reservoir pilot project. To more completely test the technology, this project emphasized detailed characterization of reservoir properties, which were integrated to access the effectiveness and economics of HPAI.

The characterization phase of the project utilized geoscientists and petroleum engineers from the Bureau of Economic Geology and the Department of Petroleum Engineering (both at The University of Texas at Austin) to define the controls on fluid flow in the reservoir as a basis for developing a reservoir model.

The successful development of HPAI technology has tremendous potential for increasing the flow of oil from deep carbonate reservoirs in the Permian Basin, a target resource that can be conservatively estimated at more than 1.5 billion barrels. Successful

1

implementation in the field chosen for demonstration, for example, could result in the recovery of more than 34 million barrels of oil that will not otherwise be produced.

Geological and petrophysical analysis of available data at Barnhart field reveals the following important observations: (1) the Barnhart Ellenburger reservoir is similar to most other Ellenburger reservoirs in terms of depositional facies, diagenesis, and petrophysical attributes; (2) the reservoir is characterized by low to moderate matrix porosity much like most other Ellenburger reservoirs in the Permian Basin; (3) karst processes (cave formation, infill, and collapse) have substantially altered stratigraphic architecture and reservoir properties; (4) porosity and permeability increase with depth and may be associated with the degree of karst-related diagenesis; (5) tectonic fractures overprint the reservoir, improving overall connectivity; (6) oil-saturation profiles show that the oil-water contact (OWC) is as much as 125 ft lower than previous estimations; (7) production history and trends suggest that this reservoir is very similar to other solution-gas-drive reservoirs in the Permian Basin; and (8) reservoir simulation study showed that the Barnhart reservoir is a good candidate for HPAI and that application of horizontal-well technology can improve ultimate resource recovery from the reservoir.

INTRODUCTION

This report details the geology, petrophysics, and some engineering attributes of the Barnhart field Ellenburger reservoir in southeastern Reagan County, Texas (Fig. 1). Goldrus Producing Company acquired a major working interest in Barnhart field and has initiated redevelopment of the field by implementing a very recently proven, potentially revolutionary, new technology. This technology employs a combination of high-pressure air injection (HPAI) and vertical and horizontal well completions to increase sweep efficiency. HPAI, a tertiary oil recovery technology, works by creating a downhole combustion of oxygen and oil to produce flue gas (nitrogen and carbon dioxide) that serves, at the same time, to repressurize and flood the reservoir. The HPAI process has been tested with considerable success in reservoirs of the Red River Formation (analogous Ordovician dolostones and limestones) in the Williston Basin of South Dakota, North Dakota, and Montana (Kumar and others, 1995; Fassihi and others, 1996, 1997; Watts and others, 1997; Glandt and others, 1998). In these reservoirs, HPAI has

2

resulted in rapid increases in production rates. For example, in the Medicine Pole Hills reservoir, which is analogous to the Barnhart reservoir in size, mineralogy, and depth, production rates increased by 400 barrels of oil per day (bopd) within 3 years of the beginning of air injection (Fig. 2). Fassihi and others (1997) estimated that HPAI will realize an incremental recovery of more than 14 percent of the original oil in place (OOIP) in this field. Other Red River fields where HPAI has been implemented have responded similarly (Erickson and others, 1992). Barnhart field meets the criteria for successful application of HPAI technology defined by Erickson and others (1992): depth greater than 5,500 ft, API gravity greater than 25, temperature greater than 170° Fahrenheit. (See Kuhlman, 2004, for a more complete discussion of the propriety of the Barnhart reservoir for application of this technology.)
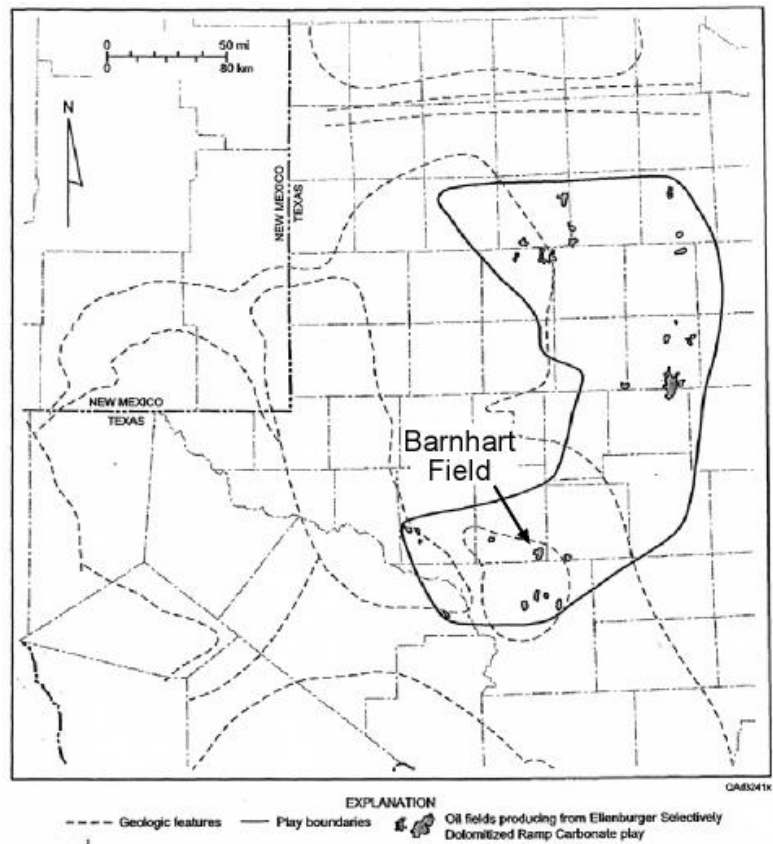
Figure 1. Regional map of the Permian Basin showing major Ellenburger fields and the location of Barnhart field. From Dutton and others (2005).
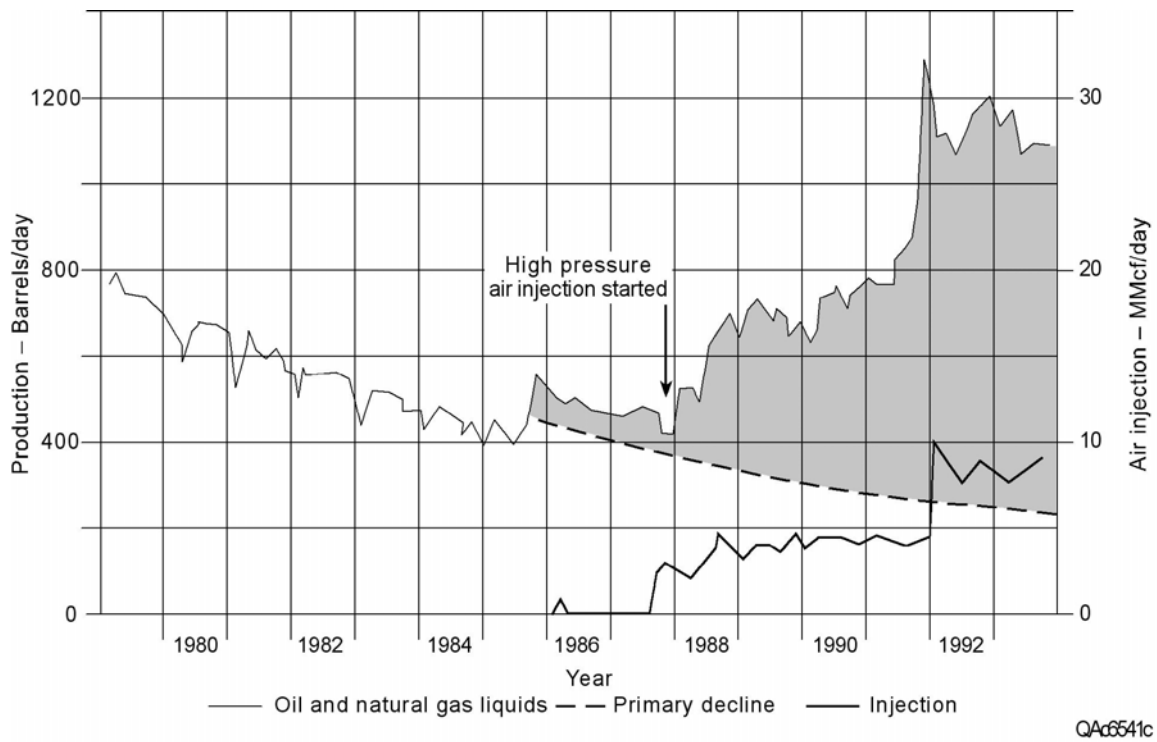
Figure 2. Production response from high-pressure air injection into the Red River reservoir at Medicine Pole Hills field, Williston Basin. Note the rapid increase in production following the onset of air injection in 1987. From Kumar and others (1995).

Critical to the successful application of HPAI, or any other advanced recovery technology, at Barnhart field is improvement in understanding of the reservoir geology in terms of reservoir facies, pore types, reservoir architecture (stratigraphy and continuity), rock-fabric types, and petrophysics. This report summarizes results of a series of integrated studies on Barnhart field. Data collected for these studies of the Barnhart reservoir for the first time provide robust insights into reservoir geology and petrophysics that can be used to guide specific plans of reservoir redevelopment leading to recovery of the large oil volume that still resides in the reservoir.

FIELD SETTING AND HISTORY

Barnhart field is located in southeast Reagan County about 10 mi southeast of the town of Big Lake, Texas (Fig. 1). Most oil production from the field has come from the Ellenburger Group at a depth of approximately 9,000 ft (Fig. 3). The field (Fig. 4) was discovered in 1941, with the first well testing at a rate of 1,122 bopd. Subsequent wells

4

were completed at substantially higher initial production rates. The combined average of reported initial production rates for the first 24 wells drilled in the field, for example, was more than1,300 bopd (J. Lomax, personal communication). By 1950, the field had produced more than 10 million barrels (MMbbl) of oil but was already experiencing substantial declines in production rates and reservoir pressure (Fig. 5). Unlike most Ellenburger reservoirs in the Permian Basin, the Barnhart reservoir is characterized by a solution-gas drive rather than water drive. Field producing rates continued to decline rapidly after 1950, falling to less than 1,000 bopd by 1956. In 1968, a pilot waterflood program was attempted to reverse pressure decline and increase production. However, this program was abandoned (1971) before its impact could be fully evaluated. Most of the wells in the field, which totaled about 80, were subsequently abandoned. By 1974, only a few producing wells remained, and cumulative oil production from the field totaled about 15.5 MMbbl. At present, cumulative production from the entire field stands at about 16 MMbbl of oil. Extrapolation of studies by Tyler and others (1991) indicates that recovery efficiency from the Barnhart reservoir is less than 17 percent of the OOIP. This leaves a remaining total resource of nearly 100 MMbbl as a target for the application of improved recovery methodologies.
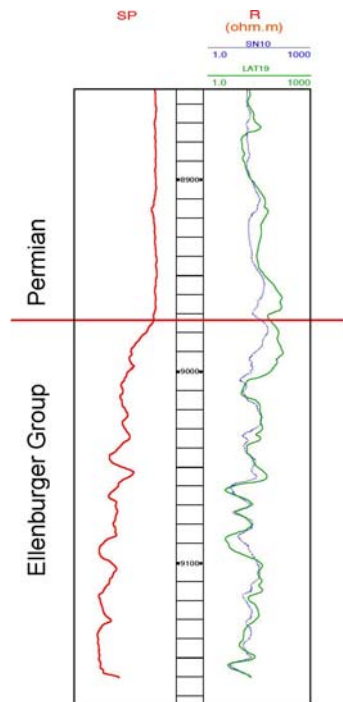
Figure 3. Type log of the Ellenburger reservoir in Barnhart field.
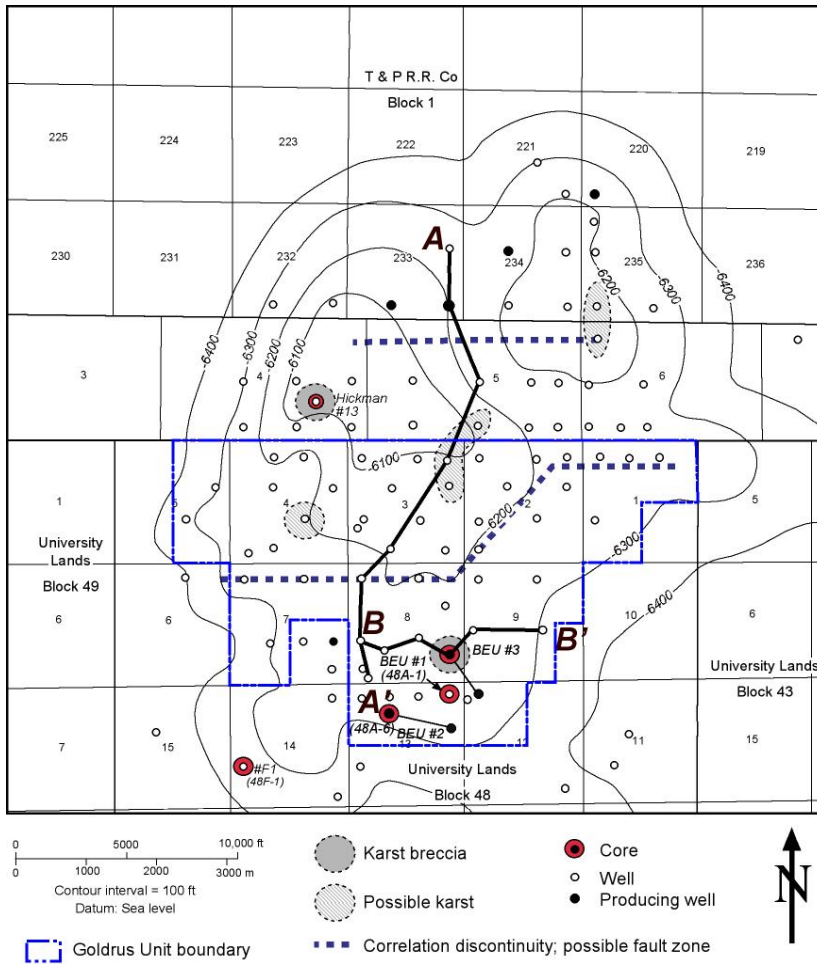
Figure 4. Map of Barnhart field showing structure at the top of the Ellenburger reservoir and distribution of University and State leases. Also shown are areas of probable karst diagenesis. After Cotton (1966).
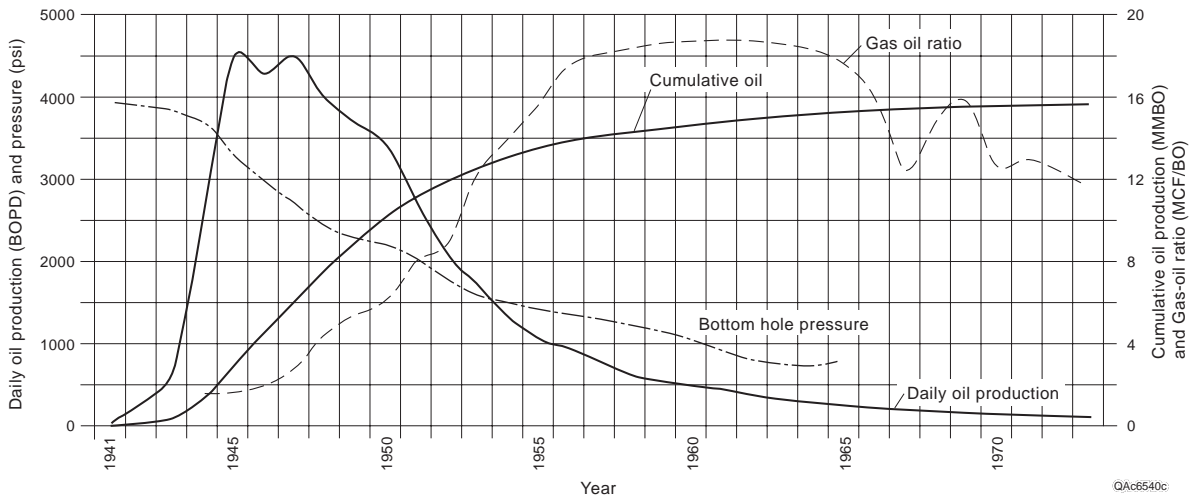
Figure 5. Production history of the Ellenburger reservoir at Barnhart field.

REGIONAL SETTING

The Ellenburger reservoir in the Barnhart area is one of several similar reservoirs developed across the east and southeast part of the Permian Basin that have been assigned to the Ellenburger Selectively Dolomitized Ramp Carbonate subplay (Fig. 1; Dutton and others, 2005). Ellenburger reservoirs in this play have the following attributes in common: (1) they are composed primarily of dolostones and lesser limestones; (2) they contain cyclic, upward-shallowing successions of shallow-water platform facies; (3) they contain common evidence of karst diagenesis and cave formation; (4) they are trapped by simple anticlines, truncated flanks of anticlines, or permeability barriers caused by dolostones along faults and steep flexures; and (5) they are sealed by shales of Permian, Pennsylvanian, or Mississippian age (Britt, 1988; Mazzullo, 1989; Holtz and Kerans, 1992).

Net pay in the play ranges from 4 to 223 ft and averages 43 ft (Holtz and Kerans, 1992). Porosity, mostly intercrystalline and interparticle, ranges from 1 to 20 percent and averages 6.4 percent. Permeability values range from 0.2 to 48 md and are log-normally distributed around a geometric mean value of 12 md.

Galloway and others (1983) showed that the average recovery efficiency from Ellenburger reservoirs of this play varies significantly with drive mechanism. Water-drive Ellenburger reservoirs characteristically exhibit 10 percent higher recovery efficiency on average than do solution-gas-drive reservoirs (45 and 35 percent, respectively). The current low-recovery efficiency at Barnhart is consistent with primary recovery operations in solution-gas-drive reservoirs developed in carbonates. For example, similarly low recoveries are typical for Leonardian shallow-water platform reservoirs on the Central Basin Platform (average 17 percent efficiency), even after secondary recovery operations have been applied (Holtz and others, 1992). As is the case in the Ellenburger reservoir at Barnhart, these reservoirs are developed in dolomitized, low-permeability rocks. The low-permeability and solution-gas (pressure-depletion) - drive characteristics of these reservoirs require secondary and in some cases tertiary technologies to obtain even moderate efficiencies. In many ways, the Barnhart

Ellenburger reservoir more closely resembles these Permian reservoirs than it does other Ellenburger reservoirs with active water drives.

GEOLOGICAL SETTING OF BARNHART FIELD

Barnhart field is a structural trap with four-way closure that encompasses approximately 16 mi^2 (Fig. 4; Umphress, 1977; Hunt, 2000). Throughout much of the field, the Ellenburger reservoir section is overlain by shales of probable Pennsylvanian or Permian age (Fig. 3; Umphress, 1977). These shales provide both a top seal and a possible source of hydrocarbon charge for the underlying Ellenburger. Along the margins of the field, especially to the south, there is evidence that older Paleozoic carbonates (probably Silurian Fusselman Formation) and sandstones (Ordovician Simpson Group) overlie the Ellenburger strata (Umphress, 1977). The younger carbonates are not clearly distinguishable from those of the Ellenburger and may locally be included in the top of the reservoir section.

Burial History

Regional analysis of the burial history of the Ellenburger suggests a complex history of repeated uplift and exposure: at least seven episodes of uplift and erosion are apparent (Combs and others, 2003). The most significant of these probably took place during (1) the Middle Ordovician, (2) the Middle Devonian, and (3) the Early Pennsylvanian. During each of these times, the Ellenburger may have been unroofed and exposed to multiple episodes of karst-related diagenetic processes. Of these, however, the Middle Ordovician and Early Pennsylvanian events probably had the greatest effect on the structure and diagenesis of the reservoir succession. Exposure during the Middle Ordovician resulted in extensive karst-associated cave development. The Early Pennsylvanian, a time of major tectonic uplift and erosion in the Permian Basin, was associated with the development of compressive crustal forces caused by the collision of the beginning of the assembly of Pangaea. Both the basic structure of the field and the widespread fracturing of the Ellenburger succession most likely formed during the Early Pennsylvanian. Renewed karsting of the field area probably also took place at this time.

General Structure and Stratigraphy

The structure and stratigraphy of the Barnhart Ellenburger reservoir are best understood by correlating well-defined, stratigraphic markers of the shale-dominated succession that overlies the reservoir (Fig. 6). These markers, which are areally continuous, document the development of widespread, deeper water siliciclastic deposition associated with the overall flooding and subsidence of the Barnhart area in the Late Pennsylvanian-Early Permian. Correlation of these units reveals that they onlap the Ellenburger, thus documenting the progressive burial of the field structure at this time. Figure 4 displays the structure of the unconformity that separates the Ellenburger section from the overlying siliciclastics. As will be documented later in this report, the internal stratigraphy of the Ellenburger displays complex angular relationships to this unconformity.
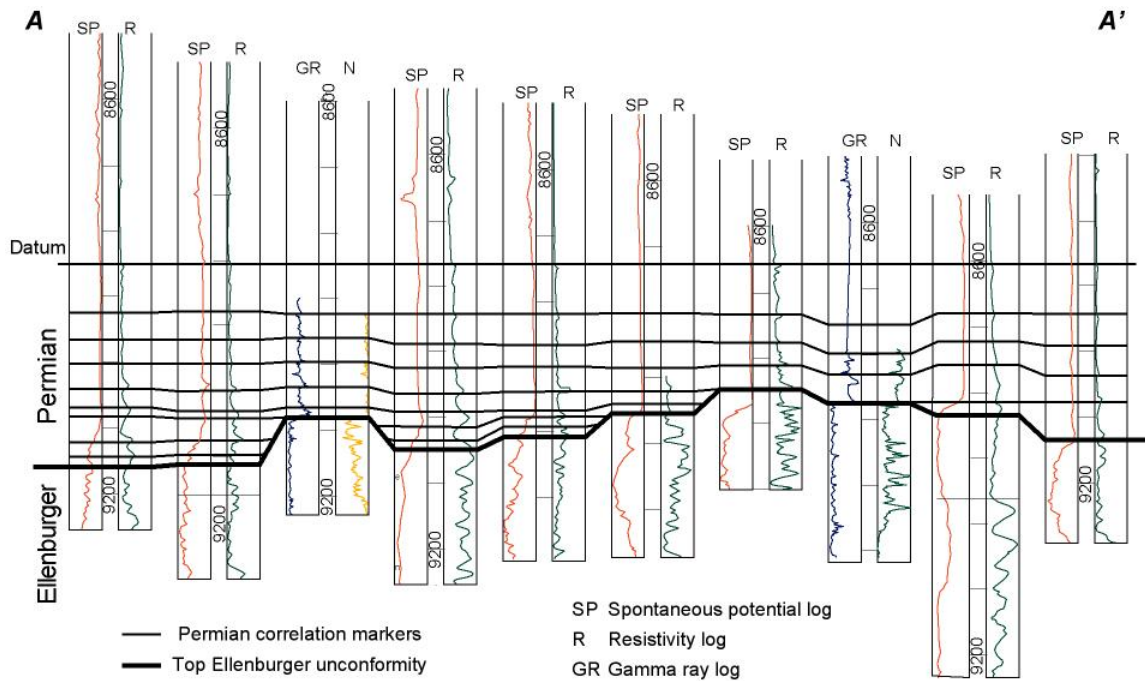
Figure 6. Cross section A-A′ showing correlations of Upper Pennsylvanian-Lower Permian (Wolfcampian) shales that overlie the Ellenburger reservoir at Barnhart field. After Combs and others (2003).

DEPOSITIONAL FACIES AND PALEOENVIRONMENTS

Previous studies of the Ellenburger Group have demonstrated that the succession was deposited on a regionally extensive, peritidal, carbonate-shelf environment, producing broad, laterally continuous deposits showing little stratal thickness variation. Carbonate facies encompass a range of rock types from laminated mudstones produced in inner tidal-flat environments to packstones and grainstones facies deposited in open, shallow, subtidal settings (Kerans, 1990).

Five Barnhart Ellenburger wells are known to have been cored (Belco Hickman #13; Arco 48 F #1; and Goldrus Barnhart Unit wells #1, 2, and 3). Interpretations of facies types present at Barnhart are based on whole cores, sidewall cores, core chips, thin sections, and photographs from these cored wells. These data indicate that the Ellenburger at Barnhart field contains facies that are consistent with regional models. Most of the rocks cored in the wells in the south part of the field are completely dolomitized. Significant amounts of limestone have been encountered only in the Hickman #13 core and nearby wells in the north part of the field. No siliciclastic deposits (e.g., sandstones or shales) have been observed in the Ellenburger reservoir interval other than a few thin shales that formed as local cave-sediment fills.

Facies observed in cores from Barnhart field are dominated by mud-rich peritidal deposits. By far the most abundant facies are featureless mudstones. Locally these deposits are laminated. In some cases laminations are wavy, suggestive of cyanobacterial or cryptalgal origins, but more commonly they are planar and horizontal (Fig. 7). Fenestral pores indicative of subaerial exposure are locally encountered but are generally rare. Skeletal material is similarly rare, but fragments of clams and snails are locally observed. Evidence of burrowing is also uncommon. The absence of fauna, the abundance of carbonate mud, and the evidence, although rare, of episodic exposure (laminations and fenestrate) suggest that these rocks were deposited on a restricted, very shallow-water, inner carbonate platform. Nearly all of the samples examined from the cores in the south part of the field (including the Goldrus Unit) are consistent with the description and interpretation given earlier.
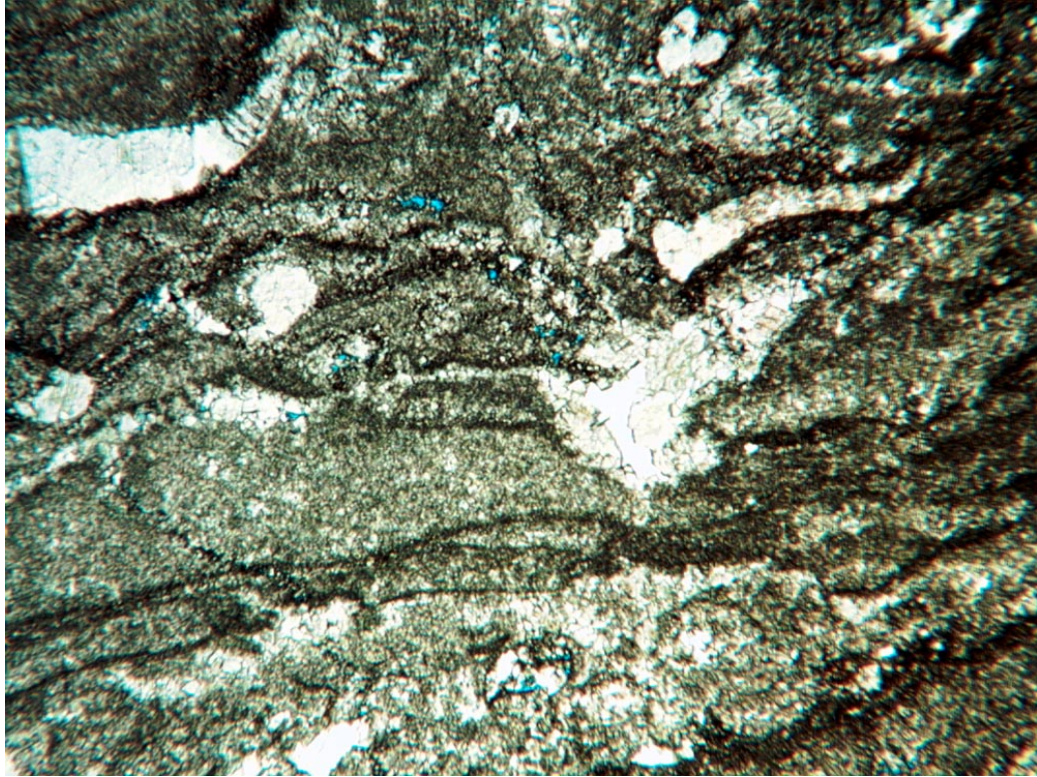
Figure 7. Photomicrograph showing laminated peritidal mudstone. Goldrus BEU #3 well. 9,063.2 ft. Width of photograph is 3.5 mm.

Subtidal facies have been observed in some parts of the field. Umphress (1977) noted several zones of ooid grainstone in the core from the Hickman #13 well and in cuttings from the nearby Hickman #2 well. These deposits are most common in the limestone-dominated upper part of the cored interval, although thin intervals of ooid-bearing facies were also observed in the dolomitized lower section. A single sample of ooid-bearing grainstone was also encountered in the Arco 48F#1 core in the south part of the field (Fig. 8). These ooid-bearing intervals, especially the thicker intervals observed in the Hickman wells, indicate the development of higher energy, subtidal depositional conditions. Tentative fieldwide correlations suggest that this upper limestone-dominated, subtidal section (which Umphress, 1977, referred to as the upper Ellenburger Group Gorman Formation) may be absent over the south part of the field.
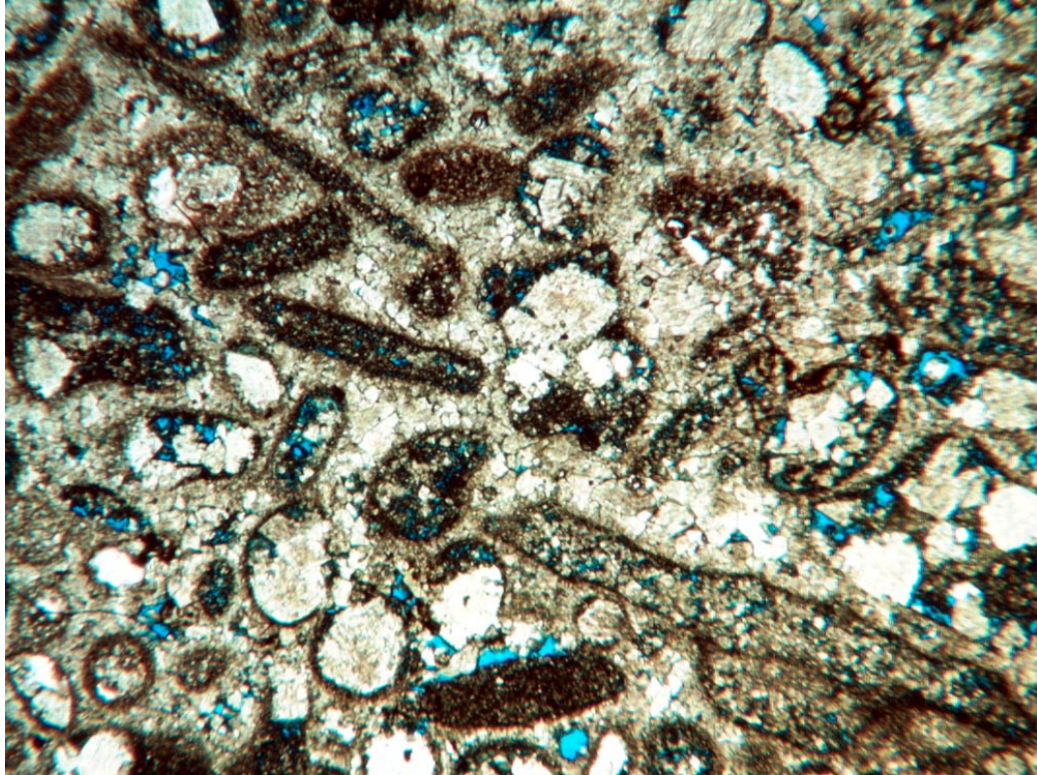
Figure 8. Photomicrograph of coated grain/ooid subtidal grainstone. Note minor interparticle porosity. Arco 48F#1 well. 9,233 ft. Width of photograph is 3.5 mm.

PALEOCAVE FACIES AND ASSOCIATED PORE NETWORKS

Paleocave Facies

<u>General Comments</u>

Core material is available from several wells in Barnhart field (Fig. 9). The complete core of the Goldrus Producing Company Barnhart Ellenburger Unit (BEU) #3 was available for description and detailed analysis, whereas only core chips and photographs were available for the University 48-F-1 and Hickman 13 wells. All three cores were analyzed for evidence of karst, fractures, and breccia types. BEU #3 was analyzed in the most detail, and results are presented in this section of the report.
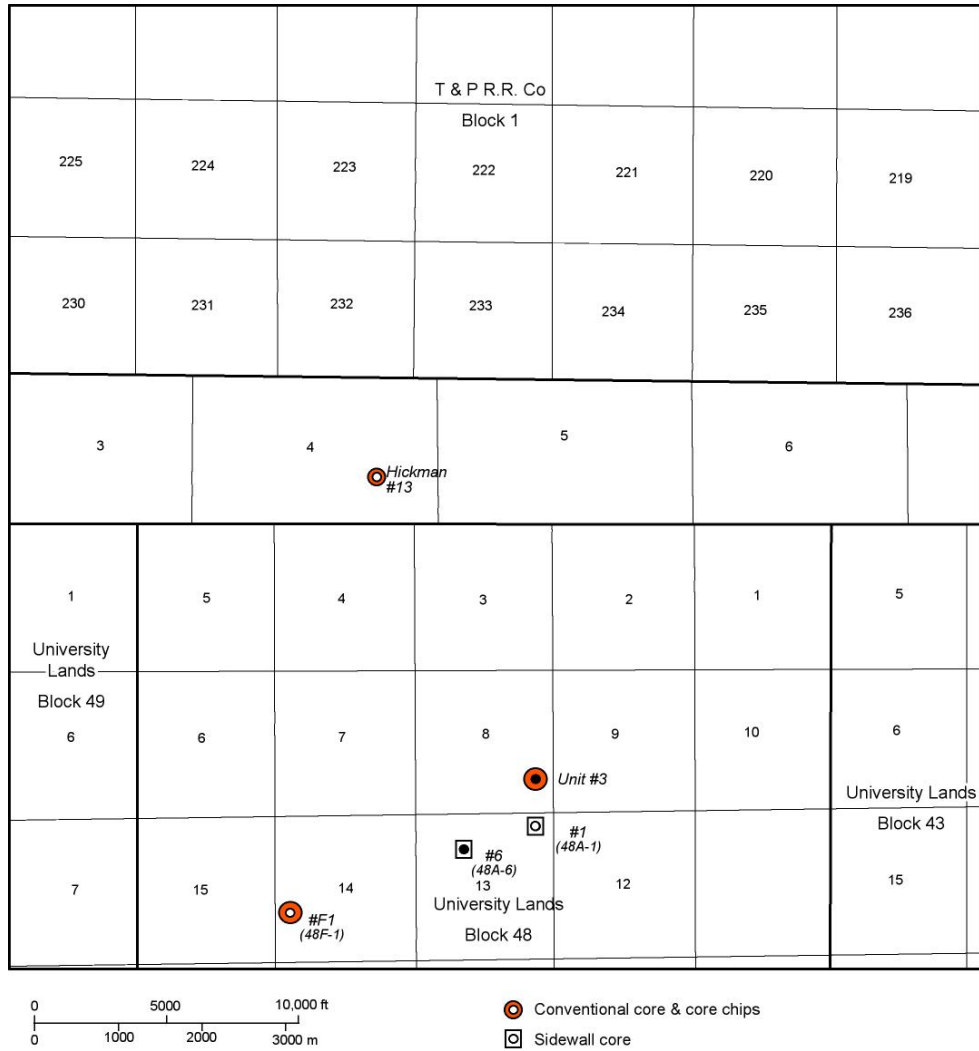
Figure 9. Location of core samples in Barnhart field.
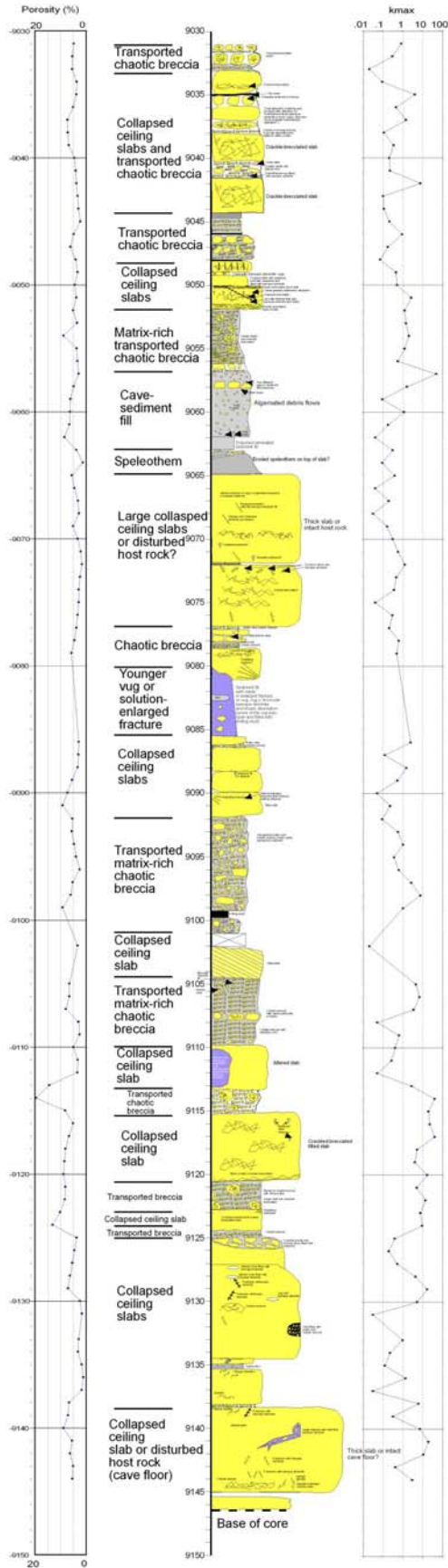
Figure 10. Core description of Goldrus Producing Company Unit #3 core showing textures and fabrics of the collapsed-paleocave system.

14

The BEU #3 well core (Figs. 9 and 10) covers the drilling-depth interval from 9,031 ft to 9,146 ft. All 115 ft of core penetrated collapsed paleocave facies that experienced a period of hydrothermal alteration associated with the Ouachita Orogeny during the Pennsylvanian (Fig. 11) (Kupecz and Land, 1991). The wireline logs in nearby wells are correlative to one another, but not to the BEU #3 wireline logs (see section on Reservoir Architecture and Continuity later in this report). This discrepancy is interpreted to be due to the presence of collapsed paleocave facies in the BEU #3 well and the relative absence of paleocave facies in surrounding wells.
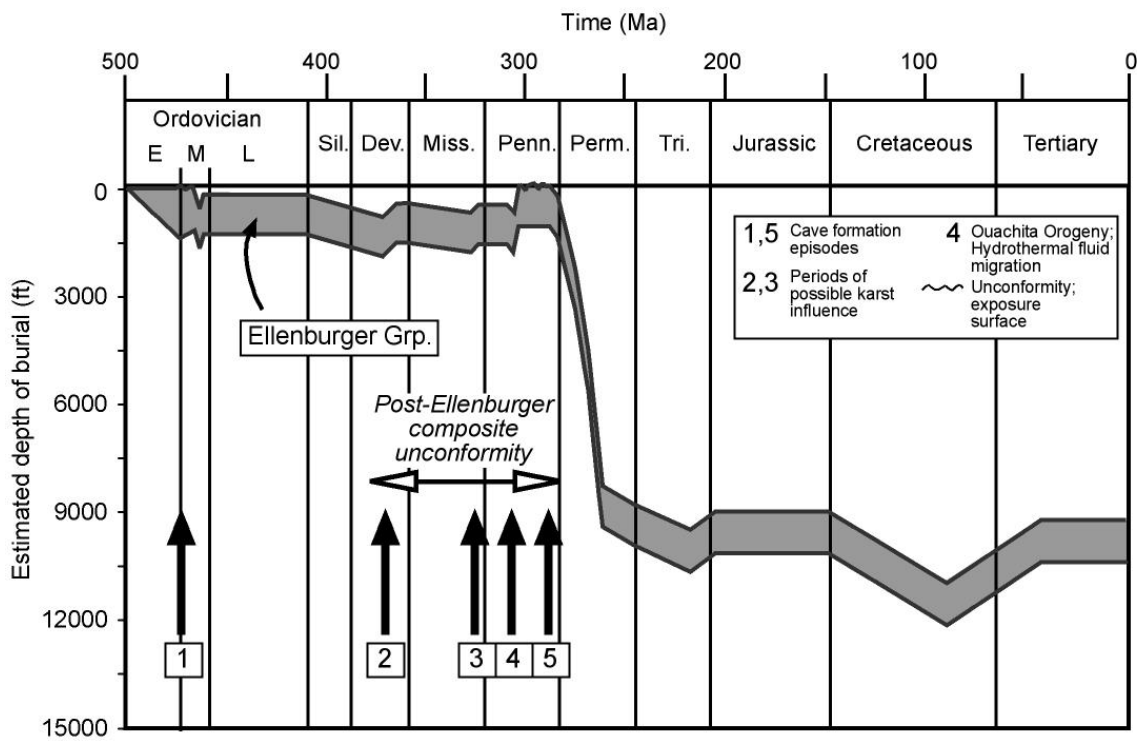
Figure 11. Generalized burial history of the Ellenburger Group at Barnhart field. The Barnhart field area underwent multiple episodes of uplift. At least two of these episodes (Early-Middle Ordovician and Pennsylvanian) exposed the Ellenburger Group to karstification and cave formation. The Ellenburger was also brought close to the surface during the Devonian and Mississippian and may have experienced some karst modification then. During the Early Pennsylvanian, the Ellenburger experienced hydrothermal processes and tectonic uplift related to the Ouachita Orogeny.

Classification of Paleocave Facies

The facies classification by Loucks and Mescher (2001) (Fig. 12) and the breccia/fracture classification by Loucks (1999) (Fig. 13) were used to describe the collapsed paleocave facies in the Ellenburger at Barnhart field. A discussion of breccia and fracture types is presented in Loucks (2003, his Figure 8). The collapsed-paleocave facies classification (Fig. 12) includes the following facies: (1) *undisturbed host rock*— excellent bedding continuity for tens to hundreds of feet with minor matrix and fracture pores; (2) *disturbed host rock*—bedding continuity is high but folded and offset by small faults and is overprinted with crackle and mosaic brecciation; (3) *collapsed-cave ceiling*—highly disturbed, very discontinuously bedded strata with pockets and layers of chaotic breccia; small-scale folding and faulting are common, as well as overprinting with crackle and mosaic breccia; (4) *collapsed-breccia cavern fill*—ribbon- to tabular-shaped deposits as much as 45 ft across and hundreds of feet long of very poorly sorted, granule- to boulder-sized chaotic breccia clasts 1 to 3 ft long; commonly clast supported but can contain matrix material; (5) *transported-breccia cavern fill*—ribbon- to tabular-shaped deposits as much as 45 ft across and hundreds of feet long composed of clast-supported, moderately sorted, granule- to cobble-sized clasts with varying amounts of matrix; clasts may be imbricated or graded; and (6) *cave-sediment fill*—carbonate and/or siliciclastic debris commonly displaying hydrodynamic sedimentary structures.
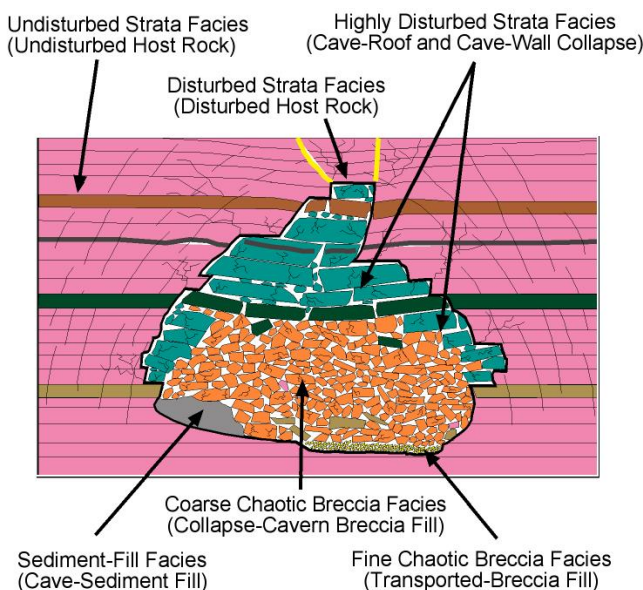
Figure 12. Classification of collapsed paleocave facies. From Loucks and Mescher (2001).
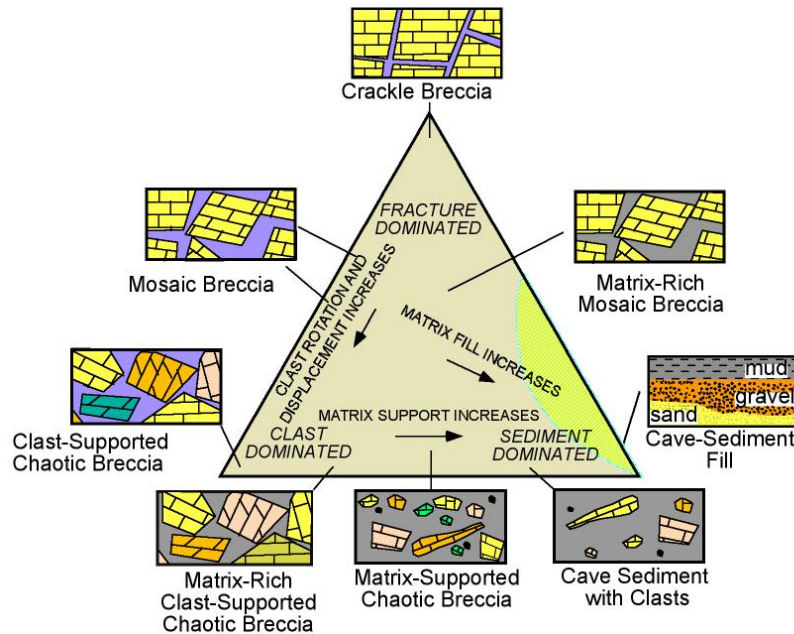
Figure 13. Classification of breccias and cave-sediment fills. Shaded area in the lower right of the diagram indicates that no cave features plot in this area. Cave-sediment fills and breccias can be separated into three end members: crackle breccia, chaotic breccia, and cave-sediment fill. Crackle breccias show slight separation and displacement. Mosaic breccias display some displacement, but they can be fitted back together. Chaotic breccias are composed of displaced clasts that cannot be fitted back together, and they can be composed of clasts of different origins (polymict). Cave-sediment fill can form a matrix within the breccia, as well as support individual clasts. The best reservoir quality is in the matrix-free breccias. From Loucks (1999).

Collapsed-Paleocave Facies in the BEU#3 Core at Barnhart Field

The following paleocave facies were described from the BEU #3 core (Fig. 12): (1) collapsed-cave ceiling facies, (2) coarse-clast collapsed-cavern chaotic facies, (3) fine-clast transported chaotic-breccia facies, and (4) cave-sediment fill facies, including a speleothem. Host rock and disturbed host-rock facies were not cored, but wireline logs and core photographs from the Belco Hickman # 13 cored well (Umphress, 1977) indicate that these facies may make up much of the Ellenburger section in the field. Descriptions below are taken from Combs and others (2003).

Collapsed-Cave-Ceiling Facies: The collapsed-cave-ceiling facies is characterized by large tilted blocks and slabs ranging in size (as seen in core) from 1 ft to over 7 ft (Fig. 14). Matrix-free to matrix-rich chaotic breccias occur between the slabs.

17

The blocks are crackle brecciated, with some of the brecciated fractures forming pores. Ceiling collapse can take place from near the surface down to burial depths of several thousands of feet (Loucks, 1999). Ceiling collapse in the BEU #3 core appears to have started early in the history of the cave, as indicated by transported sediment between the blocks and a speleothem on top of a block. Crackle to mosaic brecciation also appears to have started early, as indicated by sediment-filled fractures. Other fractures occurred late and are filled only by late baroque dolomite cement or very coarse crystalline calcite. Average porosity and permeability values for these rocks are 4.3 percent and 2.16 md, respectively.

Figure 14. Large blocks interpreted to be cave-ceiling collapse. Core depth: 9,031 to 9,041 ft. Goldrus Producing Company Barnhart unit # 3.

Coarse-Clast Collapsed-Cavern Chaotic Facies: This paleocave facies is composed of large blocks that fell from the cave ceiling or walls (Fig. 15). These blocks are too large to have been transported laterally and thus rest where they fell to the floor of the cavern. Blocks commonly display crackle brecciation. In the core, this facies appears similar to the collapsed-cave ceiling facies, and it is difficult to discern between the two facies. Generally the collapsed-cavern facies is more chaotic, and the deposit may be polymictic (implying multiple origins).
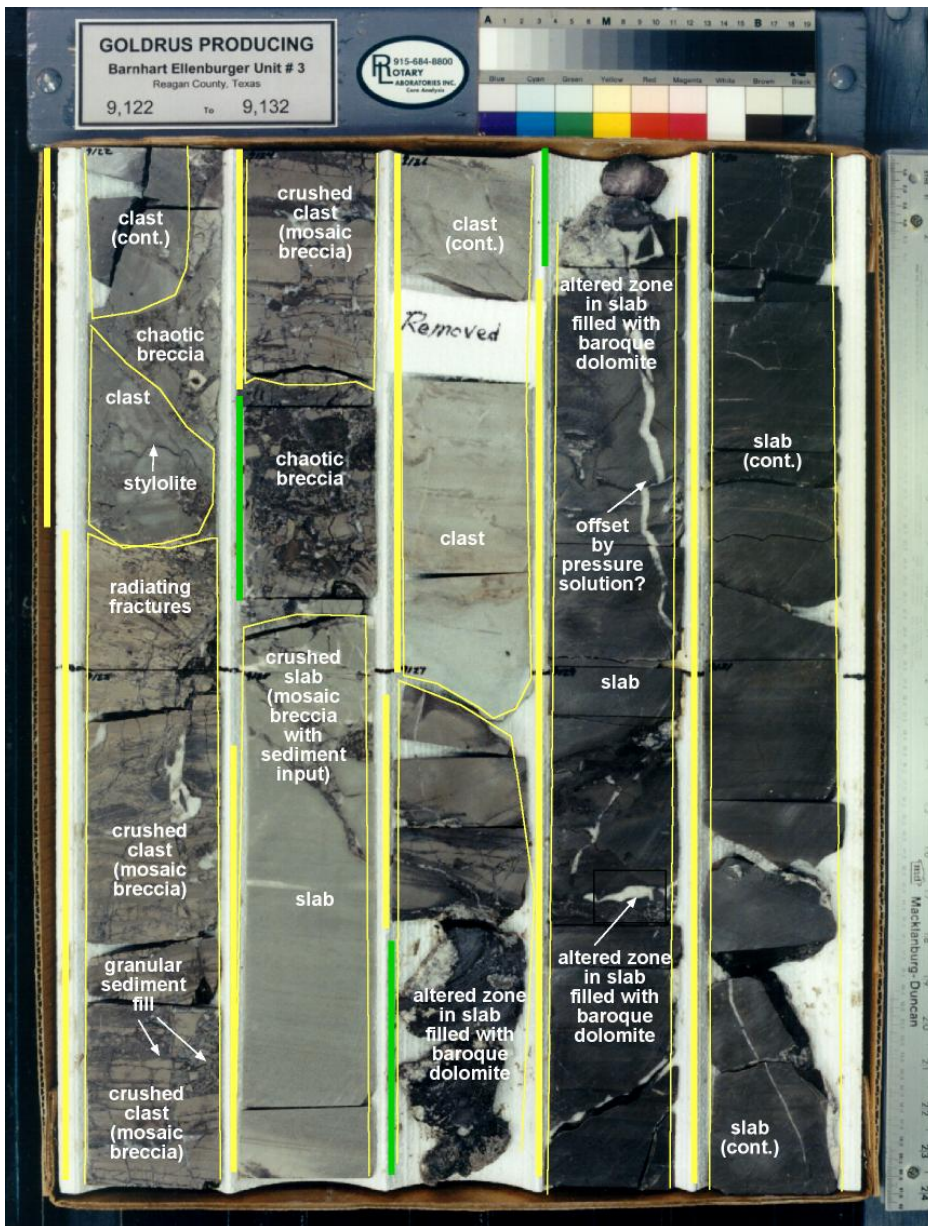
Figure 15. Several large collapsed blocks. Depth: 9,122 to 9,132 ft. Goldrus Producing Company Barnhart Unit # 3.

Fine-Clast Transported Chaotic-Breccia Facies: Smaller clasts, generally less than 4 inches, characterize this paleocave facies (Fig. 16). These chaotic breccias are commonly matrix supported, indicating that they were deposited by debris-flow transport processes (Fig. 17). A few of these fine-clast chaotic breccias are matrix free and contain excellent interclast porosity (Fig. 16).

The matrix between the clasts can range in size from granule- to very fine sand-sized grains (Figs. 18 and 19). The original sediment was carbonate detritus that is now dolomite. The detrital grains exhibit euhedral dolomite overgrowths, as shown in Figures 18 and 19. The average porosity and permeability values seen in these rocks are 6.5 percent and 6.32 md, respectively.
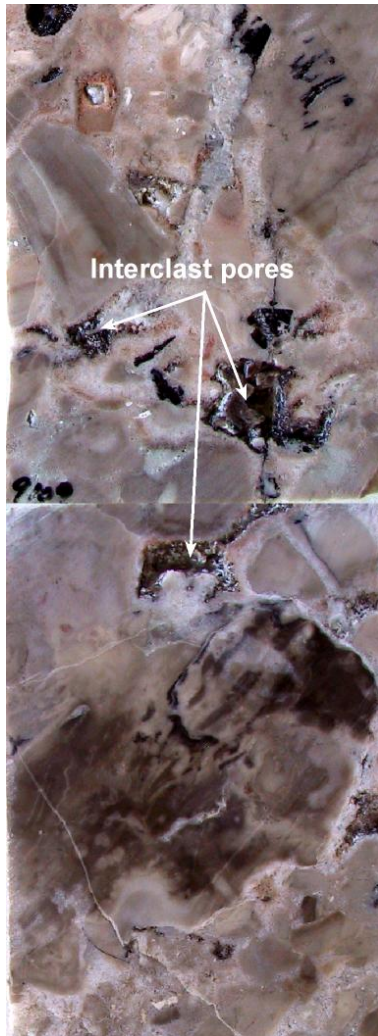
Figure 16. Transported fine-chaotic breccia without matrix. Barnhart Unit #3. Depth: 9,109 ft.

Figure 17. Transported, matrix-rich, fine-chaotic breccias (debris flow). Barnhart Unit #3. Depth: 8,091 to 9,101 ft.
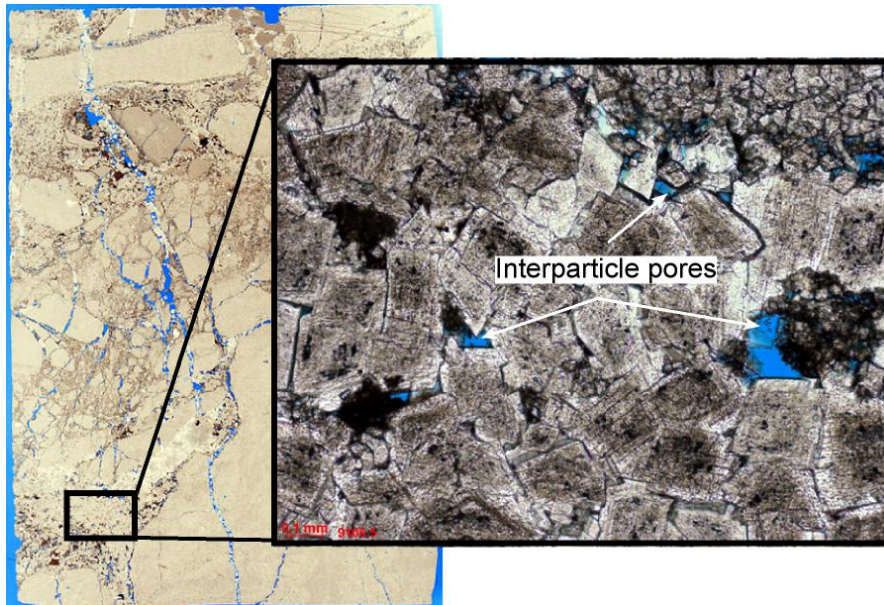
Figure 18. Interparticle pores between sand-sized detrital carbonate with dolomite overgrowths.
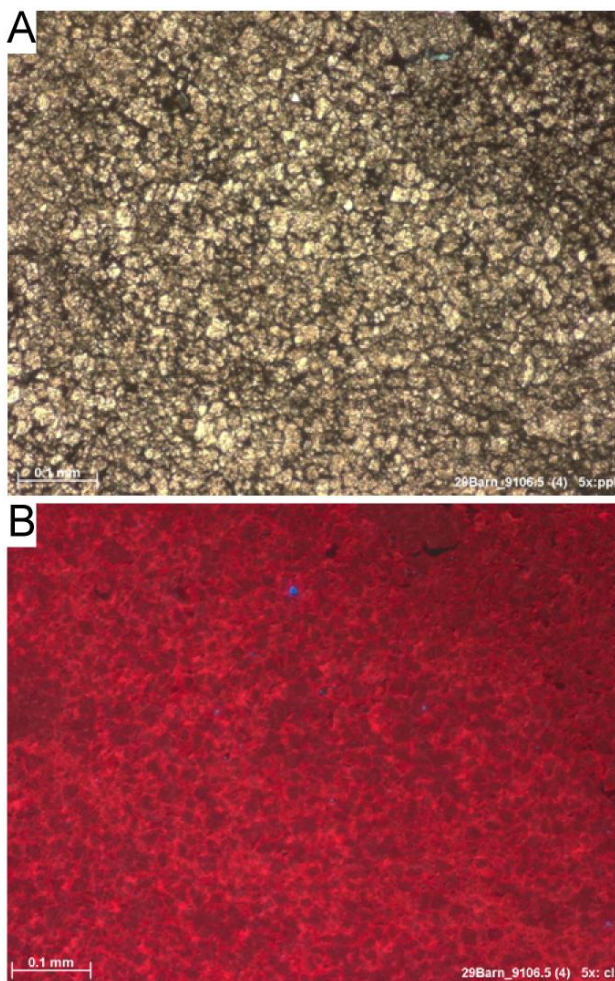
Figure 19. Silt to very fine grained carbonate detrital sediment fill. The detrital grains have dolomite over growths. (A) Plain light microphotograph. (B) Cathodeluminescence microphotograph. Dark spots are the original carbonate detrital grains that show abraded, rounded edges, and the lighter red zones are dolomite euhedral overgrowths.

22

Cave-Sediment-Fill Facies: With the core material available in the BEU #3 well, only a single interval (9062–9063 ft) of fine-grained cave-sediment fill was recognized in this Ellenburger facies. The cave-sediment fill is characterized by laminated mud that is dolomitized and was deposited by suspension processes (Fig. 20). Other cave-sediment fills within this core are clast rich and are better classified as matrix-rich, fine-clast, chaotic breccias deposited as debris flows (Fig. 17). A speleothem (Figs. 20 and 21) is present at 9,663 to 9,365 ft. This typical cave-fill feature formed on top of a collapsed ceiling block and is overlain by fine-grained, cave-sediment fill (Fig. 20). This speleothem, which is characterized by wavy parallel laminations, is interpreted as a stalagmite-type flowstone. Speleothems are excellent evidence of near-surface cave processes. The average porosity and permeability values seen in this unit are 6.4 percent and 0.61 md, respectively.
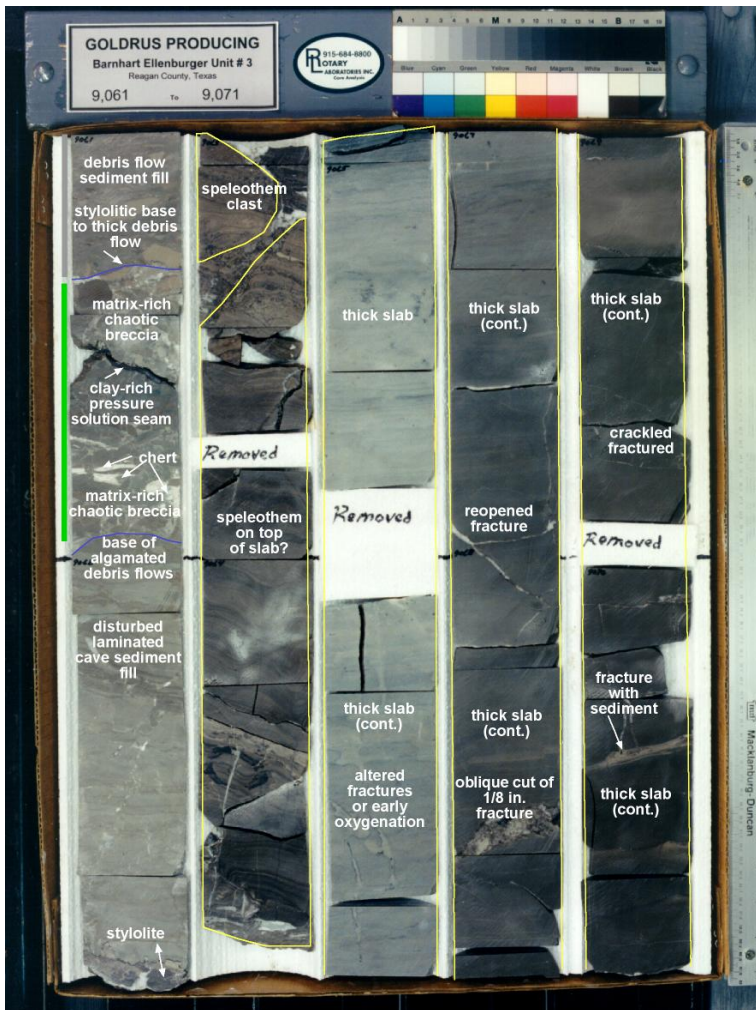
Figure 20. Photograph of laminated cave-sediment fill. Barnhart Unit #3. Depth: 9,061 to 9,071 ft.

Figure 21. Photograph of flowstone-type speleothem. Barnhart Unit #3. Depth: 9,064.5 ft.

Pore Types within the Paleocave Facies

Pore types observed in the BEU #3 core include (1) original host-rock pores within clasts, (2) interclast pores, (3) crackle-breccia pores, (4) mosaic-breccia pores, (5) cave-sediment-fill interparticle pores, (6) solution-vug pores, and (7) regional fracture pores.

Original Host-Rock Pores

Host-rock pores are found within blocks and clasts within the collapsed-paleocave facies. Most of these blocks and clasts exhibit low host-rock porosity, averaging approximately 3.9 percent. Figure 22 illustrates a typical host-rock clast containing intercrystalline pores. The presence of intercrystalline pores within blocks and clasts suggests that the host rock contains layers of these pores separated by tight layers. Estimated mean porosity and permeability in host rocks are less than 5 percent and less than 4 md, respectively.

24
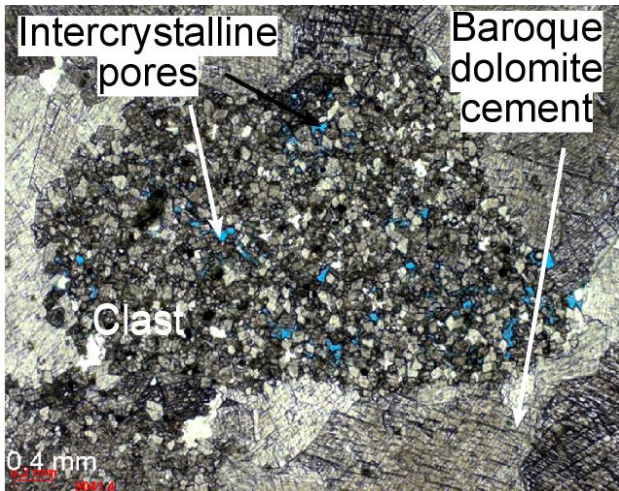
Figure 22. Clast of host rock showing intercrystalline pores. Barnhart Unit #3.

Interclast Pores

Interclast pores occur between the breccia clasts of matrix-free chaotic breccias. In the example shown in Figure 23, baroque dolomite cement has reduced some of the pore space. This type of pore system is limited to the dimensions of the cave void because the origin of the clasts is due to transport in a cavern system. *Large pore spaces such as these are commonly filled with drilling mud, resulting in erroneously low porosity and permeability measurement values.*
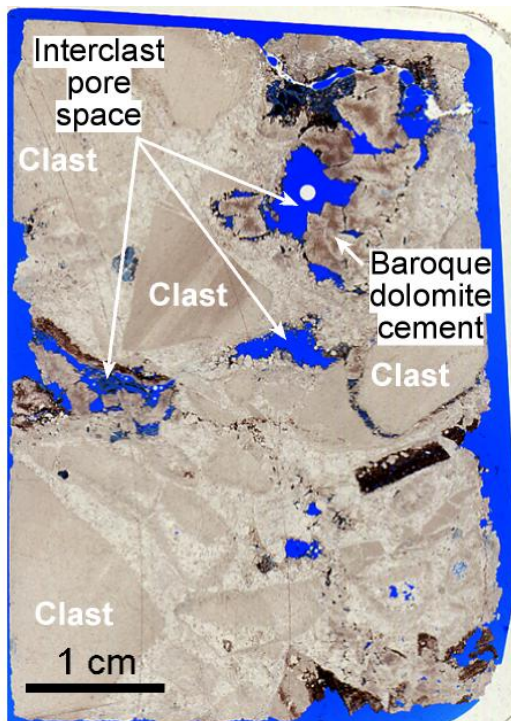
Figure 23. Chaotic breccia with interclast pores. Some of the pore space is occluded with baroque dolomite. Barnhart Unit #3.

Crackle-Breccia to Mosaic-Breccia Pores

Many of the clasts, slabs, and blocks have crackle-breccia to mosaic-breccia-
fracture pores produced by mechanical compaction (Fig. 24). Early-formed fracture pores
commonly contain detrital carbonate sediment (Fig. 24), whereas later-formed fractures
contain only cement (Fig. 25). Crackle-breccia fractures constitute a major pore type in
clasts, slabs, and blocks, and they are assumed to be common in the associated disturbed
host-rock facies.
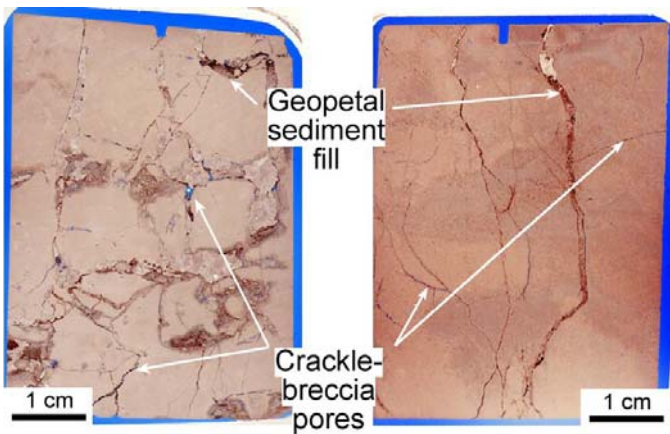
Figure 24. Early-formed, crackle-breccia fracture pores with detrital geopetal sediment. The induced sediment is an early event, transported as suspension load and deposited as water moved through the former cavern. Barnhart Unit #3.

Figure 25. Late-formed, crackle- to mosaic-breccia fracture pores occluded by baroque dolomite. Barnhart Unit #3.

26

Interparticle Pores

Interparticle pores are developed in the cave-sediment fill facies. Most porosity is restricted to coarser sediment fill. Figure 26 shows a thin section of granular-sized clasts in a larger mosaic breccia. Note in this example that some interparticle pore space exists between the granules; however, much of the pore space is cemented by baroque dolomite cement. Finer grained, sand-sized, detrital carbonate also is slightly porous, but much of this porosity has been occluded by dolomite overgrowths (Fig. 18). Finer sediment is impermeable because dolomite overgrowths have occluded all pores (Fig. 19).
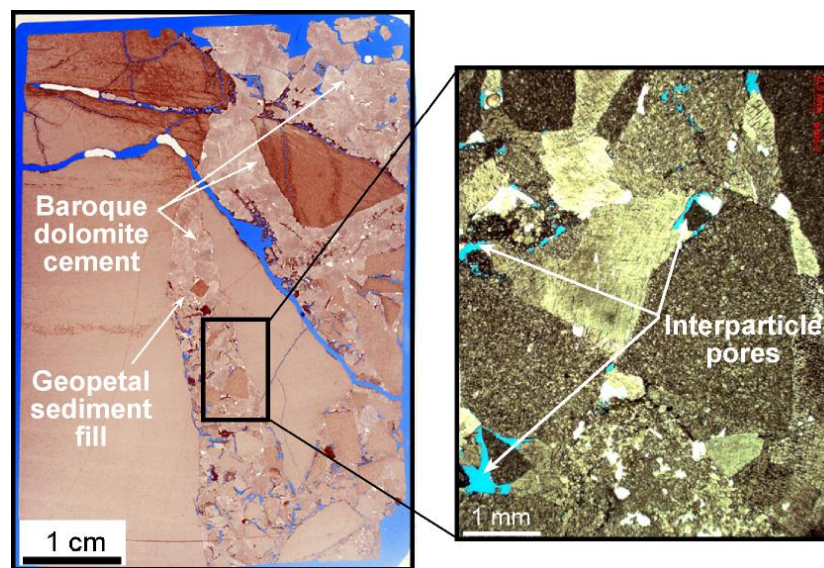
Figure 26. Interparticle pores between clast and granules in a mosaic breccia. Barnhart Unit #3.

Solution-Vug Pores

A macrovug pore is visible in the core at 9,080 to 9,083 ft (Fig. 27A). The full size of this vug cannot be determined from the core or from the image log, but it is at least 3 ft high. It could be a solution cavity or a solution-enlarged fracture. The image log from the BEU #3 well (Fig. 27B) displays the best view of the macrovug. The vug has a small amount of detrital clay, indicating that the vug was open near the surface. During coring, much of the vug was packed with drilling mud.
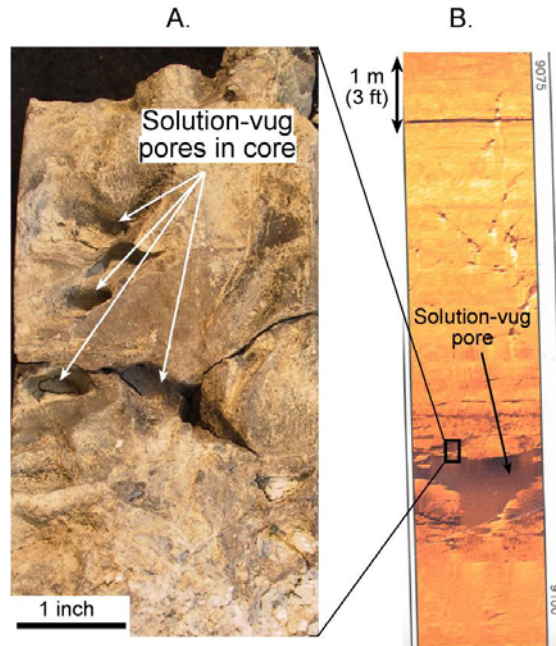
Figure 27. Core slab photograph (A) and image log (B) of a macro-vug showing a solution-etched surface. Barnhart Unit #3.

Regional Fracture Pores

Some late, throughgoing fractures are noted in the core (Fig. 28). These fractures cut well-lithified breccia and cement, indicating that their origin postdates brecciation and baroque dolomite cementation. The baroque dolomite is assumed to be associated with the Pennsylvanian Ouachita Orogeny; therefore, the fractures must be Pennsylvanian or younger in age. Cement occludes the fracture pores; however, other fractures related to this period of deformation may be open in other areas of the field. Origin of the fractures is not clear (Gomez and others, 2001; Combs and others, 2003; Loucks, 2003). They may be related to tectonic stresses during uplift and reburial of the Ellenburger section, or they may be related to mechanical compaction of large blocks coinciding with deep burial.
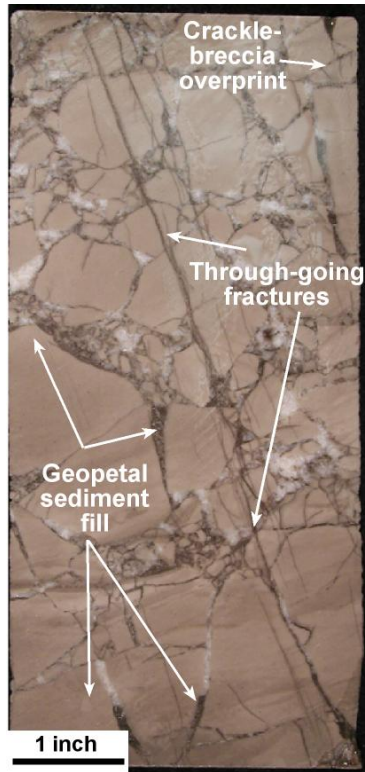
Figure 28. Late-produced throughgoing fractures that cut previously lithified mosaic breccia clasts and baroque dolomite cement. Barnhart Unit #3.

Fractures Associated with Tectonics

In whole core from the Unit #3 well, fractures several tens of centimeters long that crosscut lithified breccia and baroque dolomite were observed (Figs. 28 and 29). Postbrecciation fractures display two approximately orthogonal trends, but the orientation of individual fractures, or groups of fractures in the same section of core, is not determinable because the core is unoriented. We attempted to use the image log to orient the core, but it proved impossible for all but the top 30 ft of core, which has dominantly NW-trending, postbrecciation fractures.
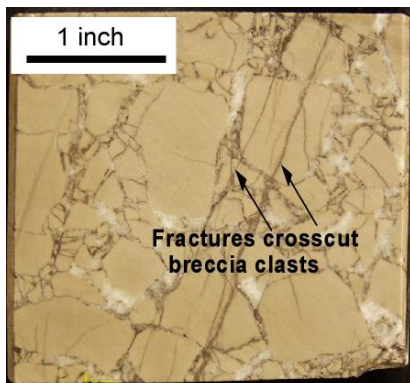
Figure 29. Slab photograph showing fractures crosscutting multiple clasts and upper baroque dolomite cement (white). Goldrus Producing Company Unit #3 core. Depth: 9,050.1ft.

Methods

Our goal was to quantify the fracture intensity and sealing characteristics of postbreccia fractures. To do so we characterized microfractures in sidewall cores from the A1 and A6 wells and in samples from the Unit #3 core in Barnhart field (Fig. 9). The use of microfractures allowed us to collect a large enough population to make predictions about large, potentially open fractures that were not sampled by the sidewall cores or whole core and which probably populate the host rock in the interwell volume. Underlying principles for this approach were outlined by Laubach and others (2000).

Opening-mode-fracture, aperture-sized measurements were collected for a NE-trending fracture set from oriented sidewall cores in the A1 well from depths of 9,055 and 9,087 ft and from the dominant set in samples from the Unit #3 well at 9,070 ft and 9,079 ft. Microfractures were measured using image mosaics collected on a scanning electron microscope with a cathodoluminescence detector for the A1 well samples and for the Unit #3 9,070-ft sample. Detectors and processing used for these images record CL emissions in the range of ultraviolet through visible into near infrared and convert them to gray-scale intensity values. All images were acquired using an Oxford Instruments MonoCL2 system attached to a Philips XL30 SEM operating at 15 kV. For the 9,079-ft Unit #3 sample, the image mosaic was collected using cathodoluminescence on a transmitted light microscope.

Microstructures were imaged on polished thin sections cut parallel to bedding. Scanned-CL photographs were taken in traverses several millimeters in length and stitched electronically into mosaics. Typically a mosaic of 30 to 40 individual images at a scale of 1:150 is required to record a continuous CL image along the short side of a 2.65 × 5.3 cm thin section. To increase the likelihood of intersecting microfractures genetically related and parallel to macrofractures, mosaics were oriented perpendicular to known macrofracture strike. An example of a portion of an image mosaic is shown in Figure 30. Different dolomite cements and calcite cements are distinguished on the basis of degree and type of luminescence (Reed and Milliken, 2003) and by using secondary electron images of the same area. Orientation and size were mapped electronically using commercially available software (Canvas 5.0) by defining four points—the two fracture

tips and two opposite points on the fracture walls at the widest aperture. Fracture attributes were measured and compiled using in-house software that uses the digitized parts of the four points to calculate length, aperture, and orientation (Ortega, 2002). The area of the CL mosaic is also calculated using image-processing software.
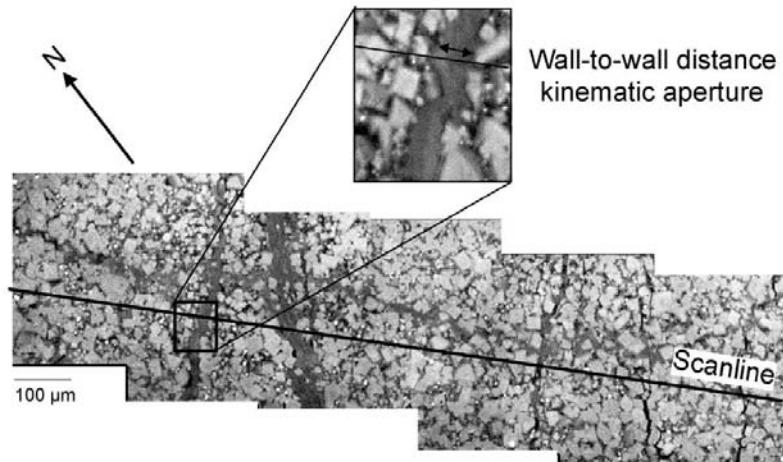
Figure 30. SEM-CL image mosaic of fractures from the A1 well sidewall core at 9,055-ft depth. Fracture apertures for the NE-trending set were measured along a scanline for a 1-D analysis.

Kinematic apertures of opening-mode fractures were measured along scanlines normal to fracture strike for one-dimensional analysis. Maximum kinematic apertures of fractures within a mosaic area were measured for two-dimensional analysis. Kinematic aperture, the wall-to-wall distance normal to the fracture, is independent of whether the fracture is open. Aperture data are presented on cumulative frequency plots of fracture apertures, normalized to scanline length or area (Fig. 31).
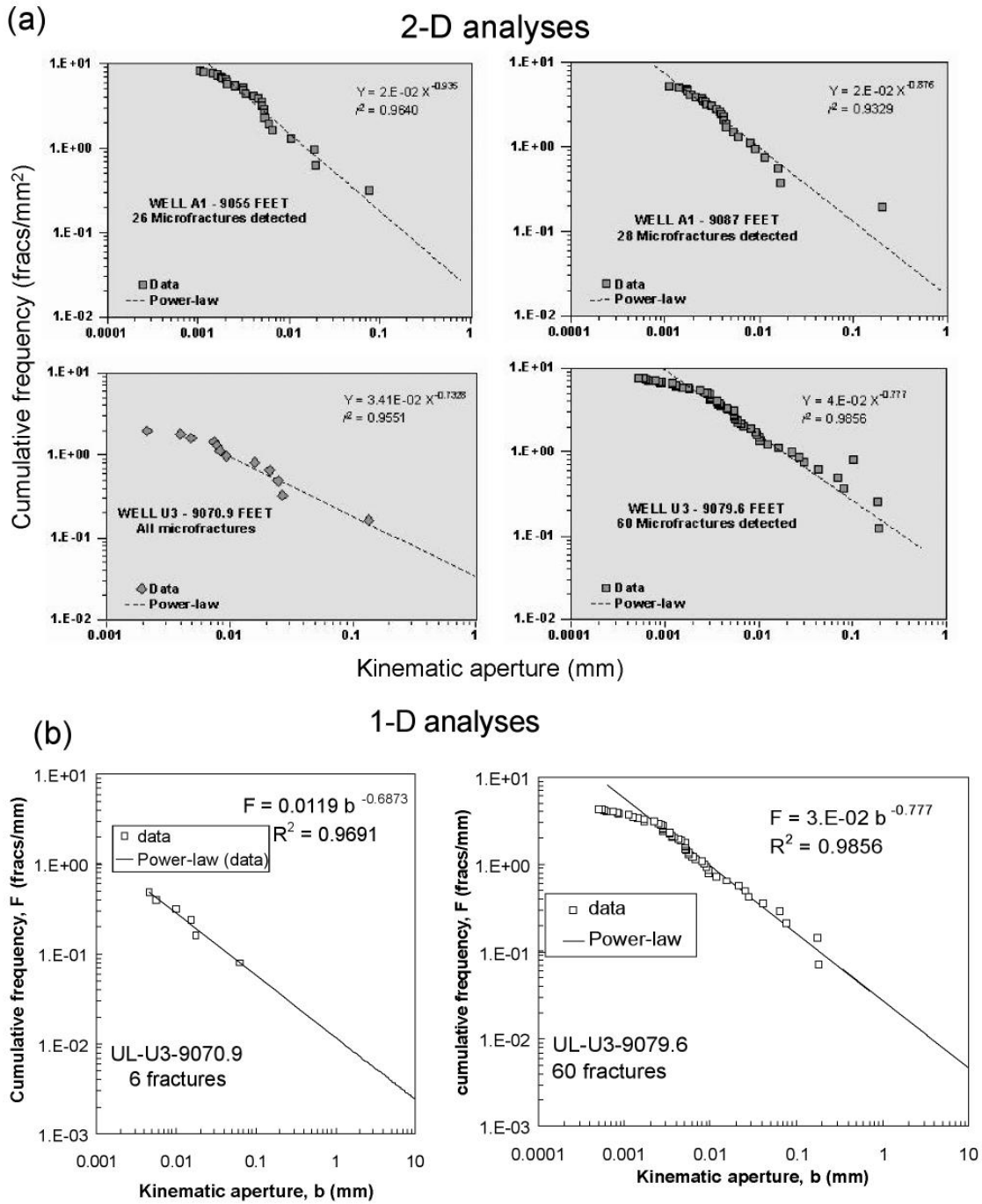
Figure 31. Aperture-size distribution cumulative-frequency plots. Data are fit to a function that models truncation and censoring at either end of the data set as well as a power law (straight line on a log-log plot) for the main part of the data. Only the power law is shown, but the correlation coefficient applies to the whole function. (a) 2-D data from A1 well, 9,055- and 9,087-ft depths and the Unit #3 well, 9,070.9- and 9,079.6-ft depths (b) 1-D data for Unit #3 well from depths 9,070.9- and 9,079.6-ft depths.

The data are fit to a power-law function of the form F = ab-c, where F is cumulative fracture frequency, a is the coefficient, b is the fracture aperture, and c is the exponent of the power-law relationship. Where these parameters can be delineated for microfracture size distributions, the equations can be used to predict the distribution of sizes of macrofractures in the same volume of rock (Marrett, 1996). Power-law distribution coefficients may be thought of as a measure of fracture intensity at a given size. For example, if b = 1, then the equation simplifies to F = a. Exponents reflect the slope of the power law on a log-log plot. Data show departures from a power-law function at high and low ends of the measured size range. These are recognized as truncation and censoring sampling artifacts (Marrett and others, 1999).

Fracture Intensity Results

The utility of cumulative frequency plots is that the power law may be extrapolated to give a measure of predicted fracture intensity, in terms of the number of fractures per unit length of scanline, for any given aperture size. In dolomites fracture porosity may typically be found in submillimeter-wide fractures, but for fractures to be effective conduits for fluid flow they probably need to be at least 1 mm wide. The power law is extrapolated to aperture sizes of up to 1 mm (Fig. 31a) and 10 mm (Fig. 31b).

Fracture intensity must be reported in reference to the fracture aperture being considered. Here, fracture intensities are reported for fractures more than or equal to 1 mm in width. For the 2-D A1 well samples from depths of 9,087 ft and 9,087 ft, intensity was 0.018 and 0.02 fractures/mm^2, respectively. For the 2-D Unit #3 well analyses of samples from depths of 9,070.9 ft and 9,079.6 ft, intensity was 0.034 and 0.04 fractures/mm^2, respectively (Fig. 21a). For 1-D analysis using a scanline rather than a mosaic area to collect the fracture aperture data, Unit #3 samples yielded intensities of 0.012 and 0.03 fractures/mm, for fractures more than or equal to 1 mm in width (Fig. 31b).

Fracture intensities from different samples may be compared. Fracture intensity for the NE-trending set at different depths in the A1 well was not significantly different, suggesting that for those depths tested, opening-mode fracture response was similar.

Intensities measured in the Unit #3 well were slightly higher than those in the A1 well. In the Unit #3 well, opening-mode fracture intensity is also high relative to most other fractured carbonates we have measured (Fig. 32). The inverse of cumulative frequency (fractures/meters) is average fracture spacing (meters/fracture). Although fractures are generally not evenly spaced and tend to be clustered, we used the average spacing measure as an alternative way to represent fracture intensity. In the Unit #3 well fractures with kinematic apertures (wall-to-wall distance across fracture, irrespective of fill) of 10 cm are predicted to be spaced 6 to 15 ft apart.
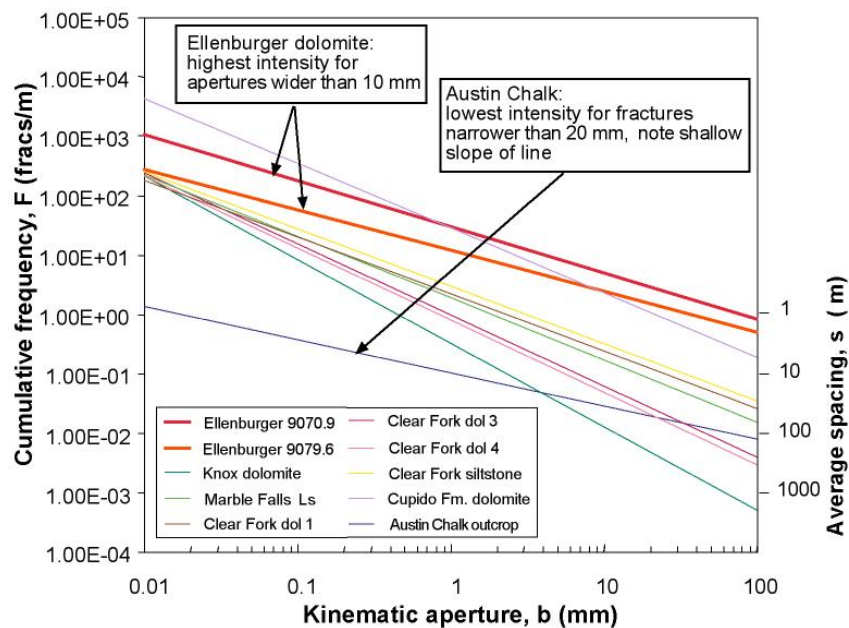
Figure 32. Cumulative-frequency plot for 1-D aperture-size distributions of various carbonates. The Ellenburger samples from 9,070.9 ft and 9,079.6 ft from the Unit #3 well (shown in heavy lines) plot near the top of the range of curves, indicating that fracture intensity is relatively high in the Unit #3 well.

Fracture Timing and Sealing Results

Principles of fracture sealing mechanisms were discussed fully by Laubach (2003). Fracture sealing takes place by two different processes, one synchronous with fracture opening (synkinematic), the other postdating the opening event (postkinematic). The question of whether a fracture will remain open in the subsurface depends on the operation of both processes. The first sealing process tends to seal the smallest fractures

in a population but leaves larger fractures open. The second process may completely occlude remaining porosity in the large fractures.

Scanning-electron-microscope-based cathodoluminescence (SEM/CL) allows the detection of microfractures that otherwise would remain invisible because of their small size and because the cement precipitated in them is in optical continuity with crystals in the wall rock. SEM/CL revealed that fractures formed after a phase of dolomite replacement because fractures have a distinct morphology, indicating that they grew initially by propagation along rhombohedral dolomite-grain boundaries (Fig. 33).
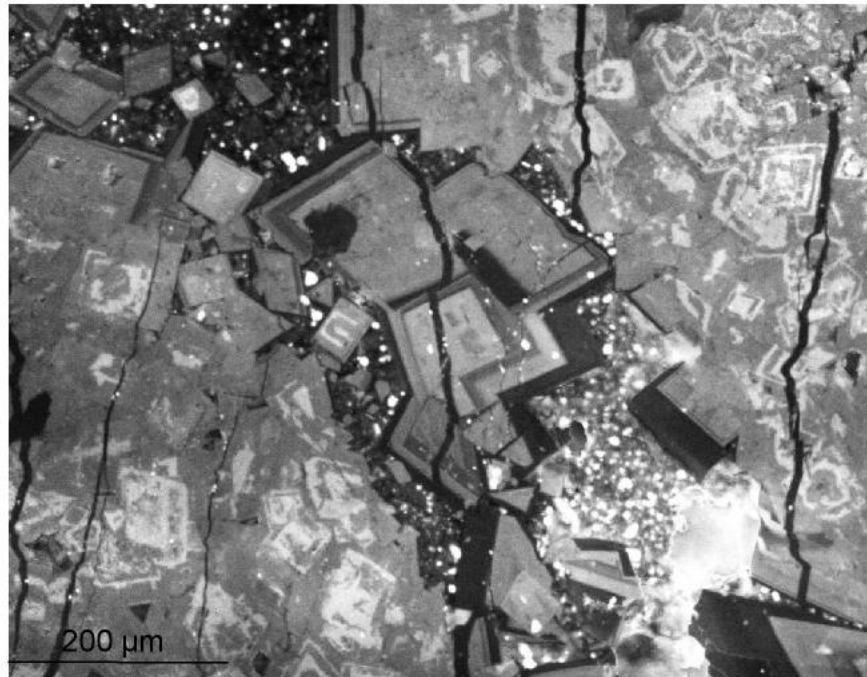
Figure 33. Cathode luminescence photomicrograph of dolomite showing fractures sealed with low-luminescence cement. Note that cements follow internal and external rhombohedral dolomite crystal boundaries, indicating that the rock was dolomitized prior to fracture propagation. In addition, note zoning of the host-rock dolomite. The external zones are also low-luminescence dolomite, which precipitated in the host rock at the same time as in the fractures.

A low-luminescence dolomite cement precipitated during fracturing (synkinematic) and formed cement bridges and a fracture lining. Evidence of synkinematic cement is provided by the presence of crack-seal structure (Fig. 34). Fractures repeatedly open and seal with cement of the same composition, producing bands of wall-rock and/or fluid inclusions within the fracture. A different, medium-luminescence dolomite cement precipitated during (synkinematic) and after

(postkinematic) the two main sets of fractures developed. Calcite cement is also present, but precipitation occurred only after all fractures formed (postkinematic) (Fig. 35). Qualitative element mapping on the SEM reveals that the low-luminescence dolomite is Fe rich and Mg poor, relative to the other dolomites. Distribution of postkinematic calcite, and, hence, open fractures, was variable. We observed fracture porosity in some fractures in the A1 well, but most fractures in the Unit #3 well were occluded by calcite.

Bands of wall-rock inclusions

Fractures sealed with low-luminescent dolomite

200 µm
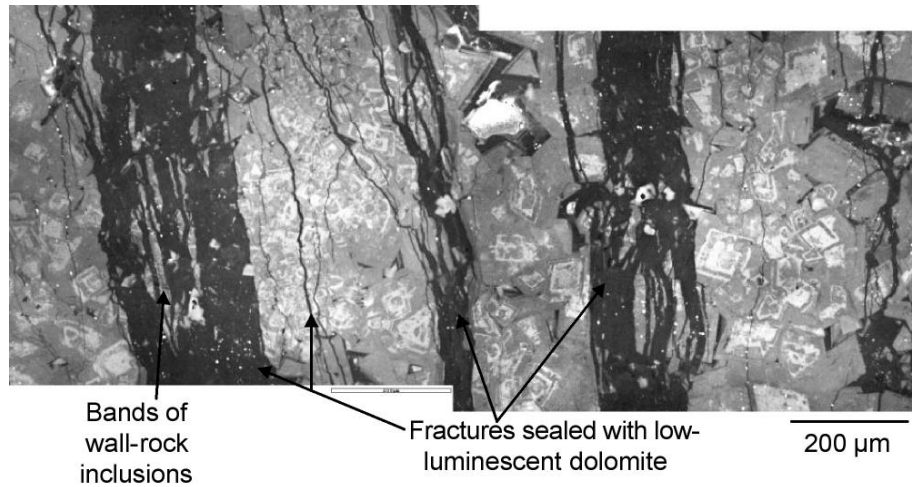
Figure 34. Crack-seal structure in fractures from the Unit #3 well at 9,079.6 ft. Fractures are sealed with low-luminescence dolomite (black). In each fracture bands of wall rock inclusions are entrained within the fracture as a result of multiple opening events. Some of these inclusions have dolomite zoning in the host rock preserved.

SEI   CL

200 microns
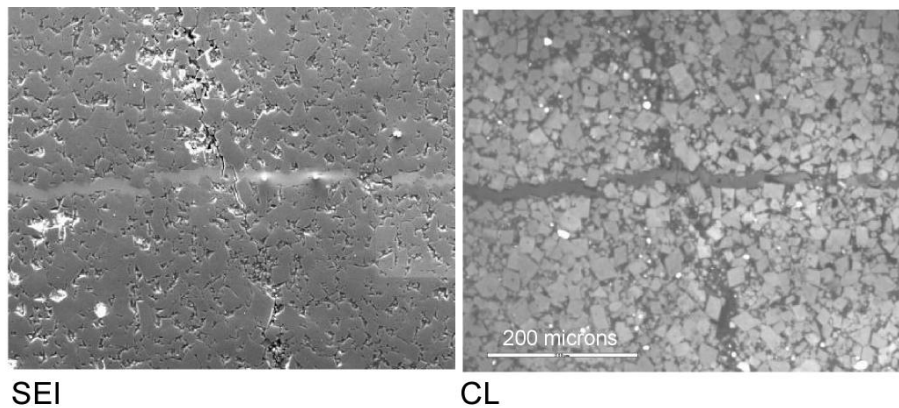
Figure 35. Secondary electron image (SEI) and cathodoluminescence image (CL) of fractures in the A1 well at 9,055 ft. Fracture trending across the page from left to right is completely sealed. It contains very small amounts of low-luminescent dolomite (black) as a lining on the fracture wall (synkinematic cement) and is filled with a medium-luminescent postkinematic cement, which in the SEI image shows as pale-gray calcite, being distinct from the darker gray dolomite.

Although it is not possible to know whether fractures in the sidewall cores are part of the same set, owing to lack of crosscutting relations in the sidewall cores, they have the same temporal relationship with dolomite and calcite cements. Because the whole core could not be oriented, we cannot know which of the two fracture sets identified on the image log we have measured in the Unit #3 well. At this stage we consider it likely that the NE-trending fractures in the A1 well are contemporaneous with the dominant set at 9,070 to 9,079 ft in the Unit #3 well. Fracture orientations measured in the core were separated into different depth categories on the basis of dominant orientation of fractures in the image log over given depth ranges.

Observations

Fractures that crosscut clasts and cement and, therefore, postdate brecciation were identified in the Unit #3 core. These fractures form continuous features in the core and have been identified on image logs in this well. Results from sidewall cores and borehole images from a recent well confirmed the orientation of two sets of fractures (S70E/90 and S30W/90) in Barnhart field. These fracture sets appear to be broadly synchronous, but their origin has not yet been determined. They may be related to late-stage cave collapse or to some more regionally widespread tectonic event.

It is possible to measure fracture intensity of microfracture populations that are subsets of the fracture sets observed in the core using SEM-based cathodoluminescence techniques specially adapted for carbonate imaging. Fracture intensity was obtained for samples from different depths from two wells in Barnhart field. Intensity within wells was consistent, but the Unit #3 well showed a higher intensity than the A1 well. Samples from additional depths and other wells are required to confirm whether there are variable fracture intensities from well to well and to what extent each intensity level persists both vertically and laterally.

Postbrecciation fractures propagated along dolomite-grain boundaries, and this fracturing event was therefore interpreted to have occurred after dolomitization of the host rock. Two compositionally different dolomite cements precipitated during fracture opening and show crack-seal structure. The more abundant of these cements also precipitated after fracture opening, as did calcite. Calcite is responsible for occlusion of

fracture porosity in the larger fractures. It is variably distributed. At this stage, although we cannot predict the distribution of calcite cements in Barnhart field, we can identify its presence on a site-specific basis using thin sections and thereby predict where large fractures would be sealed, even if we have not sampled them directly.

RESERVOIR ARCHTECTURE AND CONTINUITY

Keys to analysis of the reservoir architecture (or internal stratigraphy) are calibration and interpretation of wireline-log response to lithology and facies. The gamma-ray log, a common log of choice in establishing lithologic correlations in carbonate rocks, typically exhibits a uniformly low response in Ellenburger sections in the Permian Basin. This low response is a result of the essentially siliciclastic-free environment in which the shallow-water platform carbonate sediments of the Ellenburger were deposited. Umphress (1977) used core and log data from the Belco Hickman #13 well to demonstrate that local zones of high gamma-ray response correlate with intervals of clay-filled fractures. Our analysis of these and other core data in the field suggests that both the clays and abundant "fractures" are related to local development of breccias, dissolution zones, and internal sediment fill that are all related to the karst-forming processes. The high gamma-ray zones described by Umphress are perhaps most common in the upper part of the Ellenburger at Barnhart, but they can be observed at almost any depth. Similar karst-related, high gamma-ray zones have been described in other carbonate units that have been exposed to karsting (e.g., Devonian Thirtyone Formation, Ruppel and Holtz, 1994). Such zones are probably relatively local in development and thus are not likely to be accurate stratigraphic markers. In any case, gamma-ray logs are available for only a few wells at Barnhart field.

By far the most common wireline-log types available at Barnhart are SP and resistivity logs. Although SP logs appear to exhibit no usable relationship to stratigraphy or other reservoir attribute, our examination of resistivity-log response suggests that they are indicators of local reservoir porosity and stratigraphy. (See section on reservoir petrophysics for a more extensive discussion of this relationship.) Accordingly, we used resistivity logs to develop a correlation framework for the Ellenburger across the field.

38

Figure 37 depicts the stratigraphic architecture defined by resistivity-log correlation in the south part of the Goldrus Ellenburger Unit. Not all wells in the field, however, display these well-defined resistivity changes. The resistivity-log response from the BEU #3 well, for example, shows no obvious correlation to the zones apparent in adjacent wells (Fig. 36). As we have documented elsewhere in this report, our studies of the cores from this well illustrate that the Ellenburger section in this area is dominated by karst breccias and cave fill. We interpret the absence of resistivity markers in this well to be due to the presence of these collapsed-cave deposits and disruption of the local stratigraphy. With the exception of the area around the BEU #3 well, however, there is strong wireline-log evidence of good stratigraphic continuity among the wells in the area currently being developed by Goldrus.
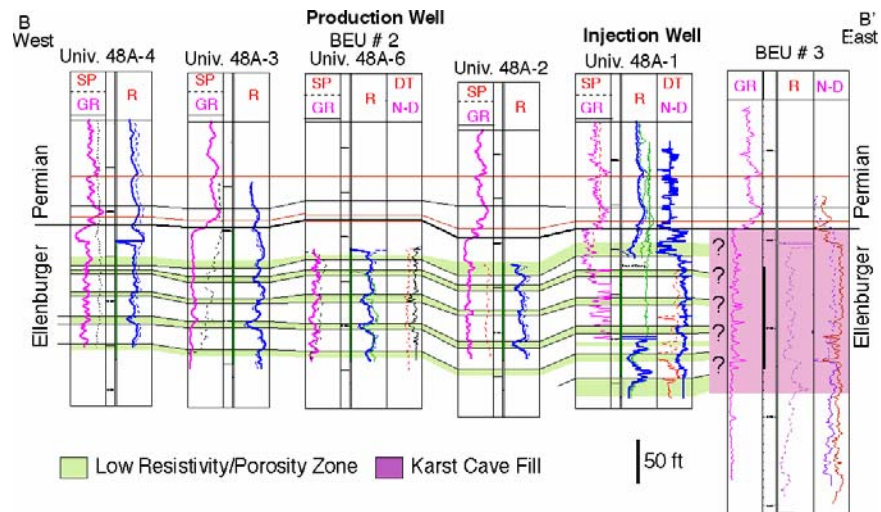
Figure 36. Cross section B-B′ showing internal architecture of the Ellenburger at Barnhart field, which is based on resistivity-log correlations.

Areas of noncorrelative resistivity-log response are also apparent elsewhere in the field. These areas may also be due to the local development of karst deposits. Examples of areas interpreted as such are shown in Figure 4. Some of these zones of noncorrelation or discontinuity are more linear (Fig. 4). Because they appear to be linear, these may represent fault or fracture zones or the linear development of karst features along such a zone.

Impact of Karst Processes on Reservoir Continuity

The Ellenburger section seen in the BEU #3 core (Fig. 37) and other cores (Figs. 38 and 39) is an excellent example of a collapsed-paleocave system. The gravity-flow-sediment deposits (Fig. 17) and the speleothem (Fig. 21) are strong indicators that parts of the cored intervals represent open cavities that were subsequently infilled. The extent of the cavities cannot be determined with the available control, but the thickness of the paleocave deposit indicates that the cavern feature was significant. The paleocave section in the BEU #3 core is probably the amalgamation of several cave levels. The cave-sediment fill and debris-flow intervals represent former passages, whereas the large blocks and slabs represent the now-collapsed cave ceiling or cave floor between the former passages. Burial compaction coalesced the cave system into a complex heterogeneous body of breccia, fractures, and sediment fill.
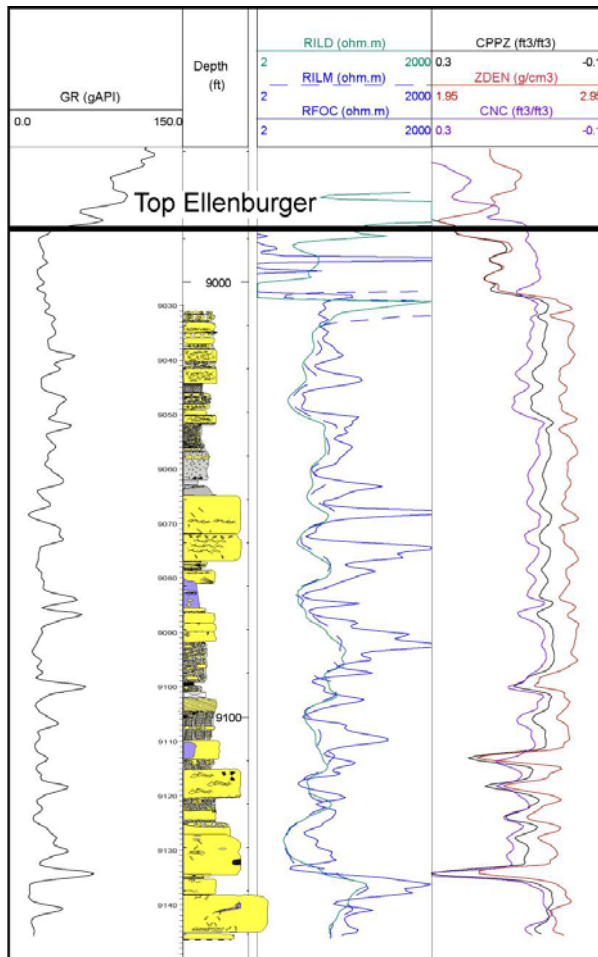
Figure 37. Calibration of Goldrus Producing Company Unit #3 core to wireline logs. Core-log relationships provide a basis for recognition of karsted and nonkarsted sections. See Figure 10 for details of core description.
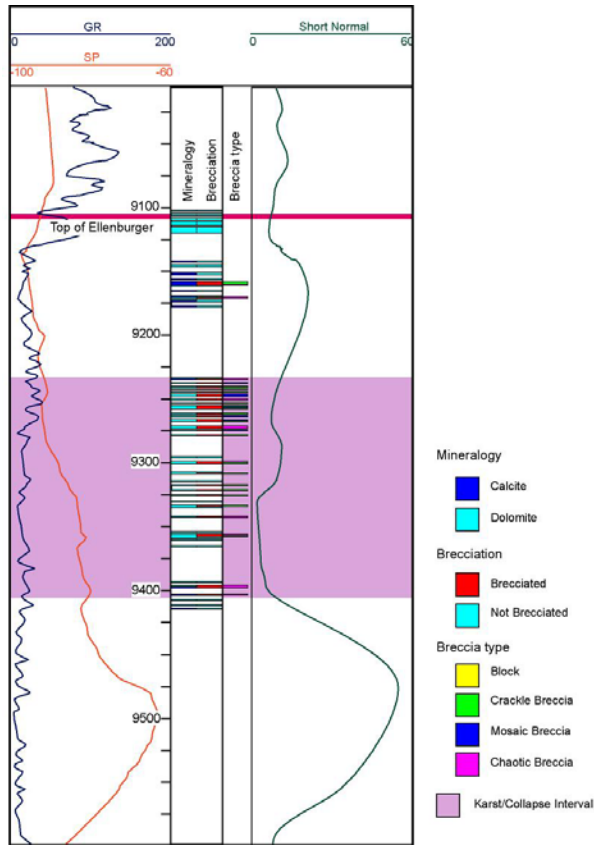
Figure 38. University #48-F-1 well showing distribution of karst-collapse features, which is based on examination of core chip samples.
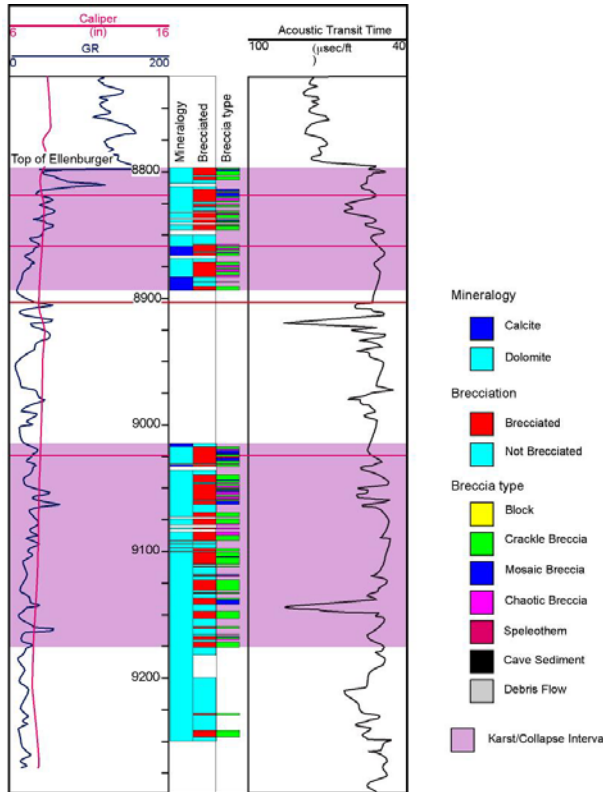
Figure 39. Core description and interpretation of the Hickman #13 cored well showing distribution of karst-collapse facies.

The resulting pore network from this coalesced, collapsed-paleocave system is complex and heterogeneous. A number of pore types compose the pore network, and their distribution is variable. Regional fractures or other large-scale mechanical compaction fractures may overprint the paleocave facies and act as a connecting pore network that joins all paleocave-related pore types. The paleocave deposits are just one component of the facies heterogeneity in Barnhart field. The original host rock may make up the greatest volume (storage capacity) of the reservoir. The paleocave facies and associated pore network are a complicating factor that must be considered in developing flow models of Barnhart field.

Effects of Fractures and Faults

The structural history of the Barnhart field area suggests that tectonic fractures are likely in the area. It is apparent that uplift of the field area took place at least two and perhaps more times during the Paleozoic. Faulting is certain to have occurred during at the least the last of these uplift episodes (Pennsylvanian), when the Ellenburger was exposed to the surface. As discussed previously, correlation discontinuity zones defined by wireline mapping suggest the possibility of faults or fracture zones in the field. However, no faults or zones of fracturing have yet been definitively recognized in the field. A preliminary study of apparent fractures in sidewall cores from two wells recently reentered and cored by Goldrus (48A#6 and 48A#1; Fig. 4) that was conducted by Gomez and others (2001) concluded that evidence of microfractures had developed along two dominant azimuths: NE and NW. However, more recent analysis of whole core from the BEU #3 core suggests that some of these apparent tectonic fractures may actually be associated more with karst-forming processes than tectonic processes (Gale and Gomez, in press). It may be that fractures are principally relatively small and discontinuous. If so, they may act to increase the interconnectedness of karsted and unkarsted areas and facies and increase the effective permeability of the reservoir section.

Overall, reservoir continuity is thought to be good because breccias and fractures associated with the collapse of the paleocave system during burial probably serve to connect most of the pore networks, including relict matrix pores and collapsed-paleocave breccia pores. As described earlier, regional throughgoing fractures may be present,

42

although these regional fractures may not be as abundant as collapsed-paleocave fractures. If present, however, they could create highly permeable pathways and, hence, possible rapid breakthrough.

Implications of Historical Production and Pressure Response

Despite log- and core-based indications of reservoir heterogeneities and discontinuities, historical and spatial trends in production and pressure decline suggest that the Ellenburger reservoir at Barnhart field is reasonably well interconnected. In terms of initial production rates, pressure decline, and primary production response, the reservoir resembles many other matrix-dominated solution-gas-drive reservoirs in the Permian Basin. For example, analysis of initial rates by the authors and by John Lomax (Goldrus Producing Co., personal communication, 2003) has revealed that many Barnhart wells began production at high producing rates and rapidly declined. Plots of annual production rates (Fig. 5) show that field production volumes began to fall rapidly about 5 to 6 years after major development was complete. Mapping of spatial trends in cumulative production by Lomax (reported in Kuhlman, 2004) suggests that primary production has been relatively uniform on a conventional drainage area to production volume basis. All of these characteristics are typical of the prolific Permian solution-gas-drive carbonate reservoirs (for example, San Andres and Grayburg) in the Permian Basin. These reservoirs, all of which contain few if any known fractures, commonly displayed initial production rates as high as 1,000 to 1,500 bopd (for example, Ruppel and Cander, 1988). They also commonly experienced rapid declines in pressure and production after about 5 years of full production. Finally, they characteristically show a close relationship between primary production response and drainage area (subject to phi-h variations). Interestingly, primary production totals from these Permian carbonate reservoirs are more typically lower than the 14 percent currently recovered at Barnhart. In San Andres reservoirs, for example, recovery efficiencies commonly totaled 10 to14 percent (before the onset of secondary or tertiary recovery activities). In short, the Barnhart Ellenburger reservoir displays production and pressure characteristics that are typical of most solution-gas drives in conventional, matrix-dominated reservoirs.

CORE AND WIRELINE-LOG PETROPHYSICS

Introduction

Three wells having core data are available for petrophysical analysis of the Barnhart Ellenburger reservoir: the Hickman #13, University 48A #6 (BEU # 2), and BEU #3. Data for the BEU #3 core, acquired in 2001, are whole-core data, including porosity, horizontal and vertical permeability, and grain-density data. The University 48A #6 (BEU #2) core-analysis data are from rotary sidewall cores and comprise porosity, permeability, and grain-density data, along with Klinkenburg permeability measurements. Because original data for the Hickman #13 core were not available at the time of this study, this core was not used for this report.

The 107 wells in the field with wireline logs can be subdivided into three groups representing different vintages. The oldest group, containing 95 wells, represents initial development of the reservoir and is limited to electric log suites, laterals, normals, and limestone laterals. Although work to convert these logs into reliable wireline data through resistivity-log inversion has begun, these logs were not considered for the current report. The second group, representing wells drilled in the late 1960's, contains nine wells that have sidewall neutron porosity (SNP) logs or gamma-ray neutron (GRN) porosity logs. The final group of three wells contains more modern log suites, including density, neutron, and photoelectric factor logs and some acoustic and resistivity-log suites. Two of these wells, both of which were drilled and logged by Goldrus Producing Company, are reentries into older wells (University 48A #6 [BEU # 2], and University 48A #1 [BEU # 1]) and one is a new drill (BEU #3). These three wells are the primary source of data for this report.

Core Analysis Data

Given the two available core analysis data sets, porosity in the Barnhart Ellenburger reservoir is approximately normally distributed between about 2 and 8 percent porosity and averages about 5 percent. Approximately 10 percent of the data include porosities greater than 10 percent (Fig. 40).
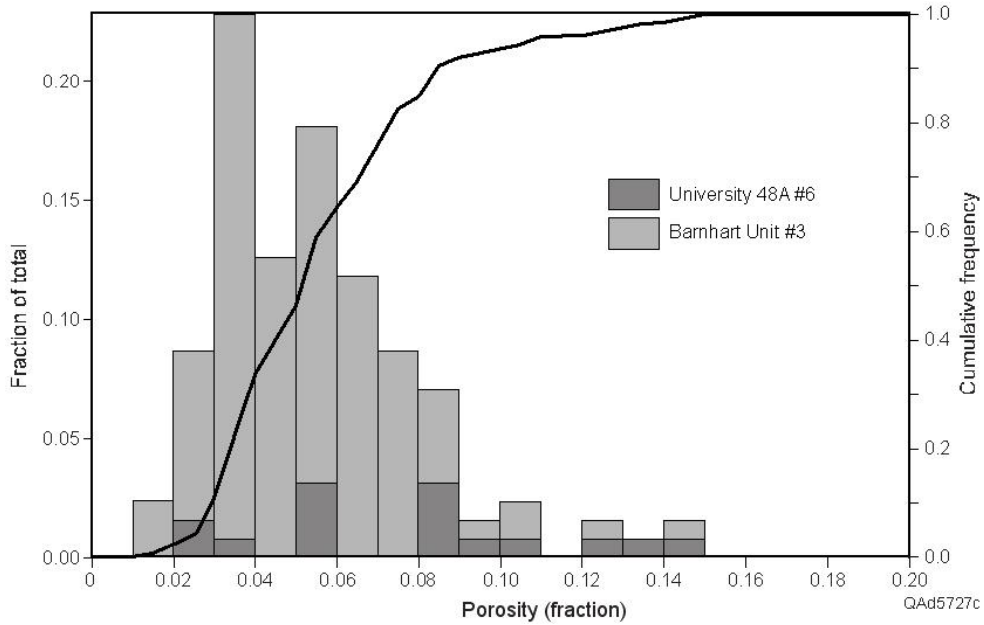
Figure 40. Plot of core porosity data for the Goldrus Barnhart Unit # 3 core. Note generally normal shape of histogram below 8 percent porosity. Approximately 10 percent of data lie below 10 percent porosity.

Grain-density data indicate that most of the cored intervals are dolostone, and most of the data are grouped around 2.84 g/cc, a typical density of dolomite in the Permian Basin (Fig. 41). About 5 percent of the data fall in the 2.71 g/cc range, indicating the presence of minor amounts of limestone.
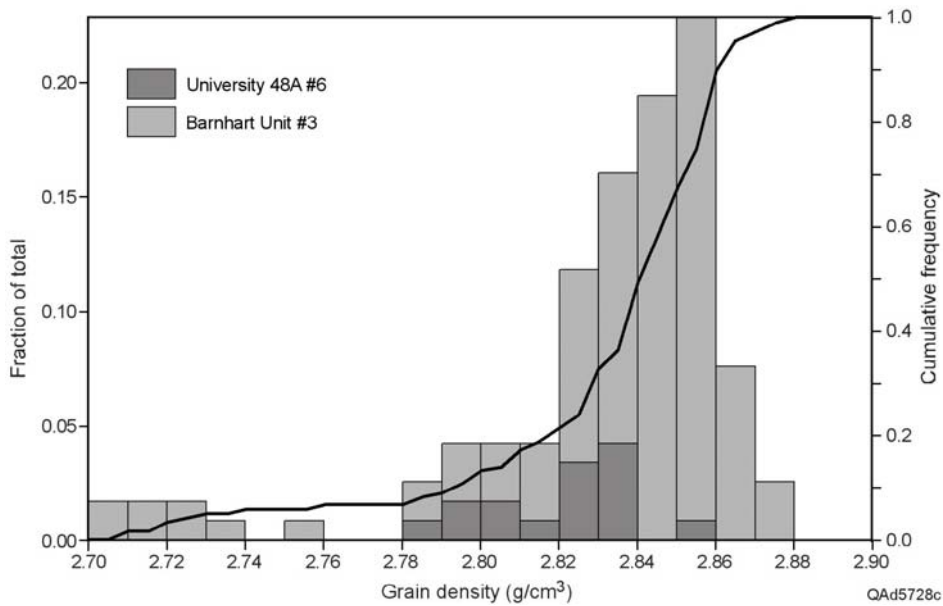
Figure 41. Plot of grain-density data for Goldrus Barnhart Unit # 3 core. Note that data are dominated by dolostone with minor limestone.

45

Horizontal-permeability data (Fig. 42) indicate an average permeability of about 2 md. Sidewall core-plug data from the University 48A #6 well (BEU # 2 shown in dark gray) fall at the low end of the data set. These data, which were measured under 500 psi of overburden stress, may represent the best estimation of purely matrix permeability. (Factors that may complicate this interpretation are discussed later.) Whole-core data (from the BEU #3; shown in light gray) are generally higher. Note that these whole-core data are represented as the geometric average of two directional values. Further analysis of these directional data (Fig. 43) indicates that there is about a one-half order of magnitude variation in the measurements.
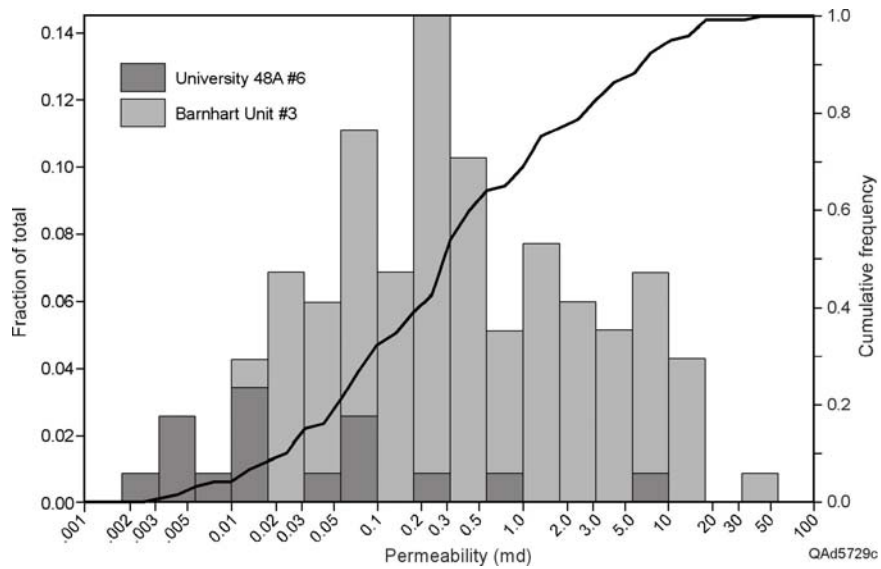
Figure 42. Plot of horizontal permeability data for the Goldrus Barnhart Unit # 3 core.
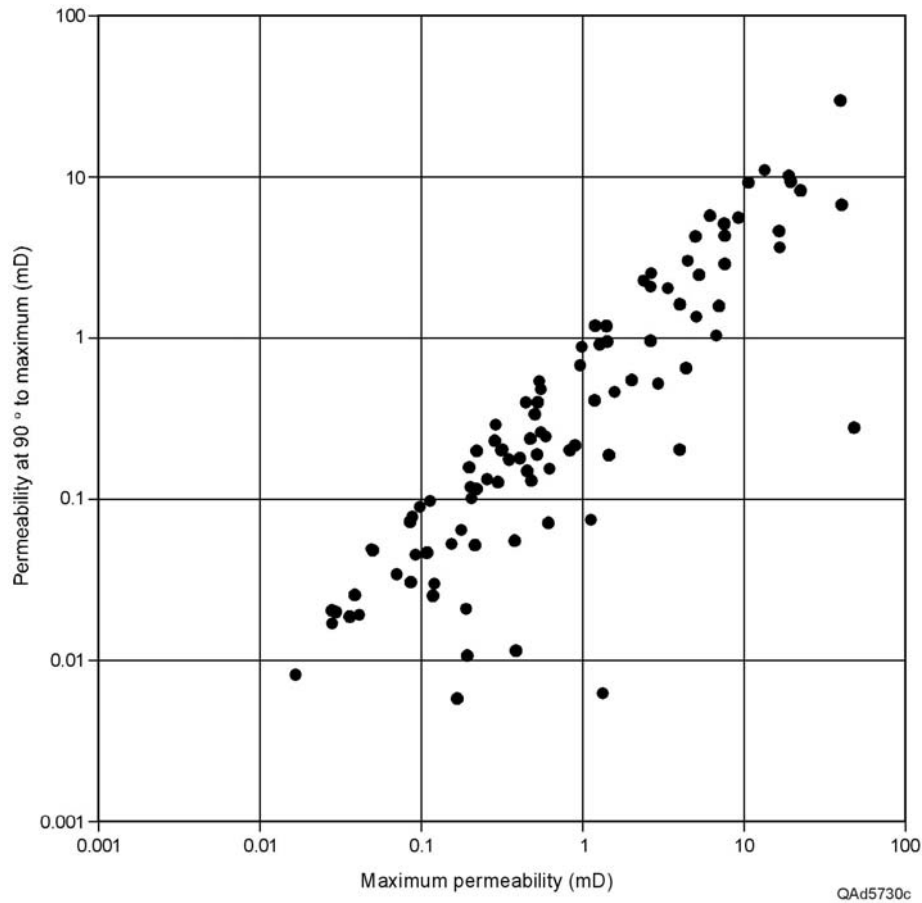
Figure 43. Crossplot of maximum and 90 degrees to maximum permeability data for the Goldrus Barnhart Unit # 3 core. Note that data suggest permeability anisotropy. No azimuth data are available to define orientations.

Comparison of porosity and permeability data (Fig. 44) reveals that the two core data sets define distinctly different trends for the same general porosity range. One of these data sets (University 48A #6 [BEU # 2] shown in black) is from plugs that were carefully selected to avoid fractures (and thus be representative of matrix properties) and measured under 500 psi stress The second set of data are from whole-core measurements made at ambient conditions (BEU #3 shown in gray). The higher permeabilities exhibited by the whole-core data suggest that there are nonmatrix components to these data, possibly fractures. It may be that these nonmatrix components are stress-relief features developed at ambient conditions and that are not present at overburden pressures. If so, as pressure on the formation decreases as a result of increased pore pressure at or near an

injection site, local permeability enhancement may occur, suggesting that increased

permeability will be induced by the HPAI procedure.
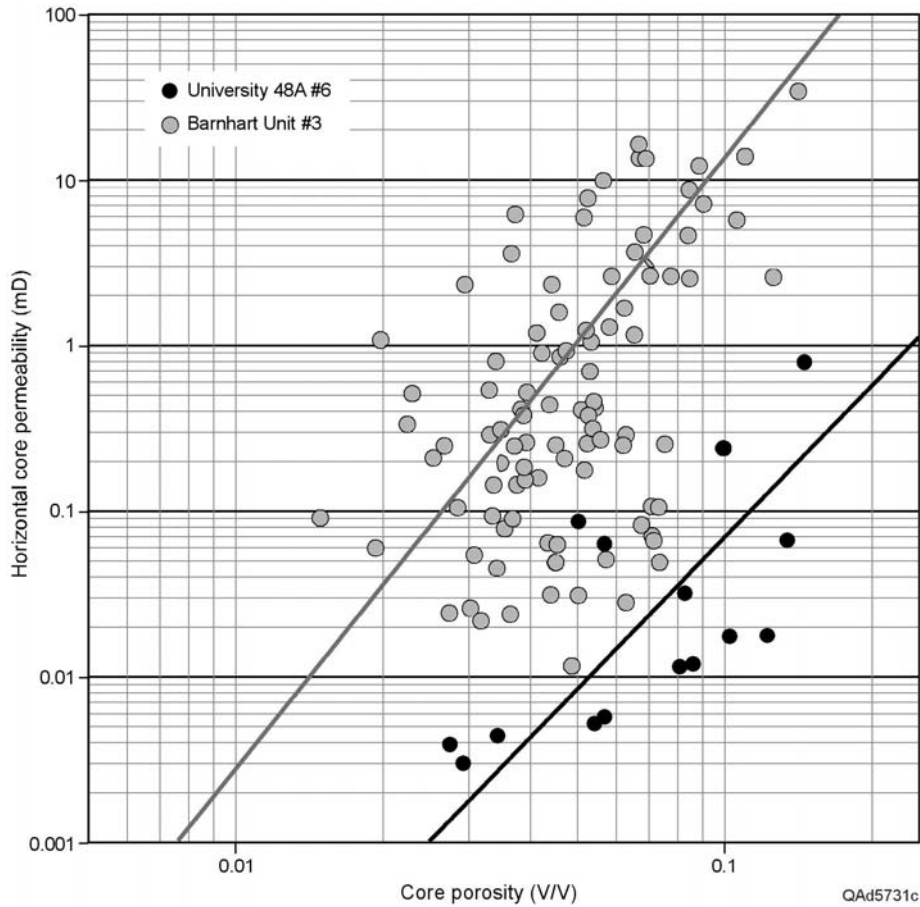
Figure 44. Crossplot of permeability and porosity data for Goldrus Barnhart Unit # 3 core. Gray circles = whole core data at ambient pressure. Black dots = core-plug data at 500 psi confining pressure. Plug data may be a better measurement of matrix permeability, whereas whole core data may reflect the additional influence of fractures.

The two core data sets thus suggest two different relationships between porosity and permeability. For "matrix"-dominated conditions, permeability is represented by

$$K_{matrix} = 10^{(1.881 + 3.037log(porosity))}$$

and for combined matrix and fracture conditions, permeability is represented by

$$K_{total} = 10^{(4.826 + 3.687log(porosity))}$$

where K_{matrix} is the permeability at the low end, K_{total} is the permeability at the high end, porosity is the measured porosity at depth, and *log()* is the base 10 logarithm.

It may be that observed differences in the two data sets reflect a stratigraphic or depth control on reservoir attributes. Figure 45 is a plot of permeability (from both core data sets) versus depth measured from the top of the Ellenburger. A 4-percent porosity cutoff is applied to emphasize data trends. Two things are apparent from this plot. First, permeability increases with depth, at least through approximately the top 200 ft of the Ellenburger. Second, the two core-analysis data sets sample stratigraphically and structurally different parts of the Ellenburger section.
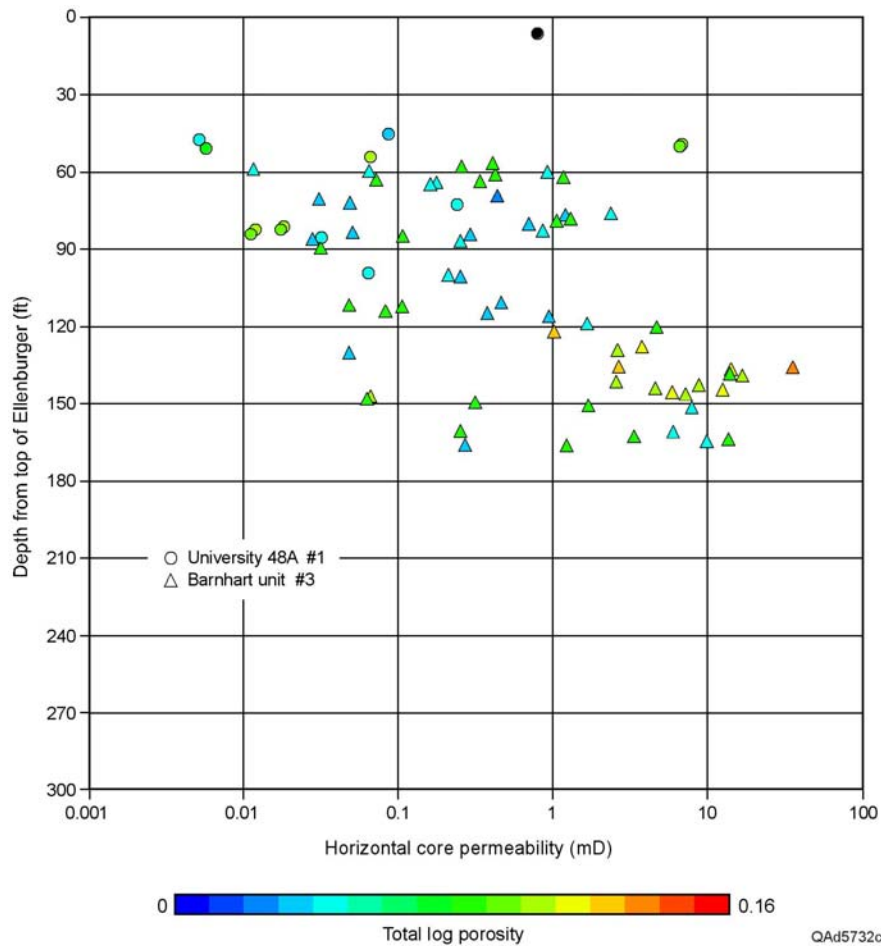
Figure 45. Plot of permeability and porosity data for two Goldrus Barnhart cores (Unit # 3 and 48A#1) against depth. Datum: top of Ellenburger. Porosity below 4 percent has been eliminated from plot to emphasize trend of increasing porosity and permeability with depth.

49

If permeability is a function of stratigraphy or depth it may be that a more appropriate way to apply the two porosity/ permeability relationships is to tie them to depth. So for depths less than 50 ft from the top of the Ellenburger, the first equation would apply:

$$K_{upper} = 10^{(1.881 + 3.037log(\text{porosity}))}$$

For the depths below 150 ft from the top of the Ellenburger, the second equation would apply:

$$K_{lower} = 10^{(4.826 + 3.687log(\text{porosity}))}$$

For depths between 50 and 150 ft below the top of the Ellenburger a simple weighted average of the two could be applied:

$$z = (\text{depth below top of Ellenburger} - 50) / (150 - 50)$$

$$K_{depth} = (1 - z)K_{upper} + zK_{lower}$$

where K_{depth} is the interpolated permeability and z is the weighting function. Results of such a relationship are presented in Figure 46.
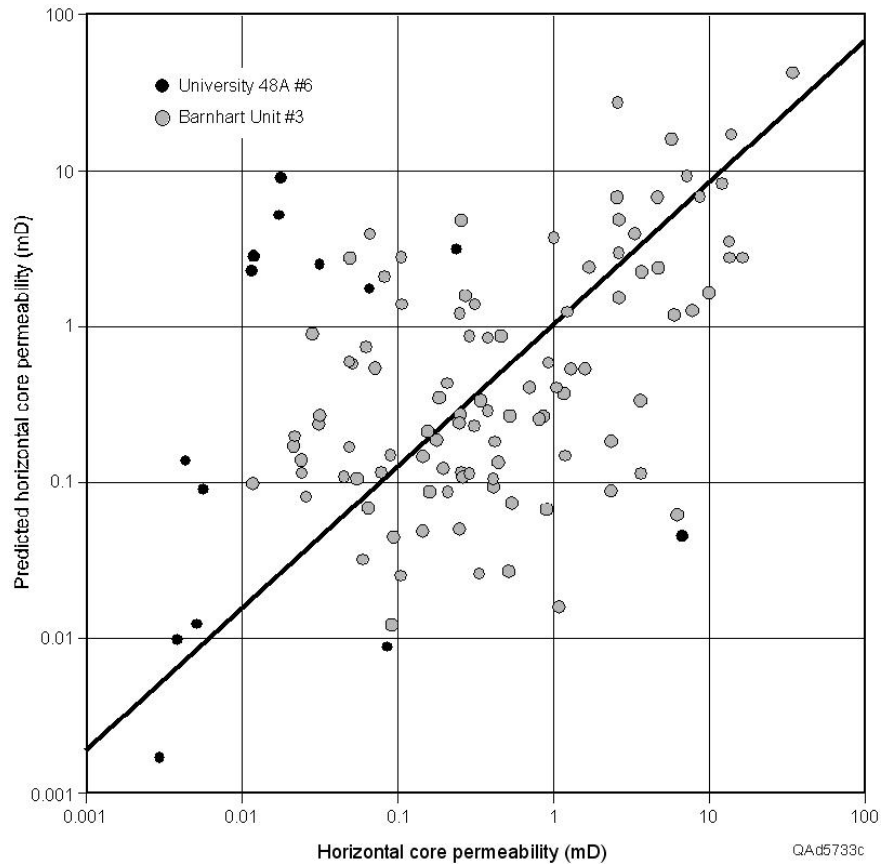
Figure 46. Crossplot of measured horizontal permeability and calculated horizontal permeability for Goldrus Barnhart Unit # 3 core.

Although it is not unreasonable to accept the possibility of such a depth-controlled relationship, the geological history of the field (specifically tectonic and karst events) makes it unlikely that such a model would be applicable over any significant area of the field.

Wireline-Log Data

The three wells considered here are the two cored wells—University 48A #6 (BEU# 2 and BEU #3) discussed previously—and the University 48A #1 (BEU # 1). These three wells have reasonably complete, modern log suites with at least a neutron-density-PEF combination and a resistivity device. The BEU #1 and #2 wells are reentries, and the BEU #3 well is a new drill. Data from these wells were edited and processed for porosity, lithology, and water saturation. Figure 47 is a crossplot of log-derived porosity

versus core porosity. In general, there is good agreement, although the log-porosity values are somewhat higher in the midporosity range. This information is not unexpected in a succession such as the Ellenburger, which is typified by relatively low matrix porosity and large vugs. Large vugs are not commonly sampled by core, so it is reasonable to expect core measurements to be lower than log measurements overall.
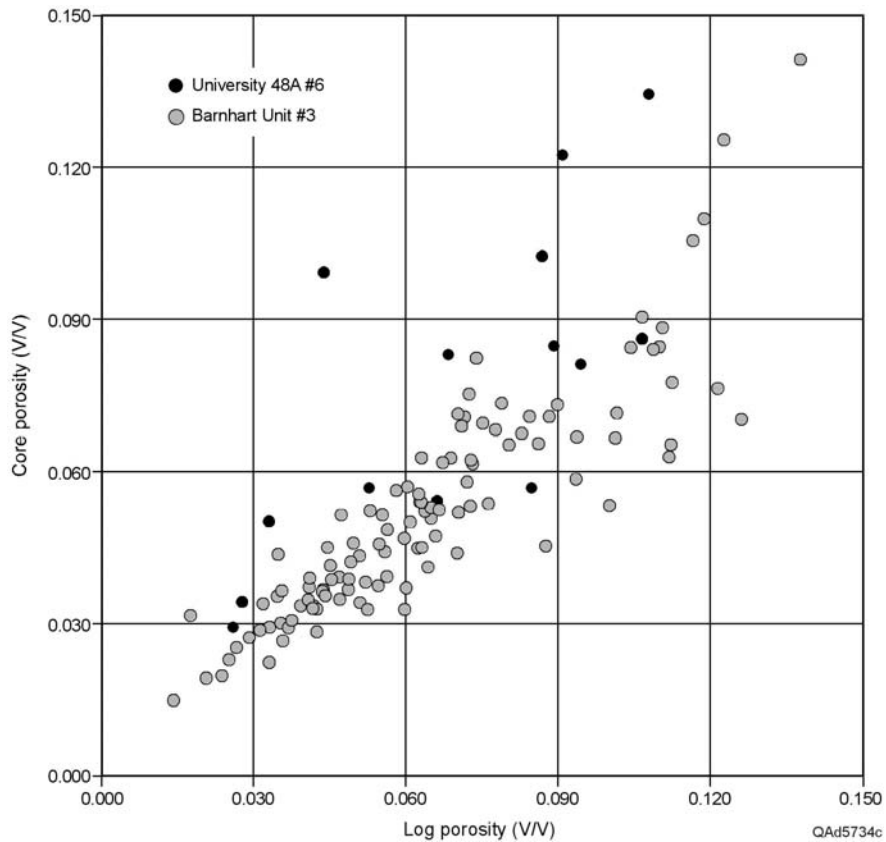
Figure 47. Crossplot of porosity against log-derived porosity for Goldrus Barnhart Unit # 3 core. The higher porosity values from logs are typical of formations that contain macroporosity features (such as fractures and vugs) because they are not well measured by core analysis.

The lithology analysis calculates the section to be essentially all dolomite, with minor amounts of limestone, and agrees well with the core data.

Water saturation was calculated using a standard Archie relationship, with cementation (m) and saturation exponents (n) of 2 and a formation-water resistivity (R_w) value representing formation conditions of 0.03 ohmm. Results of these computations are provided in graphical form for each well in Figures 48 through 50. In these plots, Track one, farthest to the left, contains the computed lithology, and Track 2, to the immediate

52

right of the depth track, contains the porosity analysis, scaled from 0 to 30 percent porosity. Hydrocarbon fraction is shown in green, and water fraction in blue. Core porosities, where available, are plotted in red. To the right of this track is the saturation profile. Moving farther to the right, permeabilities that were computed from the K_{matrix} (blue) and K_{total} (red) equations previously discussed are displayed. Core permeabilities are plotted in black where available. Track five, farthest to the right, contains some quality curves. The black curve is the density-correction curve, which is an indication of borehole roughness. The green curve is the caliper—again an indication of borehole quality. The red curve, quality, is an indication of how well the lithology-porosity model fits the recorded data. A value of zero is a perfect fit, and as the value increases, the quality of the fit decreases.
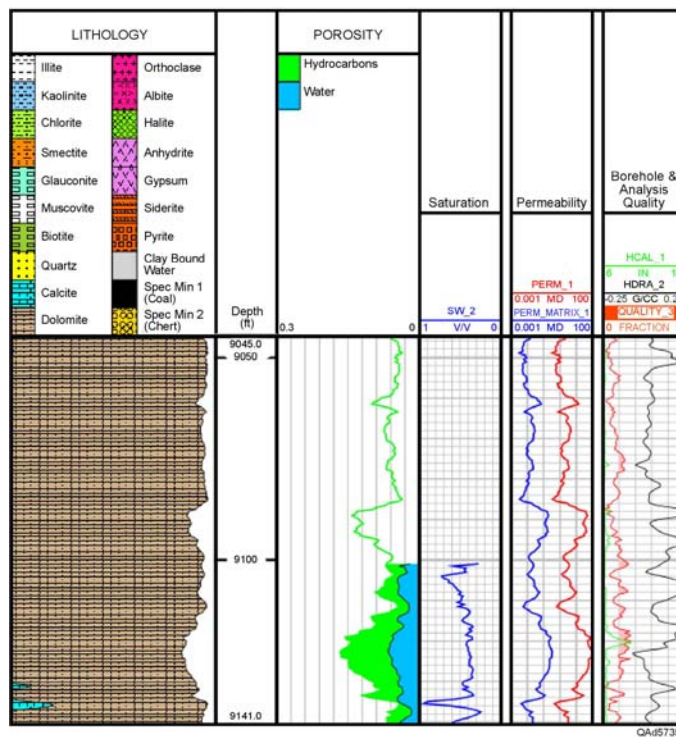
Figure 48. Log plot of the University 48 A #1 well.

53
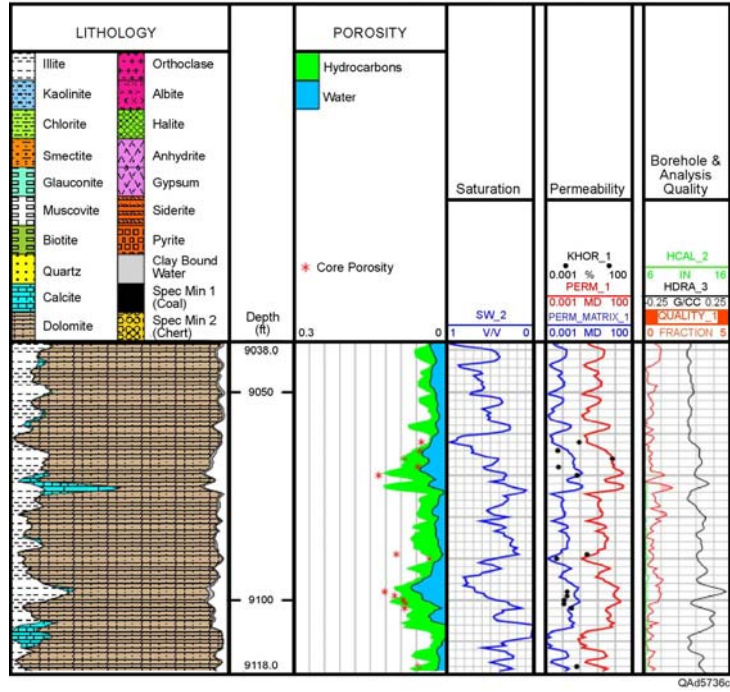
Figure 49. Log plot of the University 48 A #6 well.
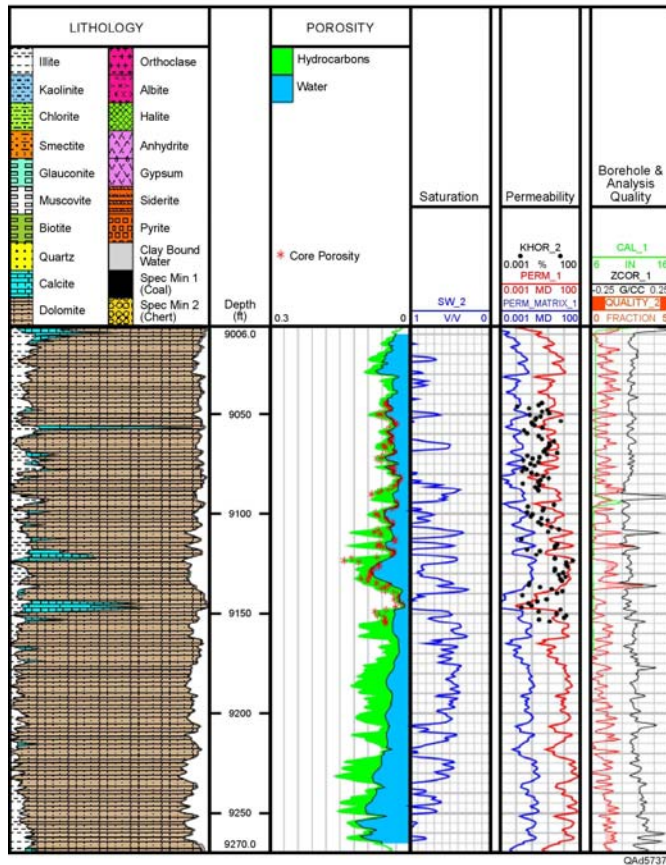
Figure 50. Log plot of the Goldrus Barnhart Unit # 3 well.

Figure 51 displays water-saturation data for all three wells as a function of depth from the top of the Ellenburger. Color represents porosity, the hotter colors being higher porosities. Some important relationships are apparent. First, an OWC is indicated in the BEU#3 well at about 260 to 280 ft below the top of the Ellenburger (~ −6,510 subsea). This figure contrasts markedly with the interpreted OWC of −6,385 subsea reported for the Hickman #13 well by Sipes and others (1973). When water-saturation data are plotted against elevation (Fig. 52), a distinct change in the character of the water-saturation profile occurs becomes apparent at about the position of the OWC reported for the Hickman well. Above that depth, water-saturation values are highly variable and show no relationship to depth. However, below this depth, values appear to decease systematically with depth (Fig. 52). This trend and the overall shape of the trend resemble those of capillary-pressure-controlled changes in saturation with depth.
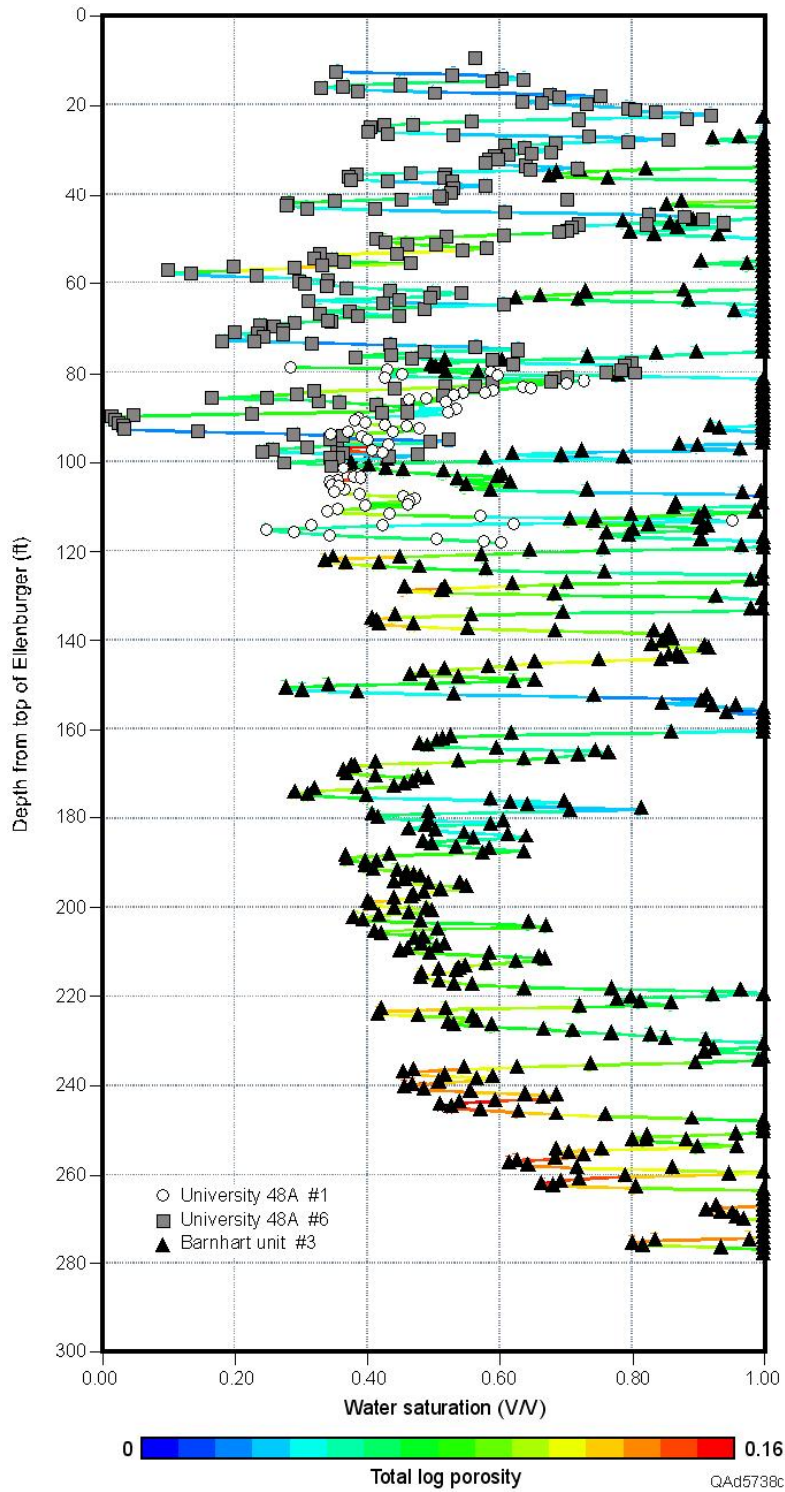
Figure 51. Plots of water saturation against depth for the three cored wells. These data suggest that the oil-water contact may be as much as 250 ft below the top of the Ellenburger.

56
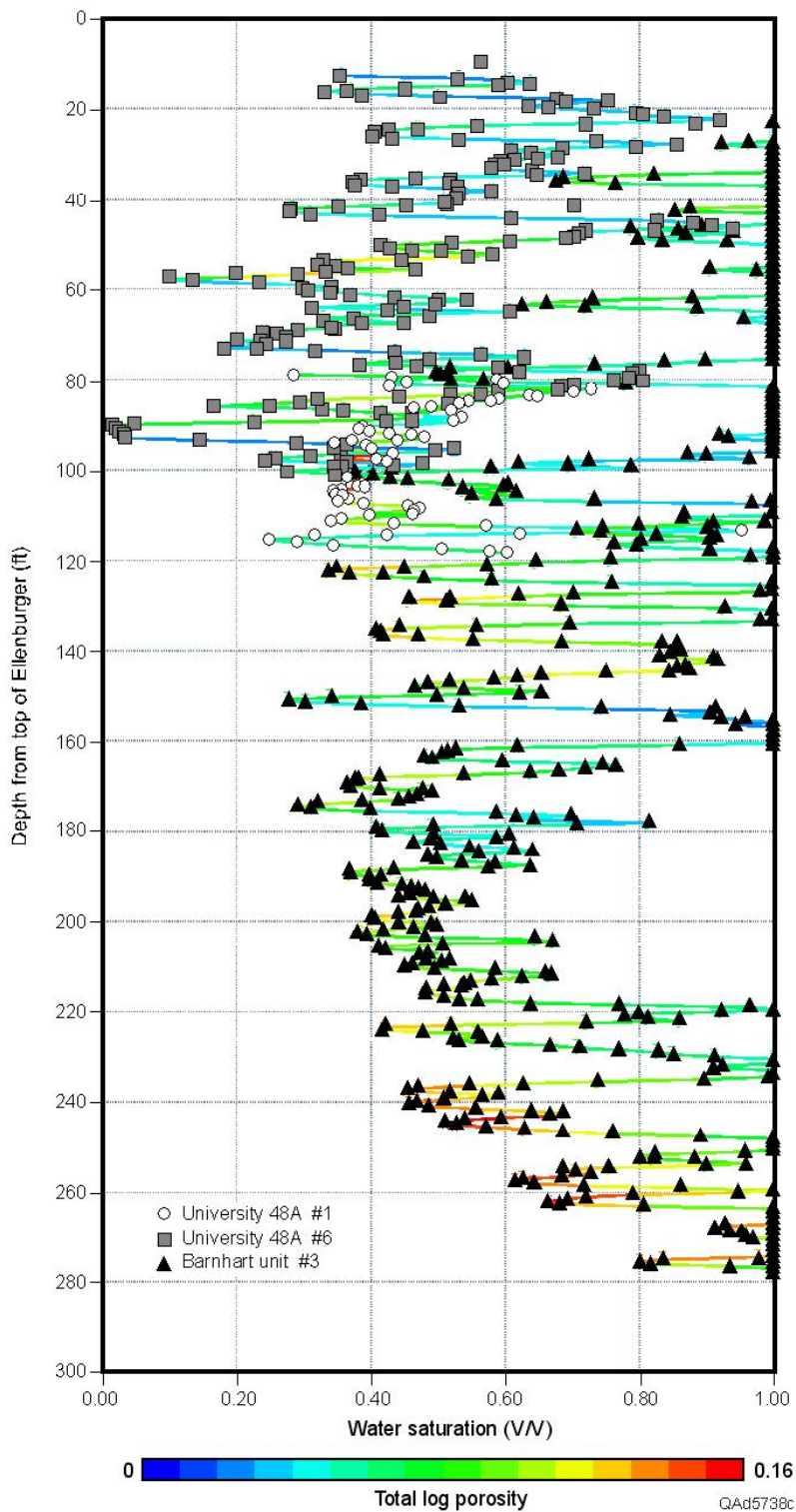
Figure 52. Plots of water saturation against elevation for the three cored wells. Compare the previously reported oil-water contact at −6,385 (Sipes and others, 1973) to the oil water contact suggested by water-saturation modeling at −6,510.

The indication from the Barnhart Unit wells that the true OWC is actually much lower than previously assumed has major implications for original-oil-in-place volume and for the oil resource remaining in the field. As an example, Table 1 presents a comparison of calculated hydrocarbon pore volumes in each of the wells for (1) the reservoir section down to –6,385 (the previously calculated OWC) and (2) down to –6,470 (a conservative estimate of the OWC based on the current study data). Note that for the BEU #3 well, this added reservoir column increases calculated hydrocarbon pore volume fourfold. Even an assumption of a much more conservative OWC at –6,428 results in a doubling of the hydrocarbon pore volume. In the BEU #2 well, addition of only 30 ft (to current log TD) to the reservoir column results in an increase in hydrocarbon pore volume for the well of more than 150 percent.

Table 1. Calculations of average porosity, water saturation, phi-h, and hydrocarbon pore volume.

Well	Interval	Thickness	Average porosity	Phi-h	Average water saturation	Hydrocarbon pore volume
BEU #2 (University 48A #1)	Above –6385	87	0.071	6.18	0.52	2.96
BEU #2 (University 48A #1)	Above –6415 (TD)	114	0.081	9.23	0.49	4.73
BEU #1 (University 48A #6)	Above –6385	88	0.056	4.93	0.47	2.61
Barnhart Unit #3	Above –6385	124	0.062	7.71	0.86	1.08
Barnhart Unit #3	Above –6428	166	0.063	10.51	0.80	2.14
Barnhart Unit #3	Above –6470	209	0.069	14.48	0.72	4.01

Petrophysical Summary

Several important conclusions can be drawn from the core and wireline-log data sets examined from Barnhart field. First, porosity and water-saturation values from the field are consistent with those of other Ellenburger fields in the Permian Basin (Galloway and others, 1983). Average porosities are somewhat low; however, deliverability and

overall storage capacity are decoupled from matrix porosity values by virtue of the fractured and vuggy nature of the reservoir and are probably much higher than would be expected from a measure of matrix porosity alone.

Second, given the wireline-log data, it is apparent that, overall, porosity increases with depth, as does permeability. Water saturation appears to be more variable; however, it, too, generally increases with depth.

Third, there is good evidence from the BEU #3 well that the field OWC is substantially deeper than previously assumed. This study indicates that it may be on the order of 125 ft lower, suggesting that previous estimates of OOIP may be far too low. Data from the three BEU wells suggests that actual pore volume may be twice what has been assumed. However, more high-quality wireline-log data are needed in other parts of the field to determine how widely applicable these findings are.

EXPERIMENTAL CHARACTERIZATION OF THERMAL ALTERATION

Overview

As part of this project, an engineering study of Barnhart field was undertaken by researchers in the Petroleum Engineering Department at The University of Texas at Austin (Dhiraj, 2004). As part of this study, a simulation model was developed on the basis of available laboratory and field data. The model was utilized to perform waterflood and air-injection simulation runs in stratified and fractured reservoir environments. Potential application of horizontal wells was also investigated. Results obtained after an extensive history-matching exercise using combustion tube data indicate that the Barnhart reservoir is a good candidate for HPAI.

The study also provided insight into implementation of an HPAI recovery program in the Barnhart reservoir. The model used to test this concept consisted of an injector-producer pair of one-quarter of a five-spot pattern about 930 ft apart. Three architectural models were employed: a homogeneous reservoir, a layered reservoir, and a naturally fractured reservoir. Two well arrangements were employed: vertical-injector producer and vertical-injector-horizontal producer. Two types of injection fluids were used: water and air. A total of seven fluid components and one solid component were

utilized in the combustion model. Oil and rock properties were obtained from laboratory tests and well logs. Relative-permeability data were obtained by matching available laboratory combustion tube data. Chemical reaction kinetics data were obtained from available accelerated rate calorimetry (ARC) tests and adjusted by matching laboratory combustion tube data.

In the homogeneous reservoir case, a small amount of water-gravity segregation was observed, whereas in the air-injection case, gas override was evident. However, gas override was not observed in the layered reservoir or fractured reservoir models perhaps because the reservoir model has high-permeability layers separated by low-permeability layers. Of all cases studied, good reservoir sweep for waterflood and air injection was observed in high-permeability zones. However, waterflood studies in the fractured reservoir having these high-permeability zones resulted in low oil recoveries (as low as 11 percent) owing to severe channeling in the fractures, rendering waterfloods ineffective. It should be pointed out, however, that air injection in the fractured-reservoir model resulted in stable-combustion-front propagation through the reservoir, yielding high ultimate oil recoveries (as high as 80 percent).

To further improve understanding of the air-injection process in the field, various sensitivity analyses, such as use of different vertical to horizontal permeability ratios, use of different types of well arrangements, injection of enriched-oxygen air, and cyclic water and air injection (wet combustion), are suggested. This simulation study showed that the Barnhart reservoir is a good candidate for HPAI. Application of horizontal-well technology can improve ultimate resource recovery from the reservoir. However, incorporating accurate reservoir characterization studies and detailed combustion kinetics into the simulation model will ultimately decide the applicability and profitability of the HPAI process on a large scale.

Study Details

Stimulation Results

Simulation studies were conducted with two types of injection fluids: water and air. The objective of these studies was to investigate numerically the potential of HPAI to

displace oil versus a typical waterflood program. Steam injection for depths of 9,000 ft is considered impractical. These simulations were performed for a variety of reservoir conditions such as homogeneous reservoir, reservoir with discrete fractures, and horizontal injector and producer. Flooding simulations were continued until the economic limit was reached, i.e. higher than 99 percent water cut or breakthrough at the producer. A summary of results for a homogeneous reservoir and a reservoir with discrete fractures with relevant plots is presented below. Work on horizontal injector and producer conditions continues.

Homogeneous Reservoir (Single Porosity/Permeability: Table 2 presents results for waterflood and airflood simulation runs carried out in a homogeneous reservoir. Waterflood studies were carried out from production startup (after primary recovery) to the waterflood economic limit. An injection rate of 200 bbl/day was specified for the vertical injector, along with a pressure constraint of 5,000 psi. The simulation was run for 8,000 days. Water breakthrough was achieved at the producer at about 6,800 days, with the water cut increasing to 99 percent at around 8,000 days. Cumulative oil recovered at the end of the simulation was 210 Mbbl. Figure 53 is a plot with all the relevant waterflood parameters obtained during the simulation. Figure 54 is an oil-saturation snapshot of the reservoir at 4,000 days.

Table 2. Airflood versus waterflood for the homogeneous reservoir.

Prediction run	Production period (days)	Cumulative production			Oil recovery	Produced oil to injected volume
		Oil (Mbbl)	Gas (CH$_4$) (MMSCF)	Water (Mbbl)		
Waterflood	8000	209	0	1.85	0.718	0.836 bbl/bbl
Airflood	1200	183	2	0	0.63	690 bbl/MMSCF
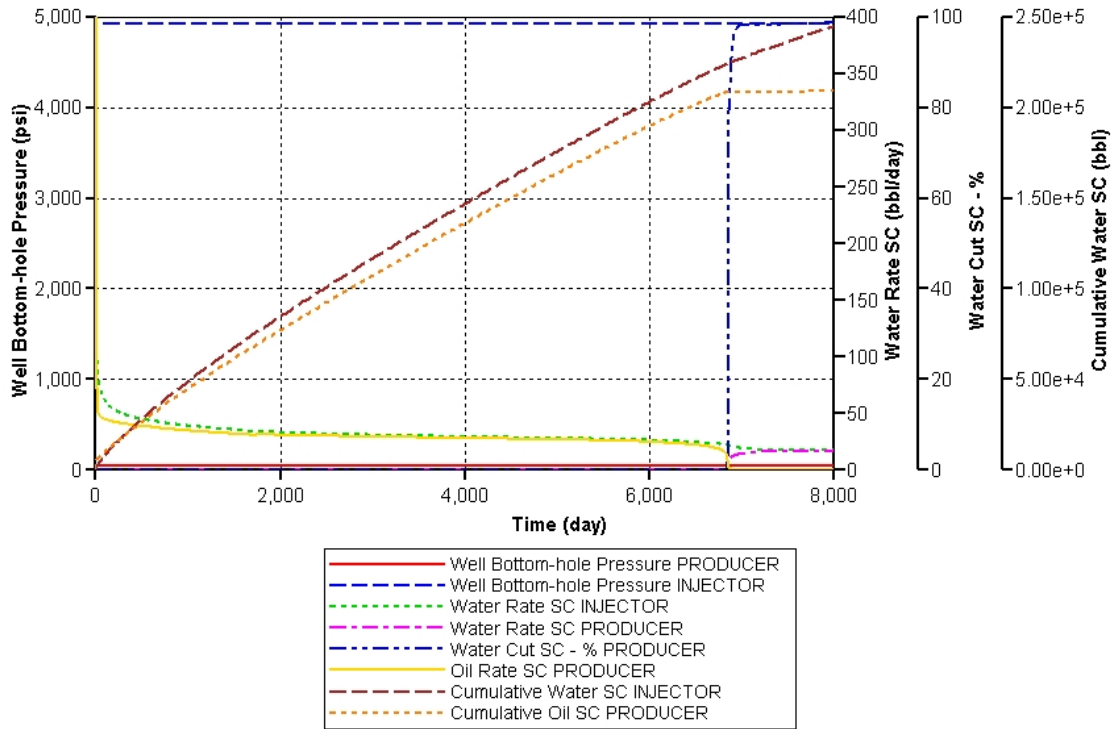
Figure 53. Pressure and fluid history during waterflood simulation.
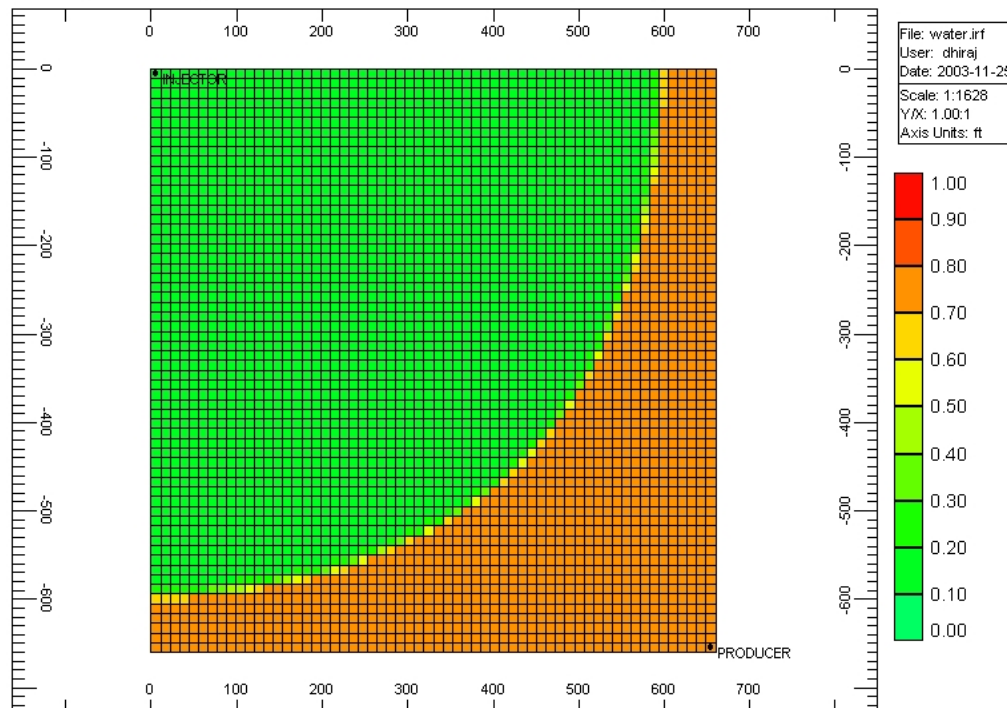
Figure 54. Oil saturation at 4000 days (fraction).

Airflood studies were carried out from production startup (after primary recovery) until much after gas breakthrough at the producer. An injection rate of 750 MSCF was specified for the injector, along with pressure constraint of 5,000 psi to reduce numerical stability. The simulation was run for 1,200 days. Gas breakthrough was achieved at the producer in the early stages of combustion. Although cumulative oil production plateaus after 400 days to a final value of 183 Mbbl at 1,200 days, the gas production rate continues to increase with time. Cumulative methane gas production at 1,200 days stands at 2 MMSCF. Figures 55 and 56 are plots of various airflood parameters recorded during the combustion run. Temperature profiles for a few grid blocks around the injector well are depicted in Figure 56. Figures 57 through 59 show temperature maps for the reservoir at 100, 400, and 1,200 days, respectively. Figures 60 and 61 show oil-saturation maps for the reservoir at 50 and 400 days, respectively. Figures 62 and 63 show pressure maps for the reservoir at 100 and 1,200 days, respectively.
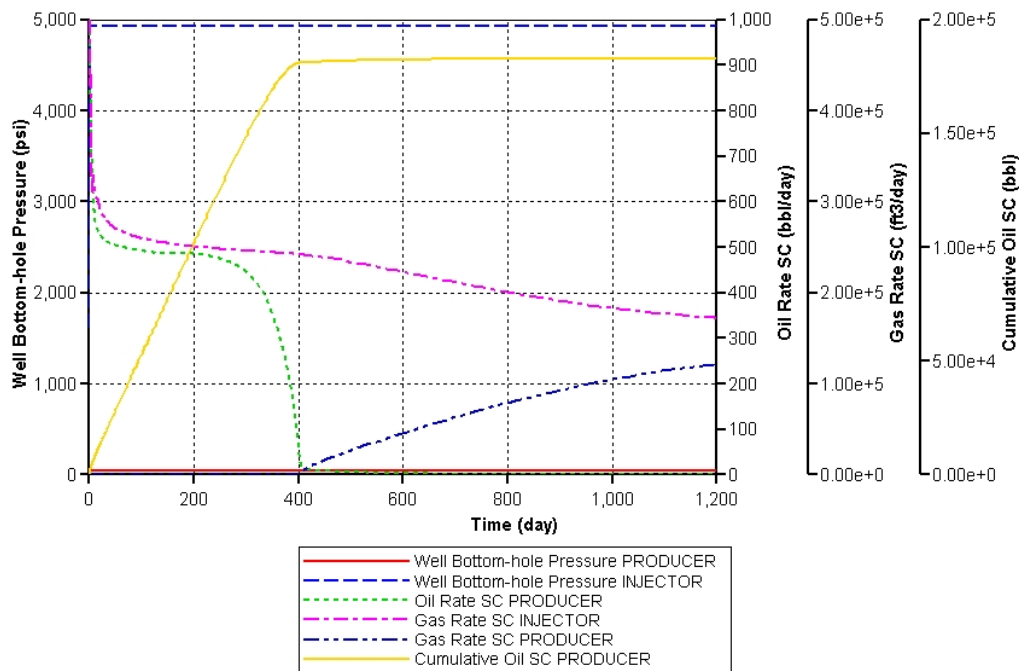
Figure 55. Pressure change and oil production response during air-flood simulation.
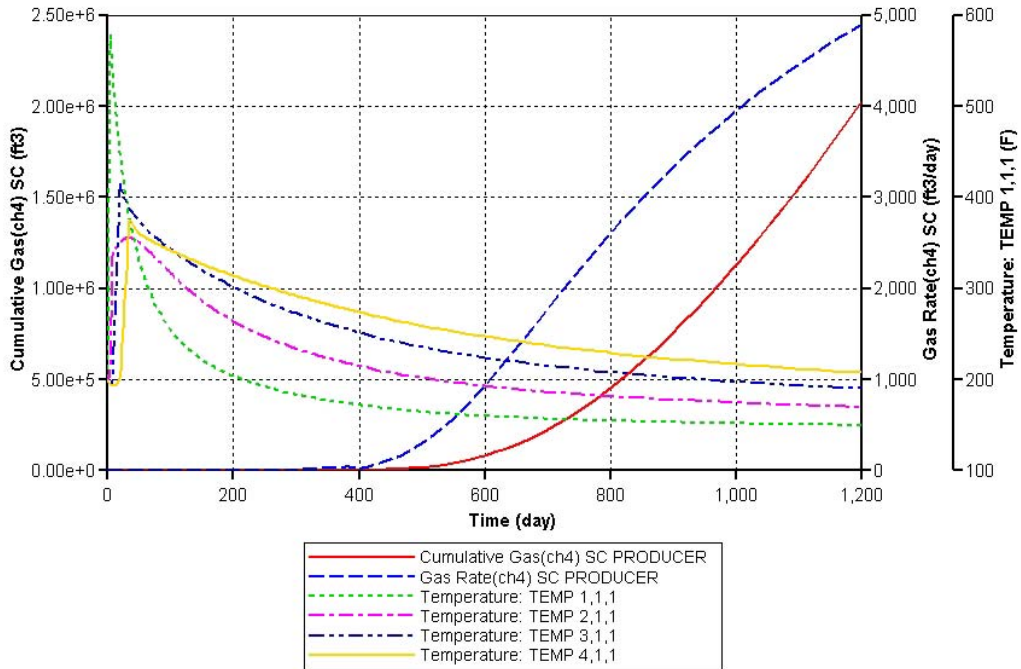
Figure 56. Gas production response and temperature change during air-flood simulation.
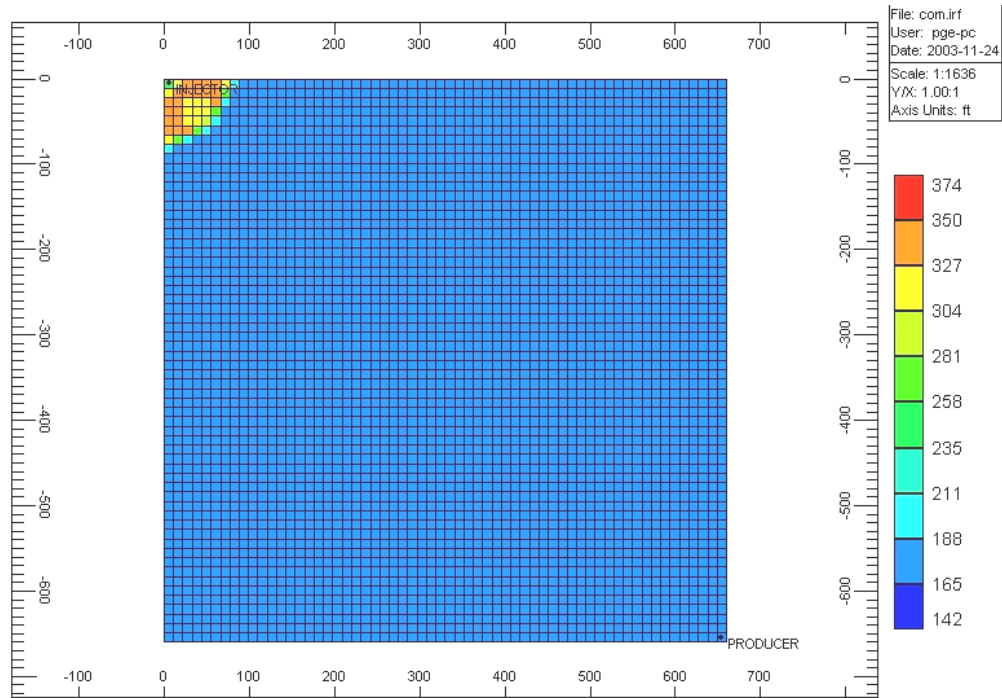
Figure 57. Temperature distribution after 100 days (°F) of air-flood simulation.
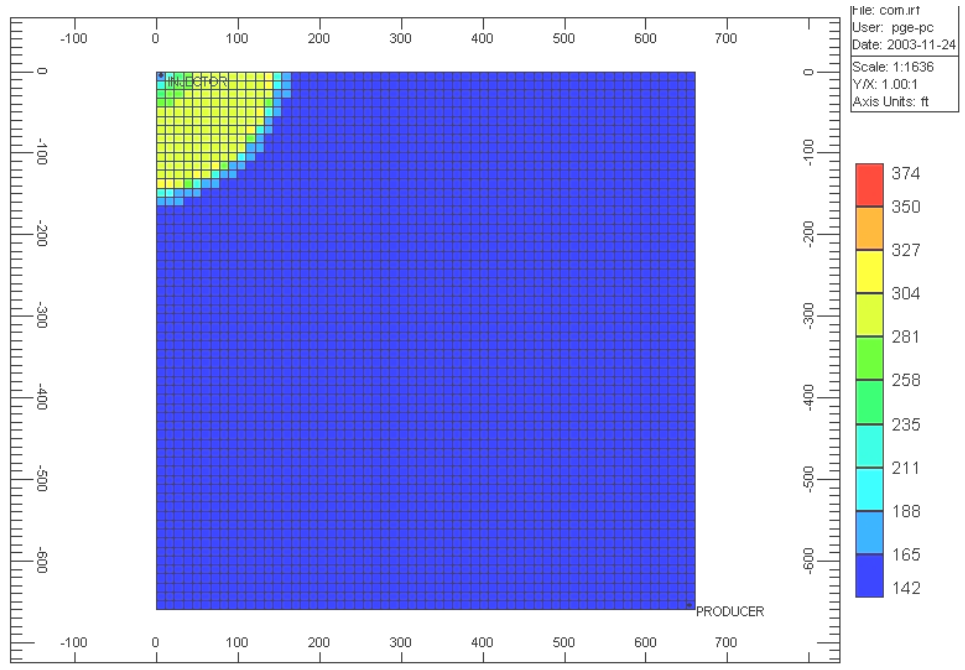
Figure 58. Temperature distribution after 400 days (°F) of air-flood simulation.
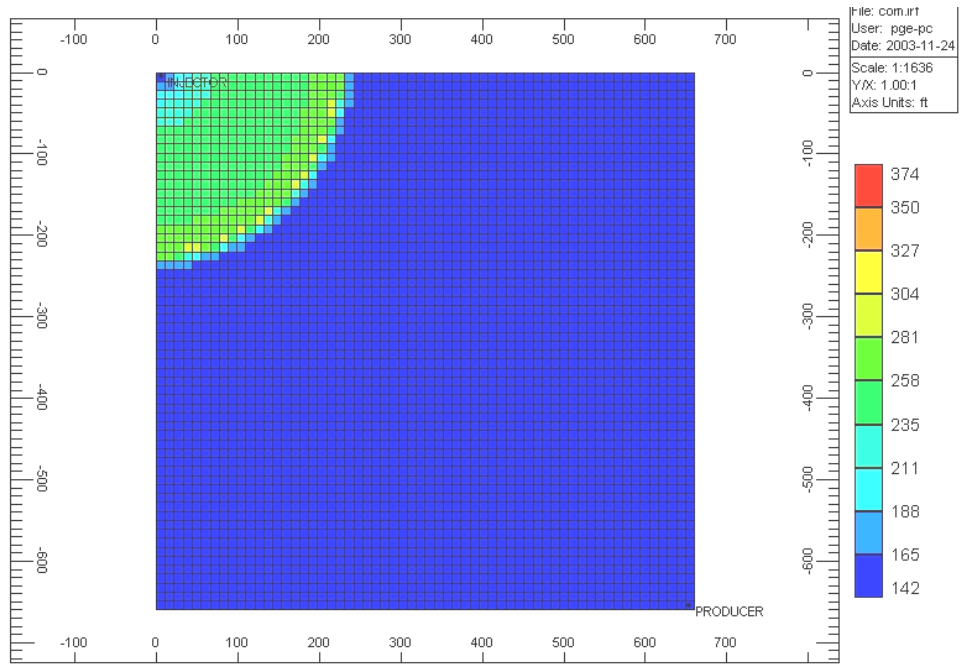
Figure 59. Temperature distribution after 1,200 days (°F) of air-flood simulation.
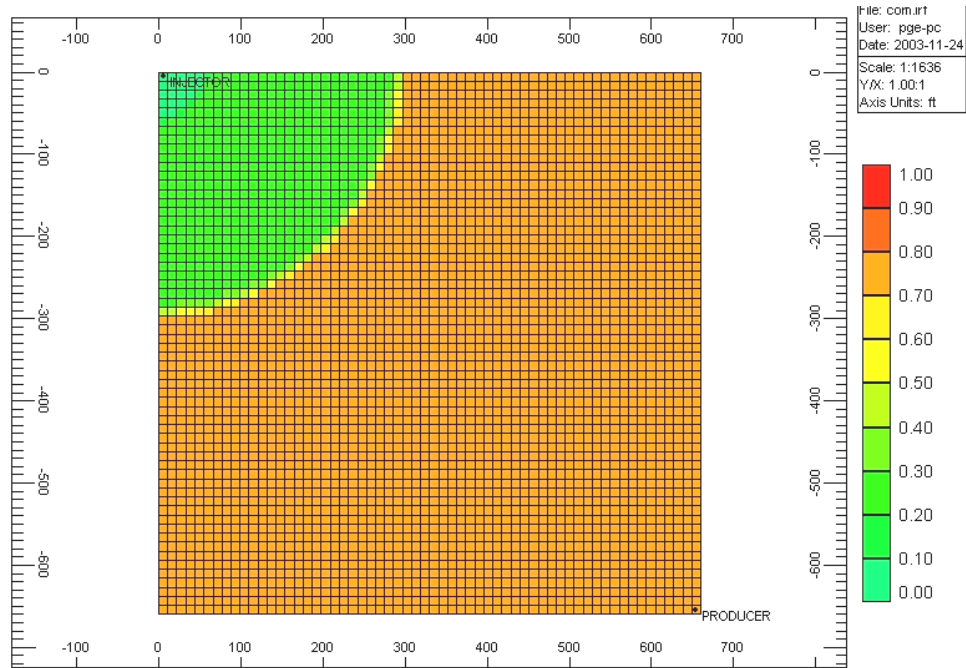
Figure 60. Distribution of oil saturations after 50 days of air-flood simulation (fraction).
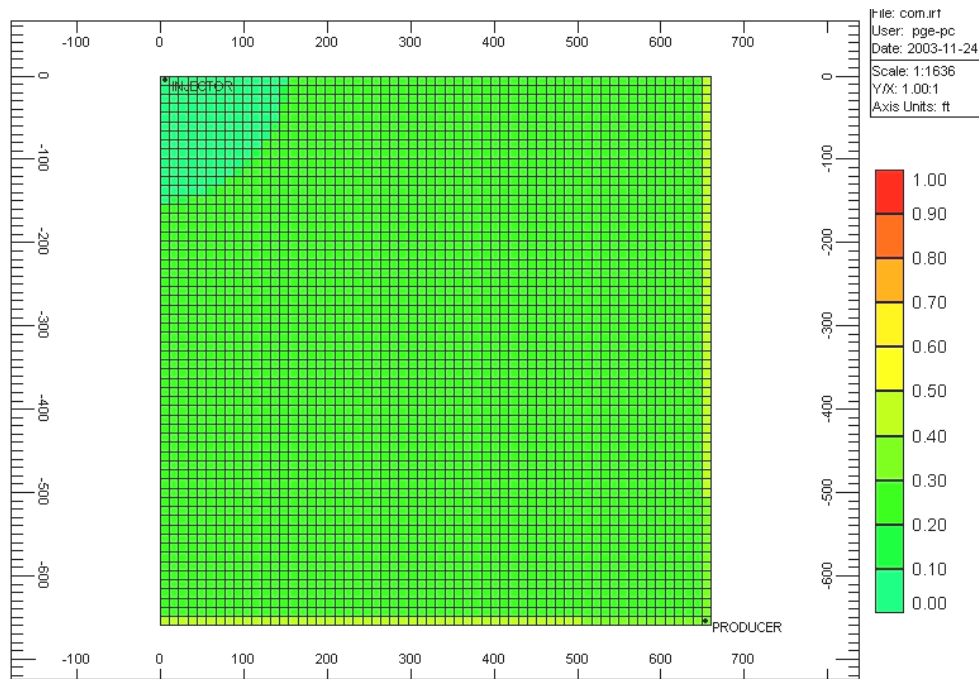
Figure 61. Distribution of oil saturations after 400 days (breakthrough) of air-flood simulation (fraction).
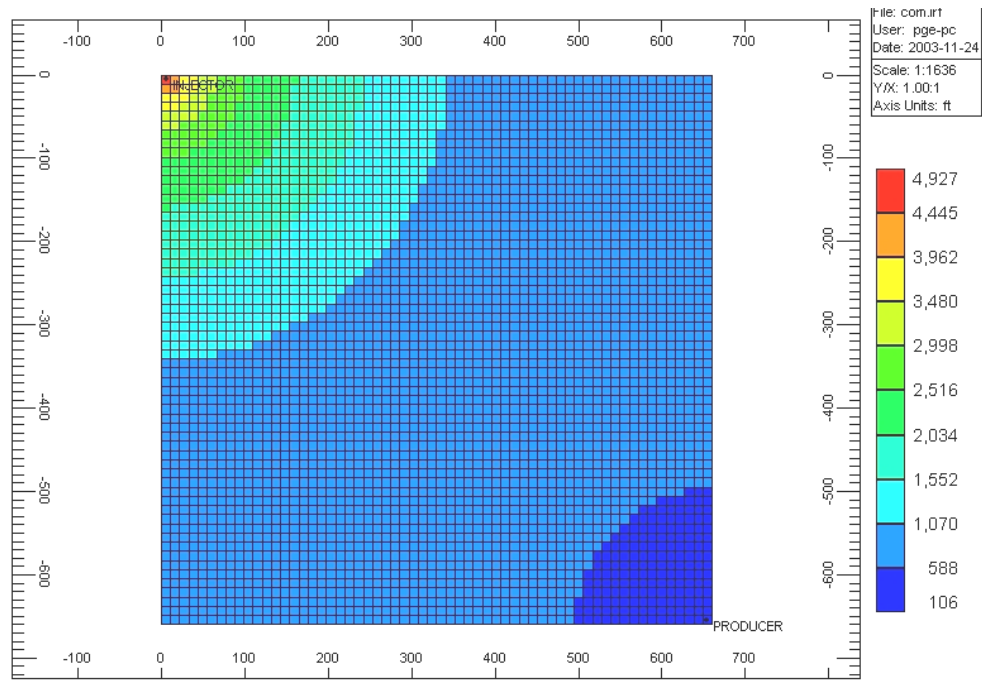
Figure 62. Pressure distribution after 100 days of air-flood simulation (psi).
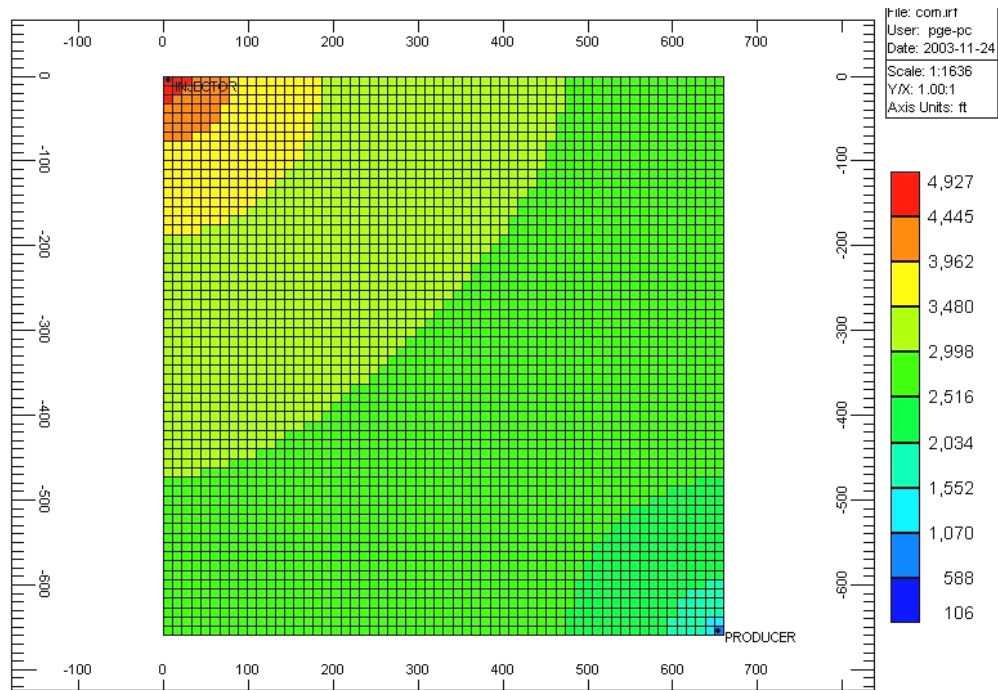
Figure 63. Pressure distribution after 1,200 days of air-flood simulation (psi).

Discrete Fracture System: To investigate the response of the two flooding techniques for a fractured system, we took the homogeneous reservoir discussed above and placed random, discrete, fracture streaks (Figure 64. Porosity and permeability values for these fractures were assumed to be 0.01 and 10,000 md, respectively. Relative permeability data for the fracture system was also accordingly modified.
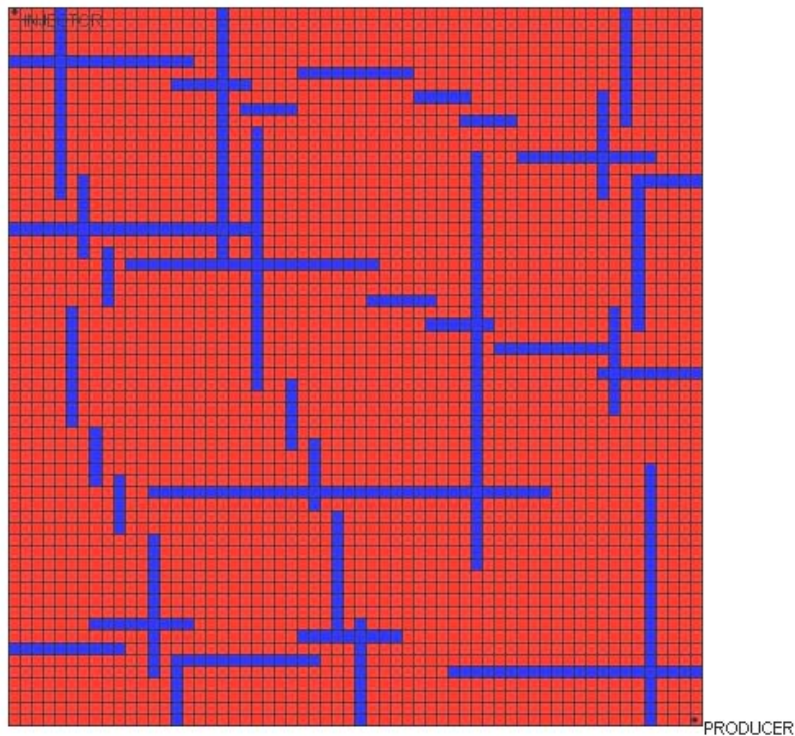
Figure 64. Fracture distribution used to simulate water and air injection in a fractured reservoir.

Table 3 summarizes waterflood and airflood results obtained from the simulation runs. Operating conditions here were the same as for those of the homogeneous reservoir discussed previously. The simulation was run for 6,000 days. Water breakthrough was achieved at the producer at about 1,600 days, much earlier than the breakthrough in the homogeneous waterflood case. Water cut of 99 percent was registered at around 6,000 days. Cumulative oil recovered at the end of the simulation was 183 Mbbl: a little lower than that in the homogeneous reservoir case. Final oil recovery also showed a minor decrease. Figure 65 is a plot showing all relevant waterflood parameters obtained

during the simulation. Figures 66 through 68 show oil-saturation maps for the reservoir at 100, 1,600 and 6,000 days, respectively.

Table 3. Airflood versus waterflood for the discretely fractured reservoir.

Prediction run	Production period (days)	Cumulative production			Oil recovery	Produced oil to injected volume
		Oil (Mbbl)	Gas (CH$_4$) (MMSCF)	Water (Mbbl)		
Waterflood	6000	183	0	214	0.696	0.416 bbl/bbl
Airflood	2000	169.5	25.35	1	0.65	188 bbl/MMSCF
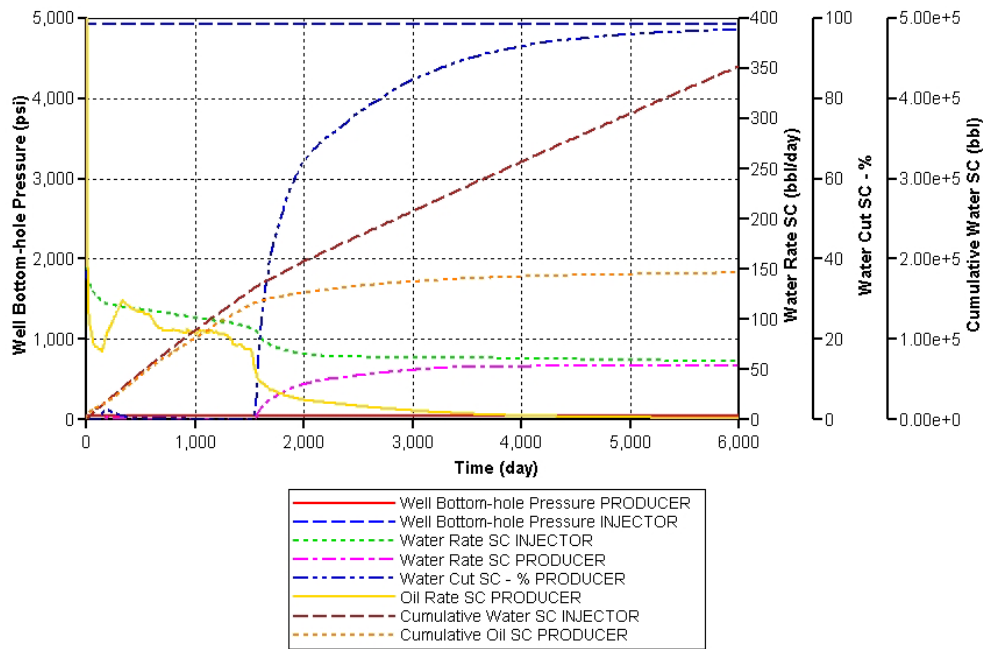
Figure 65. Waterflood response in fractured reservoir model simulation.
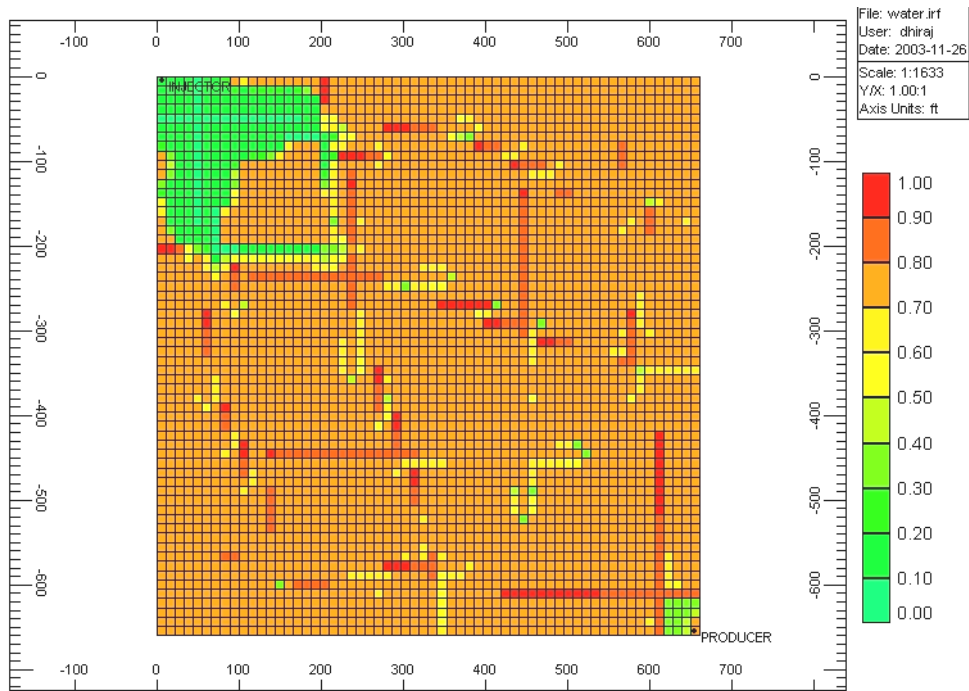
Figure 66. Distribution of oil saturations after 100 days of waterflood simulation of fracture model (fraction).
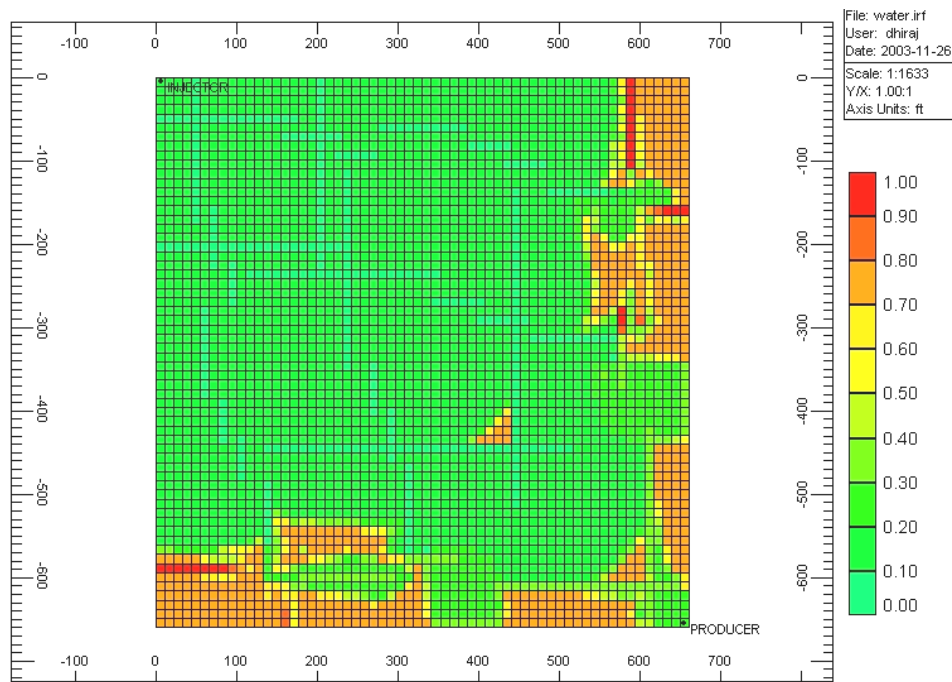
Figure 67. Distribution of oil saturations after 1,600 days (breakthrough) of waterflood simulation of fracture model (fraction).
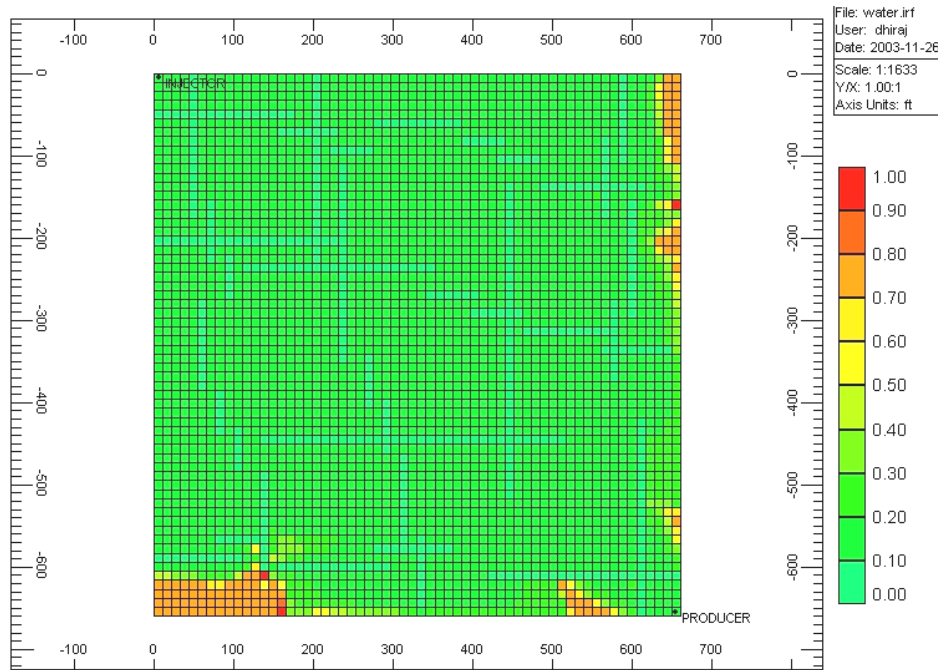
Figure 68. Distribution of oil saturations after 6,000 days of waterflood simulation of fracture model (fraction).

Operating conditions in these experiments were the same as those for the homogeneous airflood case. The airflood was run for 2,000 days, and gas breakthrough was achieved very early at the producer at around 130 days. Cumulative oil production after 2,000 days stood at about 170 Mbbl, nominally less than that of the homogeneous airflood case. The gas-production rate continued to increase with time, and cumulative production at 2,000 days was recorded to be 25.35 MMSCF, significantly higher than that of the homogeneous case. Figures 69 and 70 are plots of various airflood parameters recorded during the combustion run. Temperature profiles for a few grid blocks around the injector well are depicted in Figure 70. Figures 71 through 73 show temperature maps for the reservoir at 100, 1,000, and 2,000 days, respectively. Figures 74 and 75 show oil-saturation maps for the reservoir at 100 and 2,000 days, respectively. Figure 76 shows the pressure map for the reservoir at 2,000 days.
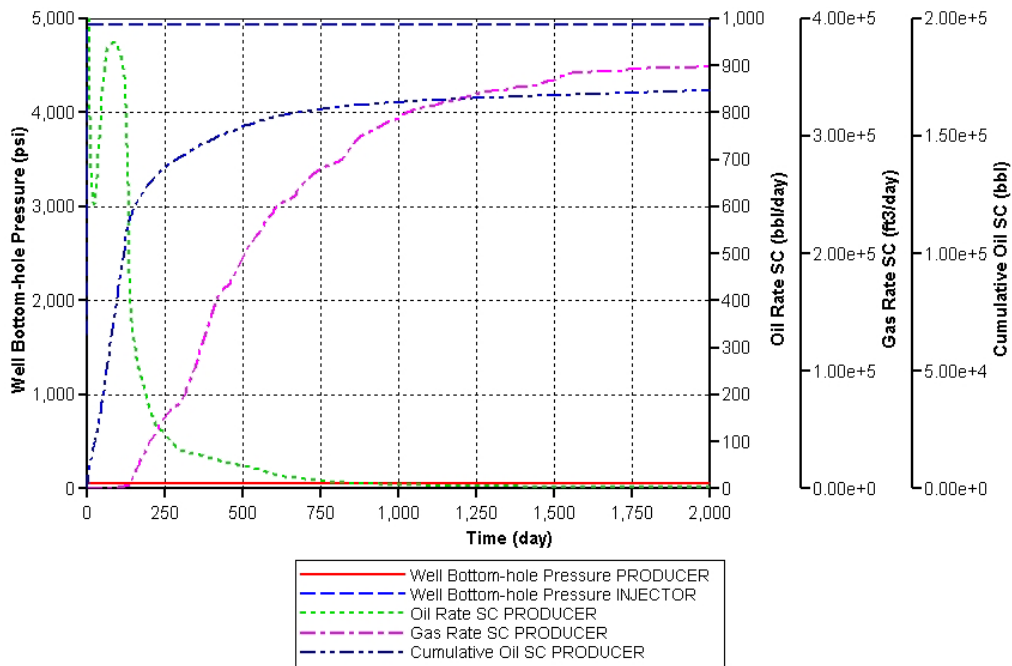
Figure 69. Production response from waterflood simulation of fracture model.
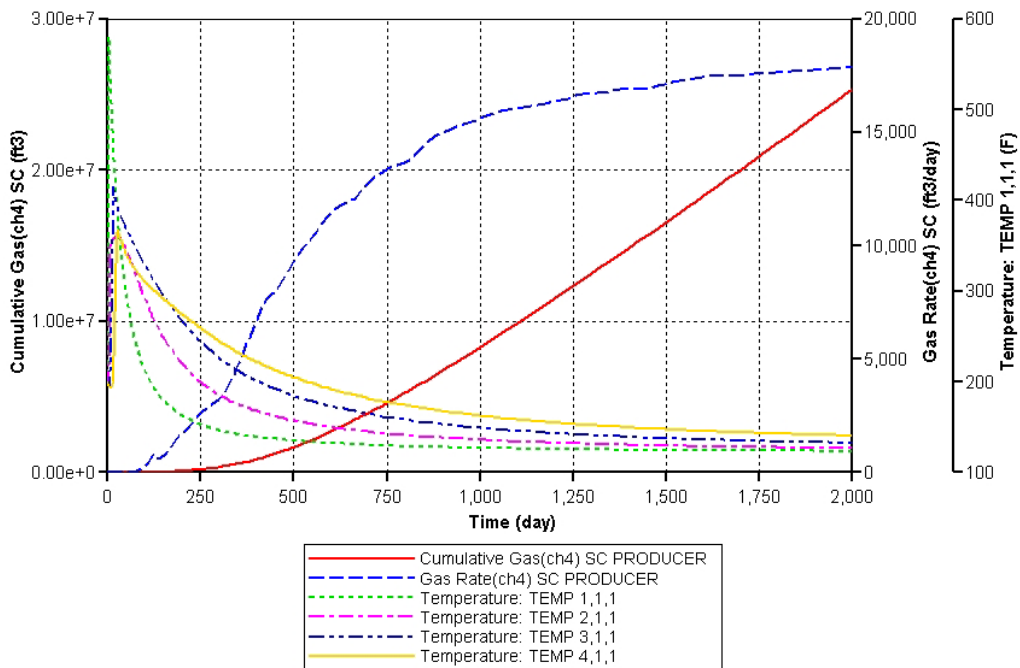
Figure 70. Gas-production response and temperature change during waterflood simulation of fracture model.

72
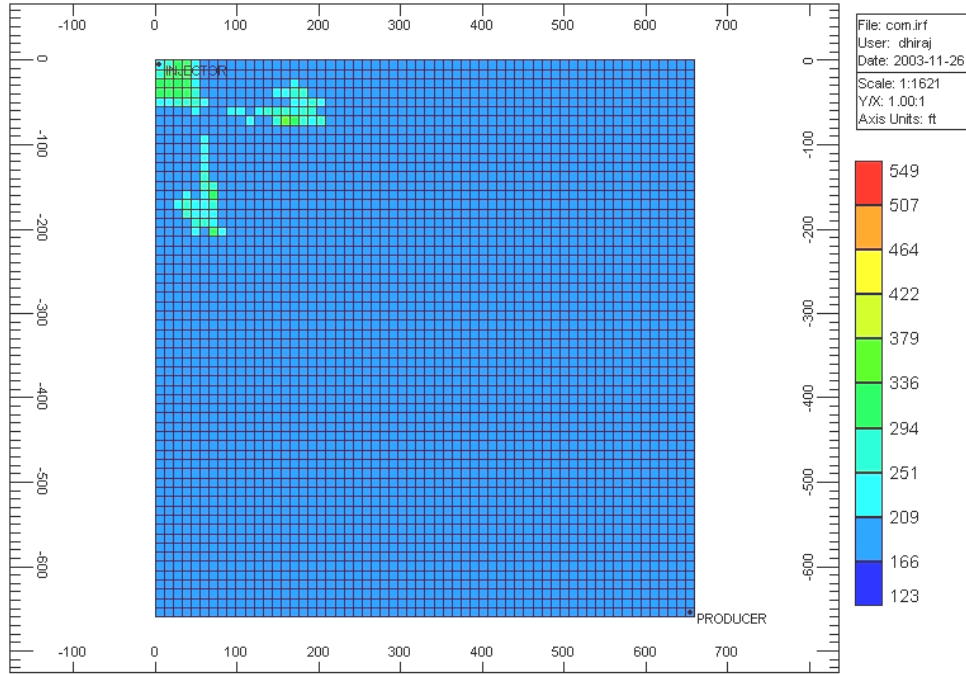
Figure 71. Temperature distribution after 100 days of waterflood simulation of fracture model (°F).
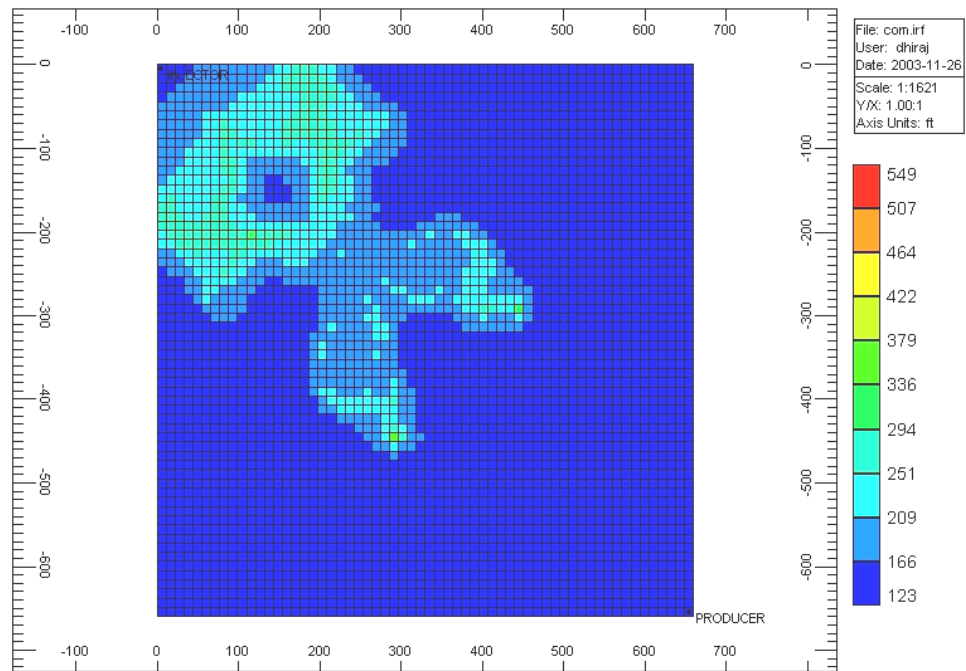
Figure 72. Temperature distribution after 1,000 days of waterflood simulation of fracture model (°F).
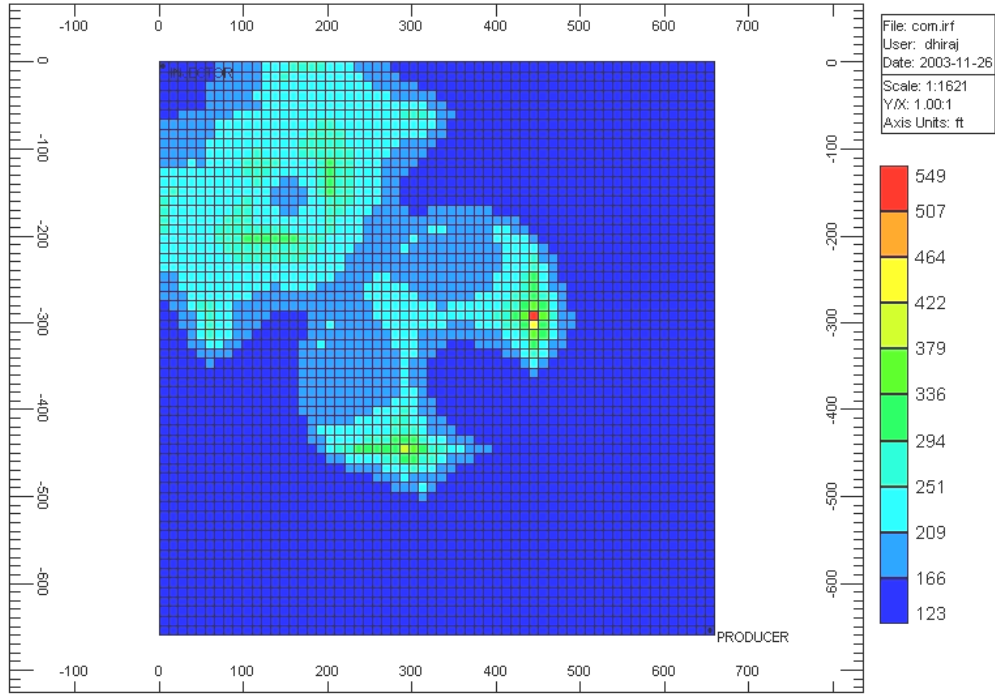
Figure 73. Temperature distribution after 2,000 days of waterflood simulation of fracture model (°F).
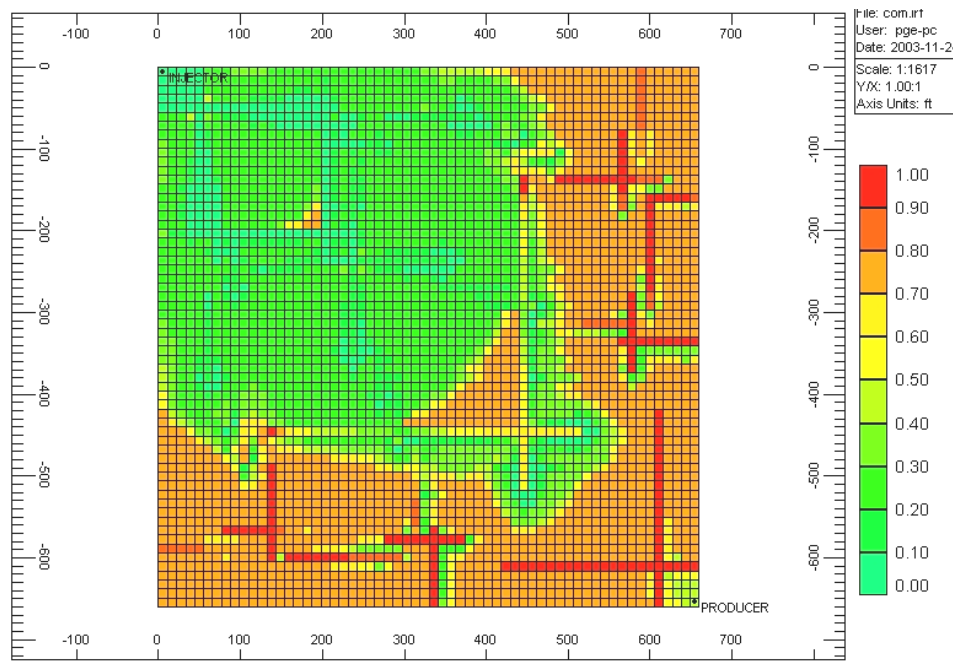
Figure 74. Distribution of oil saturations after 100 days (just before breakthrough) of waterflood simulation of fracture model (fraction).
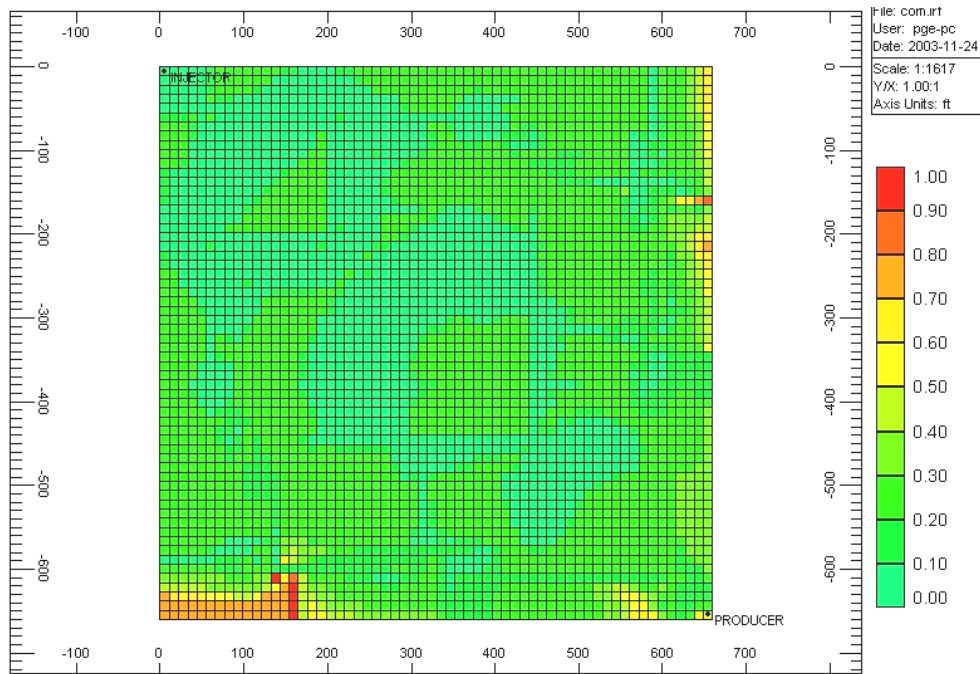
Figure 75. Distribution of oil saturations after 2,000 days of waterflood simulation of fracture model (fraction).
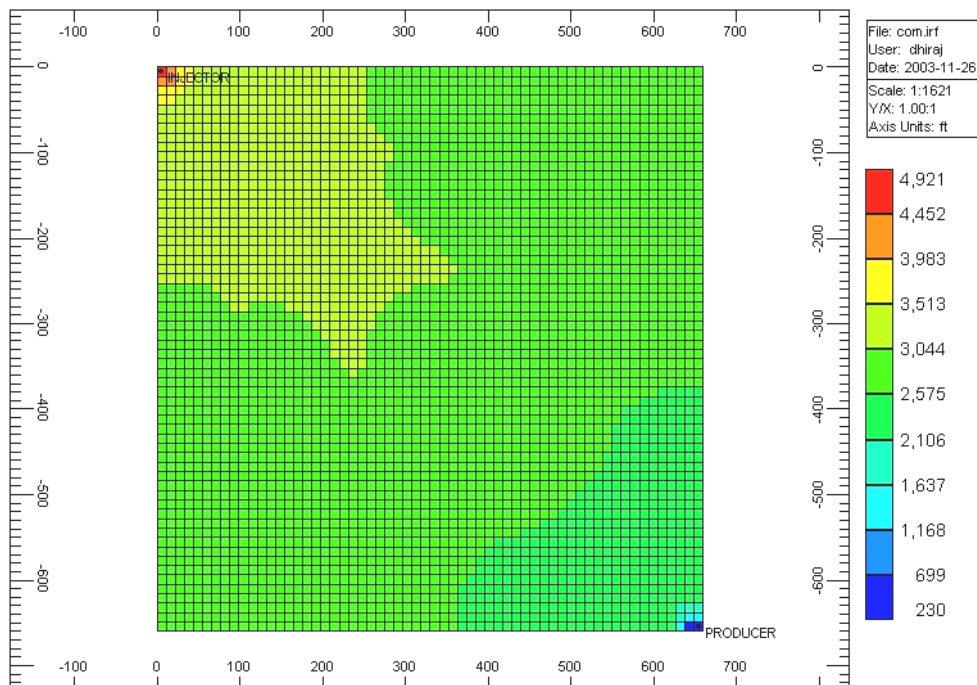
Figure 76. Distribution of reservoir pressures after 2,000 days of waterflood simulation of fracture model (psi).

SUMMARY AND CONCLUSIONS

Several important conclusions can be reached from available core and wireline-log and engineering data for the Ellenburger reservoir at Barnhart field. First, like most Ellenburger reservoirs in the Permian Basin, the reservoir section at Barnhart is dominated by peritidal dolomudstones that were deposited in a very restricted, inner-platform setting. Like most carbonate mudstones, these rocks exhibit low to moderate matrix porosity and permeability. Second, like most Ellenburger reservoirs in the region, the section at Barnhart displays a strong overprint of karst-related diagenesis, including a wide variety of cave-fill deposits, fractures, and correlation discontinuities. At the same time, this karst overprint adds to the heterogeneity of the reservoir and contributes additional porosity and permeability to basic matrix properties of the succession.

Correlations using resistivity logs have been locally successful in establishing reservoir architecture in many parts of the field, including, especially, the area of the Goldrus pilot injection program. An exception is the area of the BEU #3 well, which is shown from core to be highly affected by karst-cave formation, infill, and collapse processes. Correlation discontinuities elsewhere in the field may similarly reflect the presence of karsting.

Analysis of available core data clearly documents the dual porosity and permeability system that has been created in the Ellenburger by the interplay of depositional processes (matrix pore systems) and karst processes (fracture- and paleocave-related pore systems) and defines some very important trends in porosity and permeability. Specifically, this study shows that porosity and permeability are lowest in matrix-dominated intervals in the upper part of the reservoir section and higher in the lower, karst-overprinted part of the section.

Analysis of wireline-log data from the three modern well log suites in the field performed in this study strongly suggests that the true OWC in the field may be as much as 125 ft lower than previously reported. This finding has a potentially huge impact on calculations of the OOIP and estimations of recoverable hydrocarbon volume.

The simulation study showed that the Barnhart reservoir is a good candidate for HPAI. Application of horizontal-well technology can improve ultimate resource recovery

from the reservoir. However, incorporating accurate reservoir characterization studies and detailed combustion kinetics into the simulation model will ultimately decide the applicability and profitability of the HPAI process on a large scale.

Finally, a review of the production history of the field strongly indicates that despite any heterogeneities that may exist, the reservoir has behaved like most matrix-dominated, solution-gas-drive reservoirs in the Permian Basin. This behavior suggests that the reservoir should respond in a similarly favorable way to advanced oil recovery technologies such as HPAI.

REFERENCES

Britt, T. L., 1988, Joy of searching for eroded Ellenburger traps (abs.): American Association of Petroleum Geologists Bulletin, v. 72, p. 99.

Combs, D. M., Loucks, R. G., and Ruppel, S. C., 2003, Lower Ordovician Ellenburger Group collapsed Paleocave facies and associated pore network in the Barnhart field, Texas, *in* Hunt, T. J., and Lufholm, P. H., eds., The Permian Basin: back to basics: West Texas Geological Society Publication No. 03-112, p. 397–418.

Cotton, C. B., 1966, Barnhart field, *in* Oil and gas fields in West Texas Symposium: West Texas Geological Society Publication 66-52, p. 38–41.

Dhiraj, Dembla, 2004, Stimulating enhanced oil recovery (EOR) by high-pressure air injection (HPAI) in west Texas light oil reservoir: The University of Texas at Austin, Master's thesis, 123 p.

Dutton, S. P., Kim, E. M., Broadhead, R. F., Raatz, W. D., Breton, C. L., Ruppel, S. C., and Kerans, Charles, 2005, Play analysis and leading-edge oil-reservoir development methods in the Permian basin: increased recovery through advanced technologies: American Association of Petroleum Geologists Bulletin, v. 89, no. 5, p. 553–576

Erickson, A., Legerki, J. R., and Steece, F. V., 1992, An appraisal of high pressure air-injection (HPAI) or in-situ combustion results from deep, high-temperature, high gravity oil reservoirs, *in* 15th Anniversary Field Conference, Wyoming Geological Association Guidebook, p. 259–270.

Fassihi, M. R., Yannimaras, D. V., and Kumar, V. K., 1997, Estimation of recovery factor in light-oil air-injection projects, *in* SPE Reservoir Engineering, August, p. 173–178.

Fassihi, M. R., Yannimaras, D. V., Westfall, E. E., and Gilham, T. H., 1996, Economics of light oil injection projects, *in* Tenth Symposium on Improved Oil Recovery, Tulsa, Oklahoma, SPE/DOE 35393, p. 501–509.

Gale, J. F. W., and Gomez L., in press, Late opening-mode fractures in karst-brecciated dolostones of the Lower Ordovician Ellenburger Group, West Texas: recognition, characterization, and implications for fluid flow: American Association of Petroleum Geologist Bulletin.

Galloway, W. E., Ewing, T. E., Garrett, C. M., Jr., Tyler, N., and Bebout, D. G., 1983, Atlas of major Texas oil reservoirs: The University of Texas at Austin, Bureau of Economic Geology Special Publication, 139 p.

Glandt, C. A., Pieterson, R., Dombrowski, A., and Balzarini, M. A., 1998, Coral Creek field study: a comprehensive assessment of the potential of high-pressure air injection in a mature waterflood project, *in* SPE Midcontinent Operations Symposium, Oklahoma City, Oklahoma, SPE 52198, 11 p.

Gomez, L. A., Gale, J. F. W., Ruppel, S. C., and Laubach, S. E., 2001, Fracture characterization using rotary-drilled sidewall cores: an example from the Ellenburger Formation, West Texas, *in* Viveiros, J. J., and Ingram, S. M., eds., The Permian Basin: microns to satellites, looking for oil and gas at all scales: West Texas Geological Society Publication No. 01-110, p. 81–89.

Holtz, M. H., Ruppel, S. C., and Hocott, C. R., 1992, Integrated geologic and engineering determination of oil-reserve-growth potential in carbonate reservoirs: Journal of Petroleum Technology, v. 44, no. 11, p. 1250–1257.

Holtz, M. H., and Kerans, C., 1992, Characterization and categorization of West Texas Ellenburger reservoirs, *in* Candelaria, M. P., and Reed, C. L., eds., Paleokarst, karst-related diagenesis, and reservoir development: examples from Ordovician-Devonian age strata of West Texas and the Mid-Continent: Permian Basin Section-SEPM, Field Trip Guidebook, Publication No. 92-00, p. 45–54.

Hunt, T., 2000, Review of Barnhart Field: Ellenburger Group, Ozona Uplift, Reagan
County, Texas, *in* DeMis, W. D., Nelis, M. K., and Trentham, R. C., eds., The
Permian Basin: proving ground for tomorrow's technologies: West Texas
Geological Society Publication No. 00-109, p. 107–111.

Kerans, C., 1990, Depositional systems and karst geology of the Ellenburger Group
(Lower Ordovician), subsurface West Texas: The University of Texas at Austin,
Bureau of Economic Geology Report of Investigations No. 193, 37 p.

Kuhlman, M., 2004, Evaluation of the Barnhart-Ellenburger air-injection pilot: MK Tech
Solutions, Inc., unpublished engineering report, 18 p.

Kumar, V. K., Fassihi, M. R., and Yannimaras, D. V., 1995, Case history and appraisal of
the Medicine Pole Hills Unit air-injection project, *in* SPE Reservoir Engineering,
August, p. 198–202.

Kupecz, J. A., and Land, L. S., 1991, Late-stage dolomitization of the Lower Ordovician
Ellenburger Group, West Texas: Journal of Sedimentary Petrology, v. 61, p. 551–
574.

Laubach, S. E., 2003, Practical approaches to identifying sealed and open fractures:
American Association of Petroleum Geologists Bulletin, v. 87, p. 561–579.

Laubach, S. E., Marrett, R. A., and Olson, J. E., 2000, New directions in fracture
characterization: The Leading Edge, p. 704–711.

Loucks, R. G., 1999, Paleocave carbonate reservoirs: origins, burial-depth modifications,
spatial complexity, and reservoir implications: American Association of
Petroleum Geologists Bulletin, v. 83, p. 1795–1834.

Loucks, R. G., 2003, Understanding the development of breccias and fractures in
Ordovician carbonate reservoirs, *in* Hunt, T. J., and Lufholm, P. H., The Permian
Basin: back to basics: West Texas Geological Society Fall Symposium: West
Texas Geological Society Publication #03-112, p. 231–252.

Loucks, R. G., and Mescher, P., 2001, Paleocave facies classification and associated pore types: American Association of Petroleum Geologists, Southwest Section, Annual Meeting, Dallas, Texas, March 11–13, CD-ROM, 18 p.

Marrett, R., 1996, Aggregate properties of fracture populations: Journal of Structural Geology, v. 18, p. 169–178.

Marrett, R., Ortega, O., and Kelsey, C., 1999, Extent of power-law scaling for natural fractures in rock: Geology, v. 27, p. 799–802.

Mazzullo, S. J., 1989, Formational and zonal subdivisions of the Ellenburger Group (Lower Ordovician), southern Midland Basin, Texas, *in* Cunningham, B. K. and Cromwell, D. W., eds., The lower Paleozoic of West Texas and southern New Mexico—modern exploration concepts: Permian Basin SEPM Publication no. 89-31, p. 113–121.

Ortega, O., 2002, Fracture-size scaling and stratigraphic controls on fracture intensity: The University of Texas at Austin, Ph.D. dissertation.

Reed, R. M., and Milliken, K. L., 2003, How to overcome imaging problems associated with carbonate minerals on SEM-based cathodoluminescence systems: Journal of Sedimentary Research, v. 73, p. 326–330.

Ruppel, S. C., and Cander, H. S., 1988, Effects of facies and diagenesis on reservoir heterogeneity: Emma San Andres field, West Texas: The University of Texas at Austin, Bureau of Economic Geology Report of Investigations No. 178, 67 p.

Ruppel, S. C., and Holtz, M. H., 1994, Depositional and diagenetic facies patterns and reservoir development in Silurian and Devonian rocks of the Permian Basin: The University of Texas at Austin, Bureau of Economic Geology Report of Investigations No. 216, 89 p.

Sipes, Williamson, and Aycock, Inc., 1973, Waterflood feasibility study Barnhart (Ellenburger) field Reagan County, Texas: unpublished technical report, 28 p.

Umphress, A. M., 1977, Lithostratigraphic zonation of the Ellenburger Group within the
Belco Hickman No. 13 well, Barnhart Field, Reagan Uplift, Texas: The
University of Texas at Arlington, Texas, unpublished Master's thesis, 117 p.

Tyler, N., Bebout, D. G., Garrett, C. M., Jr., Guevara, E. H., Hocott, C. R., Holtz, M. H.,
Hovorka, S. D., Kerans, C., Lucia, F. J., Major, R. P., Ruppel, S. C., and Vander
Stoep, G. W., 1991, Integrated characterization of Permian Basin reservoirs,
University Lands, West Texas: targeting the remaining resource for advanced oil
recovery: The University of Texas at Austin, Bureau of Economic Geology
Report of Investigations No. 203, 136 p.

Watts, B. C., Hall, T. F., and Petri, D. J., 1997, The Horse Creek air injection project: an
overview: SPE 38359, SPE Rocky Mountain Regional Meeting, Casper,
Wyoming, p. 143–154.

APPENDIX 1: REPORTS, PAPERS, & PRESENTATIONS

Combs, D. M., Loucks, R. G., and Ruppel, S. C., 2003, Lower Ordovician Ellenburger Group collapsed Paleocave facies and associated pore network in the Barnhart field, Texas, *in* Hunt, T. J., and Lufholm, P. H., eds., The Permian Basin: back to basics: West Texas Geological Society Publication No. 03-112, p. 397–418.

Combs, D. M., Loucks, R. G., and Ruppel, S. C., 2004, Lower Ordovician Ellenburger Group collapsed paleocave facies, associated pore networks, and stratigraphy at Barnhart field, Reagan County, Texas: Southwest Section AAPG, El Paso, Texas.

Dhiraj, Dembla, 2004, Stimulating enhanced oil recovery (EOR) by high-pressure air injection (HPAI) in west Texas light oil reservoir: The University of Texas at Austin, Master's thesis, 123 p.

Gale, J. F. W., and Gomez L., in press, Late opening-mode fractures in karst-brecciated dolostones of the Lower Ordovician Ellenburger Group, West Texas: recognition, characterization, and implications for fluid flow: American Association of Petroleum Geologist Bulletin.

Gomez, L. A., Gale, J. F. W., Ruppel, S. C., and Laubach, S. E., 2001, Fracture characterization using rotary-drilled sidewall cores: an example from the Ellenburger Formation, West Texas, *in* Viveiros, J. J., and Ingram, S. M., eds., The Permian Basin: microns to satellites, looking for oil and gas at all scales: West Texas Geological Society Publication No. 01-110, p. 81–89.

Loucks, R. G., 2003, Understanding the development of breccias and fractures in Ordovician carbonate reservoirs, *in* Hunt, T. J., and Lufholm, P. H., The Permian Basin: back to basics: West Texas Geological Society Fall Symposium: West Texas Geological Society Publication #03-112, p. 231–252.

Ruppel, S. C., Loucks, R., and Kane, J., 2004, Report on the geology and petrophysics of the Ellenburger reservoir at Barnhart field, Reagan County, Texas: The University of Texas at Austin, Bureau of Economic Geology, Consultant Report prepared for Goldrus, 35 p.